Iterative Geostatistical Time Lapse (4D) Seismic Inversion

Baraa Osman Abdo Osman

Thesis to obtain the Master of Science Degree in

Energy Resources Engineering

Supervisors: Professor Leonardo Azevedo
Dr. João Narciso

December 2023

Declaration

I declare that this document is an original work of my own authorship and that it fulfills all the requirements of the Code of Conduct and Good Practices of the Universidade de Lisboa.

Acknowledgments

It is with God's grace and blessings that I would like to dedicate this work to my mother. Thank you for your sacrifice and efforts to make me and my siblings the valuable members of our communities and being the men and women we have become. To my father, words cannot express how fortunate I am to have your never-ending support through all my endeavors, no matter how unconventional! This has played a big part in who I am today and I hope to make you proud by giving back to our hometown, I am sure that there is a lot to be done to improve their quality of life and contribute to the sustainability of our community.

To my brother Mohammed, thank you for your unwavering motivation to always be a better version of myself and for pushing to break all barriers and not shying away from any challenge, personally, academically, and professionally. I want to especially thank you for the past 6 months, I know that the situation in Sudan was very hectic and uncertain, and even after being displaced for more than 7 months stranded from borders to embassies, and even through all of that, you were always there for me!

To my sister Tala, you have always been the anchor to our household making sure Mom and Dad are taken care of, even when you were still back home and just juggling crazy hours at the clinic and early morning surgeries with Dr. Saleh and those road trips to Dammam and Qassim, thank you for being who you are and I wish you all the best in your future endeavors....Manchester is very lucky!

To my brother Ahmed, I cannot even begin to tell you how proud I am of you and what you have achieved so far. Thank you for always giving me one more reason to strive to be a role model for you, and I am more than proud to say that you have exceeded all my expectations. One thing I have never told you is that I never had and still do not have any doubt about where you will reach in your life and being one of the student body leaders at California State University, where I have witnessed firsthand the admiration of your peers and your value to your community.

To my sister Maya, words cannot express the feeling I get when I do the math of how old am I and the woman you are today, it is very hard to see you other than my baby sister. I am so proud of what you have become, I know that I was tough on you and Ahmed growing up, but all was so that you would be ready for being an adult once you left the nest to go and forge your path.

To my aunties, Neven and Sussan. You have always been the role models we looked up to and I can't wait to come back home and share my successes and adventures with you.

To my best friends Honda, Amr ”Bebo” Essam, Turki Abo Tallal, Wael, Abdallah Gamil, Nevena, Modi, and Faisal Abo Wa'al. Thank you for your friendships, good times, life long memories and always having my back, especially during these past 3 years being away from home making the hard choice of favoring my career and education.

I would like to acknowledge my thesis supervisor Professor Leonardo Azevedo; it has been a great honor and a privilege to learn with a master of modern Seismic Reservoir characterization. I know we have had our ups and downs, I appreciate you and I truly value this journey and everything you have taught me. Thank you for all your patience, understanding and always pushing me to be better.

To Professor Amilcar and Professor Maria Joao, thank you very much for being a home away from home for me even when you did not know it, and I hope to continue this journey with all of you at CERENA and the Department of Mining and Energy Resources making significant scientific contributions, as well as to our student body. I would like to thank João Narciso for all his help and answering all of my dumb questions throughout this journeys and especially the last month with all the tremendous help with the Professor Leonardo's codes and the implementation of our proposed methodology.

To Professor Mohamed Shahir Leiw and Ahemed T. Al-Qadeeb I am truly thankful to both of you for seeing the potential in me when I was not even aware of it.

We would like to thank and acknowledge SLB for providing an academic licence to Petrel, and we would like to thank and acknowledge Equinor for providing the Sleipner dataset provided through Co2Datashare.

Abstract

Time-lapse (4D) seismic analysis is crucial for the containment and conformance assessment of CCS projects. However, interpreting CCS data for 4D signals like the Sleipner dataset faces challenges from noise, velocity effects, and thin-bed tuning. Advances in data processing and quantitative analysis methods offer promise for more accurate interpretations. Seismic reservoir characterization relies on inverted elastic subsurface models to predict the distribution of porosity, permeability, and fluid saturation. Probabilistic seismic inversion methods provide high-resolution models with uncertainty assessment. Our proposed iterative geostatistical time-lapse inversion methodology predicts the difference in acoustic impedance Acoustic Impedance (Ip) using available seismic data. It considers all available vintages simultaneously and uses geostatistical simulations for perturbation, driving convergence and better exploration of the model parameter space. We apply this methodology to monitor the growth of the CO2 plume from 1994 to 2006 using the 2007 processing of the Sleipner's seismic data.

Keywords

Geostatistical Seismic Inversion; Time Lapse; Sliepner; 4D seismic; Carbon Capture and Storage Carbon Capture and Storage (CCS); Monitoring; Containment; Conformance; Spatio-temporal modeling

Resumo

A análise sísmica de lapso de tempo (4D) é crucial para a avaliação de contenção e conformidade de projetos de CCS. No entanto, a interpretação de dados CCS para sinais 4D, como o conjunto de dados de Sleipner, enfrenta desafios de ruído, efeitos de velocidade e ajuste de leito fino. Os avanços no processamento de dados e nos métodos de análise quantitativa prometem interpretações mais precisas. A caracterização de reservatórios sísmicos depende de modelos elásticos invertidos de subsuperfície para prever a distribuição de porosidade, permeabilidade e saturação de fluidos. Os métodos probabilísticos de inversão sísmica fornecem modelos de alta resolução com avaliação de incerteza. Nossa metodologia iterativa de inversão de lapso de tempo geoestatística proposta prevê a diferença na impedância acústica Acoustic Impedance (Ip) usando dados sísmicos disponíveis. Ele considera todas as safras disponíveis simultaneamente e utiliza simulações geoestatísticas para perturbação, conduzindo convergência e melhor exploração do espaço de parâmetros do modelo. Aplicamos esta metodologia para monitorar o crescimento da pluma de CO2 de 1994 a 2006 usando o processamento de 2007 dos dados sísmicos do Sleipner.

Palavras Chave

Inversão Sísmica Geoestatística; Espaço de tempo; Slipper; Sísmica 4D; Captura e Armazenamento de Carbono Carbon Capture and Storage (CCS); Monitoramento; Contenção; Conformidade; Modelagem espaço-temporal

Contents

List of Figures

Acronyms

bestccAI6	Acoustic Impedance Similarity
CCS	Carbon Capture and Storage
CMP	Common Midpoint
Co-DSS	Direct Sequential Co-simulation
DSS	Direct Sequential Simulation
FWI	Full Waveform Inversion
GHG	Greenhouse Gases
GSI	Geostatistical Seismic Inversion
Ip	Acoustic Impedance
IPCC	Intergovernmental Panel on Climate Change
KB	Kelly Bushing
NMO	Normal Move-out
MD	Total Measured Depth
RC	Reflection Coefficients
TVD	True Vertical Depth
TWT	Two Way Time
UN	United Nations
UNSDG	United Nations Sustainable Development Goals

1

Introduction

Contents

The United Nations (UN) Intergovernmental Panel on Climate Change (IPCC)'s definition of Greenhouse Gases (GHG) are gases that absorb infrared radiation trapping the earth's heat within the atmosphere causing what is known as the greenhouse effect which is amplified by the anthropogenic emissions of greenhouse gases into the atmosphere [1, 2]. The increased temperatures after the greenhouse effect takes place set forth a combination of unfavorable conditions that lead to climate fluctuations, which in turn affect natural weather cycles which might affect and endanger human life. The global reduction of greenhouse gases is one of the top global goals and research areas crucial to the sustainable development of the global community.

The United Nations Sustainable Development Goals (UNSDG) 2030 has defined 17 global sustainable development goals with specific objectives and actionable deliverables; of which climate change plays an important role not only being one of the sustainable development goals; but as well as being a major contributing factor to several of the remaining sustainable development goals, such as the ending of global hunger and poverty and the access to clean and affordable energy. Carbon Capture and Storage is one of the integral energy transition solutions by decarbonizing heavy emitter energy sources [1, 3]. Carbon Capture and Storage (CCS) is divided into three main parts: Capture, Transport and Storage; Capture which includes liquid capture materials, solid capture materials, and the cryogenic capture process; Transport can be done via pipelines ships and tankers: Storage ranging from terrestrial storage to continental vegetation, subsea sequestration, and geological sequestration in geological formations.

Carbon geological storage is anchored on three pillars, injectivity, capacity, containment and conformance. Injectivity is how easily will the CO2 flow, that is, 'injected', from the bottom-hole well-bore completion interval into the target formation, typically measured with the injectivity index, which is the ratio of the flow rate over the pressure differential (volume / time / pressure). Capacity quantifies the available structural volumetric space of the target formation, captured by total and effective porosity, as well as absolute and relative permeability and the storage efficiency factor along with the reservoir shape factor [4, 5]; Seismic data, mainly 2D and 3D, play a key role in the structural definition of the storage site key for the definition of the structural storage capacity by mapping key horizons and faults in the region; seismic inversion guides the distribution of properties in the formation, such as porosity and permeability, which refine the volume available for storage. Containment is the ability of the target formation, with the relevant subsurface properties, to enclose the injected CO2 with all available storage processes; structural trapping, residual trapping, and mineralization of the stored CO2. Conformance of a carbon geological storage project demonstrates the evaluation of the performance of the storage site in its ability to contain the injected CO2 in the designated capacities and locations in the subsurface, outlined in the project design phase.

In a published study in Nature [5], highlights the importance of global continental margins for providing high-quality CO2 storage resources and proposes the development of 10-14 thousand CO2 injection wells globally by 2050 to enable the global deployment of offshore storage for facilitating the two-degree scenario, based on analysing historical data from prolific basins around the world, namely the Golf of Mexico and the North Sea basins utilizing the principles of pore-space utilization and subsurface pressure constraints; to provide a global baseline to guide nations in their attempt to employ and deploy CCS solutions within their energy mix [6, 7].

1.1 Motivation

Time-Lapse seismic data plays an integral role in the evaluation, creation, and curating of Mechanical Earth Models; a key part of any study and analysis of the soil's or deeper subsurface's geomechanical properties, which is detrimental to the containment aspect of the CCS regulatory requirements. Time-lapse 4D analysis of seismic data is the leading measure of containment and conformance of CCS projects [**?**, 4, 8–10]. The interpretation of 4D signals can be done either qualitatively or quantitatively, after production and/or injection induced elastic changes in the reservoir, for 4D anomalies that can be attributed to changes in saturation, pressure and temperature. Qualitative interpretation is done through the visual inspection of the repeated 3D seismic surveys (i.e. monitors) for 4D anomalies, which are extracted by subtracting the monitors from the base seismic (i.e. prior to injection and/or production). It is more common to do this comparison between predicted 4D signals, acquired through forward modeling a history matched reservoir model for base and monitor scenarios and getting the difference between them, and real observed 4D signals coming from the differences between real seismic data of the base and monitor [11]. The challenges and main drawbacks for the qualitative interpretation are the inability to quanitufy the uncertainity in the predictions and the amount of unused information that is contained in the seismic signal [11, 12].

The quantitative interpretation of time lapse seismic, 4D seismic inversion, faces the challenge of linking the temporal domain between the base and monitor survey(s), where independent inversions of the base and monitors lack the prediction of elastic anomalies as there is no explicit dependency between the different seismic volumes.

Current solutions are mainly based on inverting the amplitude anomalies that are calculated by subtracting the base survey from the monitor survey. This contradicts the general guidelines of global approaches such as GSI-related methods. The proposed workflow aims to connect the different data in the temporal domain by altering the objective function to take into account the seismic amplitude discrepancies.

Time-lapse analysis can be achieved either in the seismic domain, elastic domain eg. Acoustic Impedance (Ip), or by interpreting the time delays at the base of the reservoir after subtracting the base and monitor seismic surveys [13]. Most of the state-of-the-art methodologies are based on the calibration and alignment of the monitor and base before subtraction prior to interpretation [14–16]. The seismic domain interpretation is by the subtraction of base and monitor surveys highlighting plume boundaries and outlines, as well as demonstrating the geophysical changes in the seismic signal, mainly CO2-induced velocity push-downs and thin shale layer pull-up effects which are the first quantitative measurement coming from the data which are used in the time delays interpretations. As for interpretation in the Ip domain, it is based on the inversion of the base and monitor seismic data to acoustic impedance models with the appropriate inversion scheme and associated assumption.

This thesis is about the monitoring of CO2 as part of the subsurface CCS where we aim to invert time lapse seismic simultaneously to link the different surveys in the temporal domain. The Sleipner Carbon Capture and Storage project, which began CO2 injection in 1996, is the world's first project of its kind as a greenhouse gas emission remediation measure. It serves as a unique case study for the carbon capture and storage ecosystem, providing valuable insights and influencing technical and regulatory aspects of the CCS value chain, as well as responding to policy updates [4]. Modeling and characterizing the spatial evolution of the CO2 plume distribution in the Sleipner field has proven to be a challenging task. Various modeling approaches have been employed to capture the multilayer plume distribution observed through Time-Lapse (4D) seismic analysis; CO2-induced velocity pushdowns and thin shale layer pull-up effects are one of the main challenges in Sleipner's CO2 Time-Lapse analysis [14, 17–21].

Probabilistic seismic inversion has a distinct advantage over deterministic inversion in detecting and predicting the spatial distribution of subseismic rock formation, below seismic resolution, making it an excellent candidate to resolve subseismic shale baffles in the Utsira formation. State-of-the-art methodologies based on the calibration and alignment of the monitor and base, these initial transformations do not agree with the general guidelines of the Geostatistical Seismic Inversion (GSI). [22–24]

1.2 Objectives

The objective of this thesis is the development and implementation of an iterative geostatistical time-lapse inversion methodology with the ability to predict the difference in acoustic impedance Ip between different time steps using the available seismic data. The proposed methodology considers all available vintages simultaneously, compliant with the general guidelines of the Global Stochastic Inversion and using geostatistical simulation and co-simulation as the preferred method to perturb the parameter spaces over successive iterations driving the convergence of the proposed iterative procedure.

Our proposed methodology is applied on a real dataset to monitor the growth of the CO2 plume over the span of 1994 to 2006, using the 2007 processing of Sleipner's 1994, 2001, 2004, and 2006 seismic data.

1.3 Structure Of The Thesis

In Chapter 1 we set the scene by introducing the global drivers for carbon neutrality and energy transition efforts; the role of CCS in the greenhouse mitigation efforts is highlighted along with relevant key consideration for CCS projects. Then we describe the motivation for the thesis and followed by stating the objectives of our study and the structure of the thesis.

In this thesis's Chapter 2, we will cover the relevant literature reviewing the fundamentals of the geophysical inverse problem, followed by a comparison between deterministic and probabilistic inversion methods with a focus on the state of the art of the seismic reservoir characterization and inversion research domain; finally, we will highlight the relevant Time-Lapse 4D interpretation methods.

In Chapter 3, we describe the necessary steps to be applied before the implementation of our proposed methodology. First, we describe Exploratory Data Analysis which deals with data mining, analyzing, visualizing, and describing the data; then we walk through the procedures for creating the geocellular model for the inversion and followed with the methodology implemented for the calculation of the experimental variogram as well as elaborating the spatial continuity revealing nested variogram models. After which we give a brief description of the Geostatistical Seismic Inversion methodology implemented as a benchmark for our proposed iterative geostatistical inversion. Finally, we describe the stages of our proposed algorithm, highlighting the novel objective function that drives the convergence of our inversion.

Chapter 4 starts with a description of the Sleipner data set utilized to demonstrate our proposed methodology, followed by an illustration of the results of the GSI algorithm to be implemented as a benchmark, and the results of our proposed methodology are discussed; then Chapter 5 concludes the thesis with recommendations for future improvements as well as reflections and self-assessment of the thesis.

2

Literature Review

Contents

Seismic data plays an integral role in the characterization of the subsurface, from a mining and energy resources point of view. Recently, more novel approaches [24–26] for the utilization of seismic data through seismic inversion, which is simply described as moving from an impedance contrast interface reflectivity to a layer-based property of interest, such as acoustic and shear impedance, porosity, permeability [27], shale total organic carbon [28], ocean salinity, temperatures, and acidity, or detecting CO2 in CCS operations [4, 19, 21].

Seismic data, which is acquired in a shot receiver arrangement processed to Common Midpoint (CMP), can be 2D with CMP and Two Way Time (TWT), or 3D with inlines, crosslines, and TWT, or Time Lapse (4D), which are 3D surveys acquired over successive periods of time. Stacking is the summation of all traces which belong to a CMP into one trace after Normal Move-out (NMO), resulting in reinforced reflections and an increasing signal-to-noise ratio. Migration re-positions reflections to their true spatial position, prestack migration is done trace by trace, while post-stack migration is done with stacked CMP gathers.

Time-Lapse (4D) data have the ability to detect elastic changes due to changes in reservoir conditions, such as pore pressure, temperature, saturation, and induced geomechanical changes, all of which are connected and will influence the rock's physical response to the reservoir elastic changes. In recent decades, 4D seismic technology has been instrumental in characterizing carbon storage sites and tracking CO2 throughout the subsurface, demonstrating capacity, injectivity, and containment [4, 8, 19, 29].

2.1 The Geophysical Inverse Problem

Seismic reservoir characterization is a critical part of the Geomodeling workflow to predict the spatial distribution of properties of interest, such as porosity, permeability, fluid saturation, and fluid content [30–34]. Predicting the spatial distribution of continuous and categorical subsurface properties, such as Ip and lithofacies [35], respectively, from observed data is termed seismic inversion when utilizing recorded seismic amplitudes [36]

$$\mathbf{d_{obs}} = \mathbf{g}(\mathbf{m}, \mathbf{f}) + \mathbf{e} \tag{2.1}$$

where $\mathbf{d_{obs}}$ is the recorded seismic data, we wish to invert it back to the spatial distribution of its acoustic, elastic $\mathbf{m}$ and categorical properties $\mathbf{f}$. The operator $\mathbf{g}$ is a known forward model that maps the properties of the model into the data domain [37, 38].

The solution to the seismic inverse problem $\mathbf{G}^{-1}$, the inverse function of the forward model, retrieves the spatial distribution of the properties of interest, $\mathbf{m}, \mathbf{f}$ given the observed data, i.e., the recorded seismic data, $\mathbf{d_{obs}}$, is unknown, ill-posed, non-linear and allows multiple equiprobable solutions [37].

This means that there will be an ensemble of models with the same probability of occurring, i.e., spatial random variables, that will satisfy the solution to the inverse model $\mathbf{G}^{-1}$. The solution of the inverse problem is dependent on the assumptions made about the model parameters and the forward model $\mathbf{g}$. Seismic inversion methodologies can be classified into the deterministic approaches [39, 40], and the probabilistic approaches (i.e. stochastic), which have the advantage of assessing the uncertainty and facilitating the detection of subseismic anomalies, and require concept generalization contributions to ease the understanding and uptake by academic and industry professionals [36, 41].

By now we should be familiar with the basic concept of forward modeling $\mathbf{g}$, just as the name implies, we push the input through the model from an estimation towards a reality observation and going back from the reality observation, i.e, data measured, back to the model domain in the opposite ”inverse” direction, $\mathbf{G}^{-1}$. Depending on where we start from and where we are going to, this will dictate whether it is a forward model or an inversion, and the data type at those starting and destination points will dictate what kind of forward model or inversion it is. In other words, if we are starting with real observation of seismic data and we wish to retrieve acoustic or elastic impedance models, this will be termed seismic or elastic inversion, and the way back is the seismic forward model based on the convolution of a known wavelet with a reflectivity series derived from elastic properties. When starting with elastic properties and we wish to go for a model of petrophysical properties, this is termed rock physics or petrophysical inversion. When starting with seismic data and we wish to retrieve petrophysical properties, this is termed Joint seismic and rock-physics inversion and the way back is termed seismic and rock-physics forward model [36].

2.2 Deterministic versus Stochastic Seismic Inversion

Seismic inversion problems can be formulated in a deterministic or probailistic Deterministic methods iteratively update the initial model, that is, the low-frequency model, using a deterministic optimization algorithm to converge predicted seismic towards observed seismic yielding a smooth representation of the subsurface representing the average properties on a seismic scale, with the most notable drawback being the limitetd uncertainty assessment of the predicted results [41]. Deterministic inversions such as recursive and coloured inversion [39, 42] are fast-track Ip approximations that are useful in preliminary studies in frontier areas.

In a recent review paper [36], a range of publications that cover various aspects of seismic reservoir characterization were presented. These included modeling methods, practical application, and the fundamentals of seismic reservoir characterization. The authors also highlighted the integration of geostatistical methods in seismic reservoir studies and the incorporation of rock-physics models in probabilistic seismic inversion workflows. In summary, these publications provided a comprehensive overview of inversion methods for seismic reservoir characterization. They emphasized the importance of probabilistic approaches, rock-physics modeling, and the integration of geostatistical methods. Furthermore, they gave insights into the different categories of inversion methods and their applications while also acknowledging the challenges and assumptions associated with each approach.

The primary focus of the state-of-the-art in seismic reservoir characterization is the probabilistic inversion methods of seismic data as opposed to seismic imaging which deals with Full Wave Inversion methods for elastic properties [36, 41]. Probabilistic seismic inversion methodologies have matured and have demonstrated great value for the energy industry [36, 41]. These methods enable the sampling of multiple inverse models with similar convergence levels and the assessment of uncertainty related to observed data (such as well-log and seismic reflection data) and the physical process being modeled (such as acoustic wave propagation). Both Bayesian linearized methods [43–45] and geostatistical methods [31, 46, 47] have been utilized. Probabilistic approaches have the unrivaled advantage of retrieving subseismic resolution subsurface rock and elastic properties [31, 36]. Resolving of subseismic geologic features, below the seismic resolution, is determined by the spatial model introduced by the sampling algorithm used to generate multiple reservoir models, rather than the seismic data or the optimization algorithm used for inversion [36].

Probabilistic inversion techniques can be divided into four main groups: Bayesian analytical inversion, Monte Carlo methods, stochastic optimization, and probabilistic deep learning. However, these categories are not absolute, as some techniques may fit into multiple categories. For instance, certain sampling techniques can be seen as both Monte Carlo methods and stochastic optimization algorithms [36].

Bayesian approaches are the most commonly used in probabilistic inversion, where the goal is to estimate the posterior probability distribution of the model variables. Bayesian analytical inversion methods are highlighted for providing an analytical solution to the posterior probability density function conditioned on the measured data. These methods are generally faster and computationally more efficient than numerical methods-based solutions such as stochastic optimization. However, they require linearization of the forward model and make restrictive assumptions about the probability distributions of the model parameter space [36, 41].

Monte Carlo methods, such as Monte Carlo acceptance-rejection sampling and Markov chain Monte Carlo (MCMC), are iterative algorithms used to approximate the posterior distribution. These methods generate a large set of models to represent the uncertainty in the inversion process [36, 41]. Stochastic optimization algorithms, on the other hand, iteratively generate models and stochastically perturb them until the mismatch between predicted and measured data falls below a specified threshold. The optimal solution is the model with the lowest misfit value [41, 48].

2.3 Time Lapse(4D) Interpretation

Seismic attributes are implied, measured, or computed measurements that deduce meaningful conclusions from the seismic data [13]. Attributes such as seismic amplitude [49], root mean square amplitude [50], Ip [51, 52], and sweetness are highly critical in the 4D seismic interpretation process. Frequency and phase are sensitive to reservoir changes, such as pressure and fluid saturation, making them suitable for use in reservoir monitoring purposes.

The primary objective of 4D seismic interpretation is to capture changes in 4D seismic attributes generated from multiple surveys throughout the operation. In theory, changes in pressure and fluid saturation should modify the seismic response due to changes in velocity and density [35, 53, 54]. If these changes are of significant magnitude, they will be evident in the difference between the baseline and monitor surveys [13].

Seismic attributes are either surface attributes, such as at the top of the reservoir, or volume attributes for a specified seismic cube. Due to the different sensitivities of these attributes to different reservoir properties, whether volume or surface, the effective combination of these different seismic attributes will yield an effective 4D seismic interpretation [13].

Seismic amplitudes are directly related to fluid saturation in the reservoir and its pressure, the lithology present, and its thickness, as any alteration in these parameters will yield changes in the seismic velocity and the elastic properties of the rock [13].

Taking the square root of the sum of the squared amplitudes in the data set divided by the sample size in a specific time window yields the root mean squared amplitude, which is integral in channel identification and could be used in hydrocarbon monitoring by capturing amplitude sensitivities. The sweetness attribute identifies thick clean reservoirs, hydrocarbon accumulations, and channel detection using strong sand body reflections within successive shales, highlighting sweet pay zones within the reservoir. Ip is obtained by the multiplication of the density and the velocity logs, which is implemented in the seismic inversion process of extracting subsurface information from the data, such as the identifications of fluid saturation and lithology identifications from log measurements, borehole fluid invasion profiles calculated from well logs, and the discrimination between reservoir fluids (oil, gas, and water) from production logs [51,52,55].

History matching is the step in validating the reservoir model, calibrated with production data, which presents the challenge of being representative at the well location but with questionable consistency with fluid flow and distribution in other locations [13,20,21,56]. Several studies suggest the integration of available data, including geology, geophysics, and engineering, thus improving the reliability of the model [21]. The quantitative 4-D assisted history matching incorporates seismic data, Ip, Poisson ratio, or inverted saturation and pressure [57]. 4-D assisted history matching can be done in three domains: the simulation domain, the elastic domain, and the seismic domain. In the simulation domain, the seismic pressure and saturation are inverted, and then compared to the simulation's pressure and saturation. In the elastic properties domain, the seismic is used to calculate changes in elastic properties and then compared with a forward-modeling impedance-populated simulation model. In the seismic domain, synthetic seismic is generated through rock physics modeling and wavelet convolution, and then compared with the real seismic data [58,59].

4D technologies for reservoir management has 4 main aspects, Time-Lapse Modeling estimating elastic responses, Simulation to Seismic validating new reservoir models, 4D Calibrations to account for different acquisitions and processing parameters between base and monitor seismic and 4D interpretation is concerned with the quantitative interpretations.

Time-Lapse modeling deals with the estimation of production or injection induced velocity and density changes in order to generate synthetic seismic with the convolution with a known a wavelet to predict changes in the reservoirs seismic response. Simulation to seismic starts from a history matched reservoir model to generate pressure and saturation values which are related to the seismic though rock-physics models that is used to generate synthetic seismic to be compared with the monitor seismic survey. This approach can be beneficial in answering operational questions such as when is a good time to acquire a new monitor seismic to evaluate the reservoir performance and are the 4d signals detectible.

4D calibration focuses on the mitigation of non-repeatable noise and different acquisition and processing parameters which detrimental to the robustness of the 4D interpretation. A typical calibration workflow of base and one or more monitors would start with the estimation of cross correlation and shifts. Afterwords the average phase and time shifts, shaping filter and amplitude normalization are calculated and executed, then we can apply cross correlation statics to the top of the reservoir. At this point the seismic is calibrated to the base, this is where we can start witht the first iterpration which deals with the time delays as well as applying the time variant shifts, such as Taylor series expansion and dynamic vector wrapping, to align the base and the monitors at the base of the reservoir as the first step towards the quantitative interpretation of the seismic amplitudes.

2.4 Stochastic Time Lapse(4D) Seismic Inversion

4D interpretation can be done by the analysis of the time delays and seismic amplitude differences as well as deterministic and probabilistic formulations to the inversion problem. The traditional approach for 4D inversion is to independently invert the base and monitor surveys and subtract the elastic results to infer the production effect. However, this approach makes it difficult to interpret the 4D anomalies. The differences interpreted from independent inversions may not be related to production, but rather to differences in seismic vintages [60]. These differences could be artifacts related to convergence to different solutions in the model space, which may not be consistent with the actual subsurface elastic changes. Inverting all vintages simultaneously, combined in a single objective function, allows for reliable and consistent models to be inferred for the expected differences in elastic behavior [60].

With advancements in 4D seismic inversion technologies, there is now a focus on quantitative 4D interpretation workflows, involving 4D inversion in the elastic domain followed by rock physics inversion to estimate changes in fluid saturation and pressure [60]. However, obtaining reliable estimates of time-lapse changes in elastic domain using 4D seismic inversion is a challenging task that has received considerable attention in recent years.

Different approaches have been proposed for 4D inversion, including workflows where base and monitor surveys are inverted separately and then subtracted, i.e. independent inversion, sequential inversion schemes where inversion results for a base survey are used to define an initial model for inverting a monitor survey, direct inversion of amplitude differences for changes in elastic parameters, and global inversion methods where all vintages are inverted simultaneously. Studies and experiences have shown that coupling the inversion of base and monitor surveys is important to obtain quantitative estimates of impedance changes and reduce the non-uniqueness of the inversion process. Among the stochastic methods, one of the most recent methods is the Bayesian inversion of time-lapse seismic data for the estimation of static reservoir properties and dynamic property changes [30]. This methodology proposes a two-step approach: first, the estimation of conditional probability of elastic properties and their relative changes, and then the estimation of posterior probability of rock properties and dynamic property changes. The result is a set of point-wise probability distributions that are used to predict the most probable reservoir models and evaluate the associated uncertainty.

In recent published paper [61], the authers compared independent inversions and joint 4D inversion with the baysiean formulation and benchmearked it with standenred determinstic aproach. Their results showed that the joint 4D inverison has provided more accurate results when compared to the independt inversions as well as being consistant with determistic methods.

The distinct advantage of our proposed methodology is that the inversion methodology is structured with the global stochastic inversion guidelines, where it does not have a similar restrictive linearization assumption of the Bayesian formulation, such that the base seismic and monitor seismic are inverted directly for 4D signals without any calibration or alignment processing prior to the interpretation. Thus, making or methodology compliant with the general guidelines of the Global Stochastic Inversion, which is the key concept for the extension of our proposed methodology into the elastic domain utilizing partial stacked seismic data to invert for shear impedance, compression, and shear velocities as well as the density models, which are the building blocks for further geomechanical assessments into the target formation.

3

Methodology

Contents

3.1 Data Analysis and Model Preparation

In this section, we describe the necessary steps to be applied before the implementation of our proposed methodology. Our methodology requires a minimum of one well with density and sonic log measurements in the zone or formation of interest, which must be covered with a minimum of two seismic surveys, one baseline, and one monitor.

First we describe Exploratory Data Analysis, which deals with analyzing, visualizing, and describing the data; then we walk through the procedures for creating the geo-cellular model for the inversion and followed with the methodology implemented for the calculation of the experimental variogram and fitting model variograms. After which we give a brief description of the Geostatistical Seismic Inversion methodology implemented as a benchmark for our proposed iterative geostatistical inversion. Finally, we articulate the stages of our proposed algorithm, highlighting the novel objective function driving the convergence of our inversion.

3.1.1 Exploratory Data Analysis

A few summary statistics can convey the key elements of most histograms. Summary statistics can divided into three categories: location measures, spread measures, and shape measures.

The statistical measures of location tell us where different segments of the distribution are located. The sum of the values divided by the number of samples gives us the arithmetic mean, the sample that divides the population into two equal parts is the median, and the most frequent value is the mode; all help us figure out where the center of the distribution is.

Various quantiles indicate the location of additional segments of the distribution, such as P10 and P90 or the interquartile range's P25 and P75. Variance, standard deviation, and interquartile range are all measurements of spread. These are used to describe the range of data. The coefficient of skewness and the coefficient of variation characterize the shape of the distribution; the coefficient of skewness provides information on the symmetry, while the coefficient of variation provides information on the length of the tail for specific types of distributions.

When these statistics are combined, they provide a comprehensive summary of the information contained in the histogram. In our methodology, we have chosen the variance as a statistical benchmark for our inverted Ip from both, GSI and GSI 4D, for its sensitivity to extreme values.

3.1.2 Model Creation

In this thesis, we have utilized SLB's Petrel for all the Geology and Geophysics workflows implemented, which implies a particular standard workflow for loading and quality checking the well and seismic data used and all preliminary steps such as despiking and frequency filtering as well as seismic-to-well tie which is a crucial step in any seismic reservoir characterization workflow.

The first step was to set up the appropriate coordinate system for the project, such as UTM-31 as provided in the Sleipner dataset, to guarantee the proper placement of the wellheads in their correct spatial locations. Then the wellhead data is loaded and must include the well name, the X and Y coordinates, water depth, Total Measured Depth (MD), True Vertical Depth (TVD), and reference point which is usually Kelly Bushing (KB) in offshore settings. The well deviation survey is added next, which gives a precise trajectory of the wells in the subsurface, which serves as a spatial anchoring point for all well log measurements and well tops, crucial in seismic to well tie, which are loaded afterward. This highlights one of the most fundamental concepts in spatial inference problems, a location and an attribute or multiple attributes such as in our case with the density and sonic well logs and seismic data. The most important quality checks for the density and sonic logs are such that they should cover the zone of interest plus a top and bottom thickness buffers encapsulating our target, they should be free of measurement errors such as errors that arise due to bad hole conditions like caving or swelling, and should be of positive values. The sonic log is measured in units of time divided by units of length most commonly microsecond per foot, which we need to take the reciprocal and converting it into meters per seconds with the appropriate conversion factor which will result in the P-wave velocity values; which are then multiplied with the density log measured in grams per cubic centimeter for the Ip calculation and the subsequent convolution of the reflection coefficient with a known wavelet estimated from the seismic data at hand.

After we have set up the wells in our study, we create a seismic folder to load our seismic data, which can be loaded individually or multiple seismic data at once. The seismic data is then realized and converted into Petrel's ZGY seismic data format, which allows for smooth display and data handling by the software. The first step where well data meets seismic data is the seismic-to-well tie, where they can both communicate in the two-way time domain vertically and we start to see the well on the seismic section. The initial step of this process is the calibration of the sonic log with ideally a check-shot well log or alternatively a two-way time and depth pairs from the well tops in the well, which are usually found in the literature associated with the wells. After the calibration, we have a new time-depth relationship informed by a calibrated sonic log and the seismic data which is used from here on after. Next is the synthetic generation workflow, extracting a representative wavelet to be convolved with the reflection coefficients calculated at the well location, which is then compared to the real seismic measurements at the same location.

At this point, we check for the alignment at the top and base horizons of our zone of interest and apply the necessary stretch and squeeze for the alignment when needed, as well as the predictability of the extracted wavelet to reproduce the seismic data [41]. In our methodology, we first extract a deterministic wavelet to scale the subsequent statistical wavelet, which will be used for the inversions. The key considerations for the wavelet are that it should be less than or equal to at least half the thickness of the zone of interest encountered by our inversion well, the wavelet should have the same sampling rate as the seismic data such as Sleipner's 2 milliseconds and should follow the polarity convention of the seismic data.

After calibrating the sonic log, extracting the representative wavelets, and generating the synthetic seismic, we are ready to create and populate our Geo-cellular model. The first step is identifying the top of our reservoir, which can be done by interpreting the seismic data or be given processed surfaces such as the depth surfaces provided in the Sleipner data set which need to be converted with the appropriate velocity model for the domain conversion from depth into two-way time. Diffracting the top and base surfaces of the reservoir obtaining the thickness which is then padded from the top and base with half the length of the wavelet encapsulating our zone of interest with the new top and base of the model. These surfaces are fed into the make simple model process in Petrel which will define the top and bottom limits of our model, and are combined with the extracted dimensions of the used seismic cube that will inform the spatial discretization of the grid that will follow the inline and crosslines of the seismic cube. Next is one of the most crucial steps in the Geostatistical Seismic Inversion , the layering of the grid needs to be parallel to ensure that the model's blocks are parallel and of equal volumes, which is quality checked by running the geometrical modeling dialogue to calculate cell volume. Ideally looking at the statistics, we should find that the minimum and maximum values of cell volumes are equal or at least with fractional distances from each other.

When the skeletal and volumetric structures of the model are created, we are ready to populate the grid. We start with up-scaling in the appropriate units the density logs, if available density corrections log as well, along with the converted P-wave velocity log. At this point, is one of the most important milestones where we should always save our project as the next step of resampling the seismic data into the grid, by means of the geometric modeling dialog, tends to cause some issues leading Petrel to restart.

3.1.3 Spatial Exploratory Data Analysis

In addition to statistical analysis, it is necessary to conduct a study of the spatial continuity of the study variables, as some of them are not isotropic and depend on their distribution in space. To this end, we have used experimental variograms and, through a visual process of trial and error, we sought the best variogram model that fits the experimental variogram in the three directions of study, the major direction in line with the seismic acquisition, the minor direction orthogonal to the major direction perpendicularly across the line of the seismic acquisition, and the vertical, which is going to be based on the Ip log with the following inequality: the spatial continuity in the major direction is larger than the spatial continuity in the minor direction which is larger than the spatial continuity in the vertical direction. The model is created, populated, and ready for spatial exploratory data analysis with the calculation and fitting of the experimental variograms. We started with the vertical direction using the Ip log calculated by multiplying the density corrected log with the despiked and frequency-filtered P wave velocity. Since our model only has one monitor well 15/9-13 with velocity and density data, the injection well lacks velocity data, we used the seismic data to calculate the experimental variogram in the spatial direction. First, we set the lag distance equal to the smallest distance in the grid, which in our case was 2 milliseconds, 12.501, and 12.502 in the vertical, major, and minor directions, respectively; the number of lags was chosen such that the search radius is less than or equal to half the model extent in the vertical, major, and minor directions, respectively; the bandwidth was set to 4 times the lag distance and a lag tolerance of 50 percent of the lag distance, values lower than 50 percent will omit values from the calculation while values higher than 50 percent will overlap values in the calculation; finally, the tolerance angle was set to 90 degrees; the calculated experimental variograms are fitted with two nested exponential structures with a 0.11 nugget and varying ranges. These models reveal the spatial continuity pattern of the seismic signal within our grid, which is an integral part of any seismic reservoir characterization workflow.

Table 3.1: Variograms Parameters

Year	Strct	Type	Major (12.502) m	Minor (12.501) m	Vertical (2) ms	Sill	Nugget
1994	1	Exponential	350.056 (28)	275.022 (22)	12 (6)	0.74	0.11
1994	2	Exponential	4400.704 (352)	2587.707 (207)	12 (6)	0.15	
2001	1	Exponential	312.55 (25)	262.521 (21)	12 (6)	0.75	0.11
2001	2	Exponential	1,862.798 (149)	1,400.112 (112)	12 (6)	0.14	
2004	1	Exponential	287.546 (23)	262.521 (21)	12 (6)	0.7	0.11
2004	2	Exponential	1,212.694 (97)	850.068 (68)	12 (6)	0.19	
2006	1	Exponential	275.044 (22)	300.024 (24)	12 (6)	0.68	0.11
2006	2	Exponential	1,187.69 (95)	737.559 (59)	12 (6)	0.21	

3.2 Geostatistical Seismic Inversion

The typical GSI methodology, used as a benchmark in our methodology, can be summarized and visualized in the following sequence and 3.1, respectively.

1. In the first iteration, generate an ensemble of N_s Ip with Direct Sequential Simulation (DSS) [22] and Direct Co-simulation after the first iteration, with a variogram calculated with seismic and well data.

2. With a representative wavelet $\omega\ (t)$ forward model N_s synthetic seismic *s(t)* from normal incident Reflection Coefficients (RC) computed with

   $$RC = \frac{I_{p2} - I_{p1}}{I_{p1} + I_{p2}} \tag{3.1}$$

   where subscript 2 and 1 are the Ip values of the layer below and above the interface, respectively. seismic s(t) results from the convolution of RC(t) and the wavelet $\omega\ (t)$

   $$s(t) = RC\ (t)\ *\ \omega\ (t) \tag{3.2}$$

3. Calculate the trace-by-trace similarity (S) between the Real and the Ns Synthetic traces following equation 3.3

   $$S = \frac{2 * \sum_{s=1}^{N} \left(\mathbf{Seis_{Real}} * \mathbf{Seis_{Synth}}\right)}{\sum_{s=1}^{N} \left(\mathbf{Seis_{Real}}\right)^2 + \sum_{s=1}^{N} \left(\mathbf{Seis_{Synth}}\right)^2} \tag{3.3}$$

4. Store the best Ip and the similarity S of all simulated models in an auxiliary volumes.

5. Return to Step 2 and iterate using Direct Sequential Co-simulation (Co-DSS) with best Ip and S as auxiliary volumes until the global S between the entire real seismic and synthetic volumes is above a predefined threshold or we have reached the specified number of iterations and simulations.

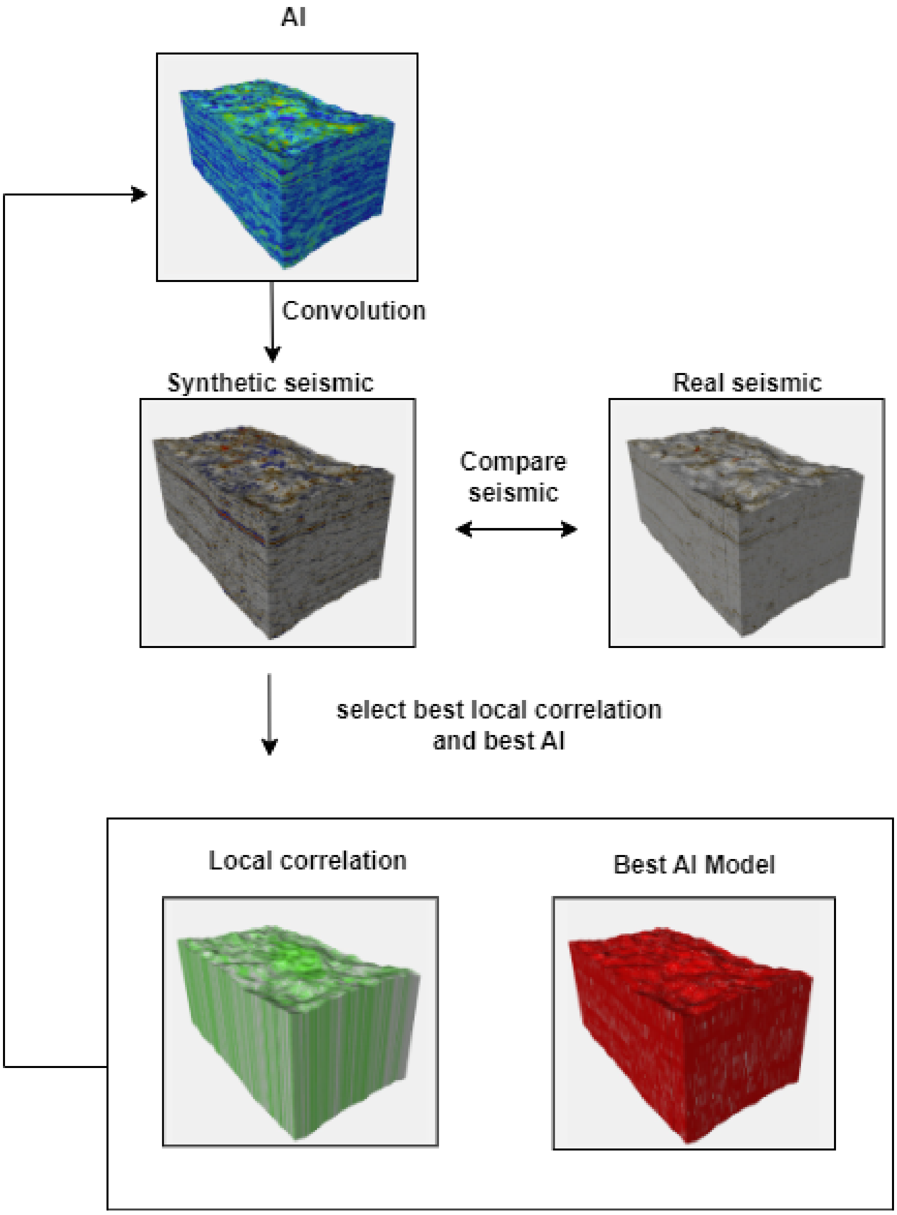

Figure 3.1: Geostatistical Seismic Inversion GSI

3.3 Geostatistical Seismic Time Lapse (4D) Inversion

The proposed iterative geostatistical methodology of time-lapse seismic data for high-resolution 4D signal spatiotemporal models of injected CO2 is based on the GSI framework [62, 63]. Geostatistical approaches have the ability to integrate different data sources with different resolutions and scale support, whilst boasting a symbiotic, mutually beneficial, modeling approach that augments the best advantages of each data source.

Our proposed methodology is implemented for all available vintages. In the first iteration, using the available well data and variogram to generate thirty-two acoustic impedance models for all time steps, base, and all monitors. For every simulation, the generated models are forward modeled with a known wavelet to generate synthetic seismic.

The predicted residuals are obtained with real base seismic minus the generated synthetic monitor seismic, i.e, equation (3.6) and then compared with real residuals between real base seismic and real monitor seismic, i.e, equation (3.7), for all monitor seismic vintages, with the calculation of the similarity coefficient based on the mismatch between predicted and real residual, i.e, equations (3.8). The similarity between real and predicted residuals calculation procedure is repeated three times for three monitors, except for the base seismic inversion to Ip where the convergence-driving similarity calculation is performed between real and predicted seismic of the base.

Our proposed methodology has three key pillars, the forward model, the computation of the local similarity coefficients utilizing four parameters to calculate the interpolation weights as well as the computation of the local correlation coefficients after selecting the best iterations. The local similarity interpolation weights are calculated by equal distributions of 25% each given to the slope, the intercept, the least square means, and the mean values of the generated ensemble. Next is the calculation of the local similarity coefficients, which is calculated with equal proportions to weights based on the number of seismic data available, for our case this 25% as well. In other words, if we had one base seismic and four monitors, the local similarity interpolation weights will be 25% when using the same slope, the intercept, the least square mean, and the mean values from the generated ensemble of acoustic impedance models; while the local similarity interpolation weight will be 20% reflecting the number of available seismic data. The last step is the selection of the best elastic traces which generates the best synthetic seismic are retained along with the corresponding similarity coefficient to be used in the next iteration.

Our proposed geostatistical time-lapse seismic inversion can be summarized in the following sequence and visualized in fig. 3.2.

1. Simulate a set of Ns Ip models given well data and a variogram model
2. Forward model the Ip models with a known wavelet to generate synthetic seismic

   $$RC = \frac{I_{p2} - I_{p1}}{I_{p1} + I_{p2}} \tag{3.4}$$

   where subscript 2 and 1 are the Ip values of the layer below and above the interface, respectively

   $$s(t) = RC\ (t)\ *\ \omega\ (t) \tag{3.5}$$

3. From the synthetic seismic generated in (2), compute the residuals between the synthetic seismic generated in (2) and the observed Baseline Seismic using equation (3.6)

   $$\mathbf{Synth_{4D}} = \mathbf{BaseSeismic_{Real}} - \mathbf{MonitorSeismic_{Synth}} \tag{3.6}$$

   $$\mathbf{Real_{4D}} = \mathbf{BaseSeismic_{Real}} - \mathbf{MonitorSeismic_{Real}} \tag{3.7}$$

4. Compare the predicted residuals from (3.6) with the observed residuals from (3.7) between the observed Monitor and Baseline Seismic using equation (3.8)

   $$S = \frac{2 * \sum_{s=1}^{N} \left(\mathbf{Seis_{Real_{4D}}} * \mathbf{Seis_{Synth_{4D}}} \right)}{\sum_{s=1}^{N} \left(\mathbf{Seis_{Real_{4D}}} \right)^2 + \sum_{s=1}^{N} \left(\mathbf{Seis_{Synth_{4D}}} \right)^2} \tag{3.8}$$

5. Select the best Ip with the similarity coefficients which produces the highest similarity from (3.8) for all vintages simultaneously
6. From the Ip models and similarity coefficients generated in (5), Co-simulate the next Ip models using models generated in (5) as auxiliary variables in the next iterations

Following the guidelines of the GSI with self-updating local probability, the iterative geostatistical time-lapse inversion ensures that all realizations of Ip accurately represent the well data at their respective locations. Additionally, they replicate the spatial continuity pattern described by the three-dimensional variogram model and capture the local and global distributions of Ip [23].

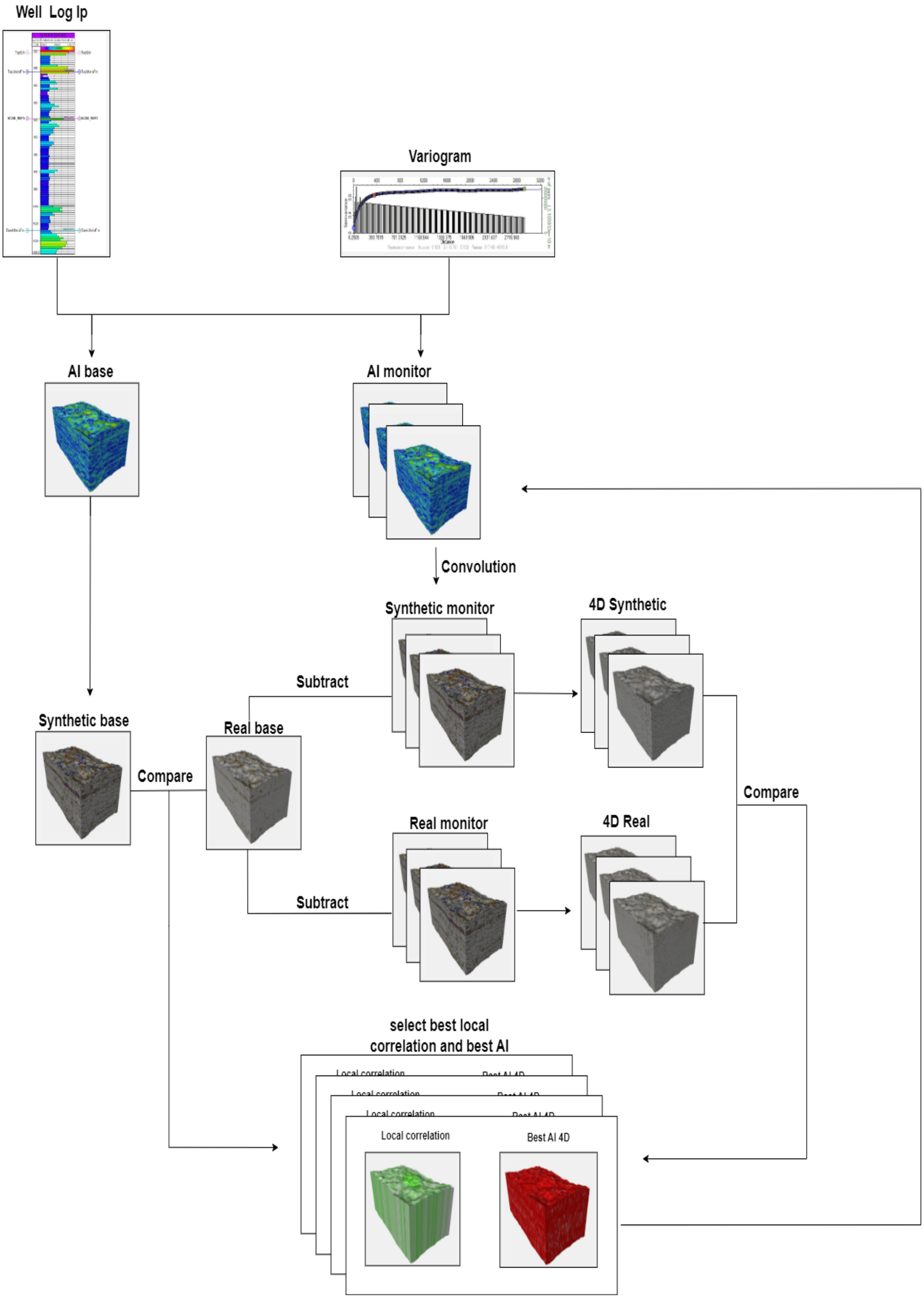

Figure 3.2: Geostatistical Seismic Inversion GSI Time Lapse

4

Results and Discussion

Contents

4.1 Results

4.1.1 Data-set Description

The Sleipner field, located approximately 250 kilometers off the coast of Norway in the Norwegian block 15/9, Production License 046, was discovered in 1974 and began production in 1996. In collaboration with the Sleipner East condensate gas field, which was discovered in 1981 and began production in 1993, Equinor Energy AS (formerly Statoil) and the license partners (LOTOS E&P Norway AS, ExxonMobil E&P Norway, and KUFPEC Norway AS) decided to store the captured CO2 geologically [19]. This decision was motivated by the desire to reduce air pollution, implement a new technology, and take advantage of a CO2 tax incentive, as well as meet state requirements.

The CO2 from the Sleipner West gas production is separated and injected into the Utsira Formation, a mid-to-late Miocene age saline formation located in the Viking Graben of the North Sea. This formation was chosen due to its large size, excellent reservoir qualities, shallow depth, and cost-effective well and topside costs [10, 29, 64]. The Utsira Formation thins out towards the northeast, with an overall increase in clay content, suggesting sediment deposition from west to east. The primary lithofacies within the Utsira Formation consist of clear to white, very fine, and fine-grained marine sandstones, which can also display medium to very coarse grains. These sandstones are interspersed with light greenish, plastic, and soft marine claystone, as well as minor siltstone. Fossils and glauconite are commonly found throughout the formation [65–67].

Since 1996, a near-horizontal deviated well (15/9-A-16) located approximately 1012m below sea level has been used to inject carbon dioxide at a generally consistent annual rate of around 0.9 million tons (Mt). A total of 18 Mt of CO2 has been injected since then, with an initial prediction of 25 Mt of CO2 to be injected over the field's planned 25-year life. In 2014, CO2 from the Gudrun gas field (approximately 50 kilometers north) was processed through the Sleipner Carbon Capture and Storage (CCS) plant, resulting in the production of an additional 100,000 to 200,000 tonnes of CO2 each year [4, 5]. To avoid extra costs and risks, it was decided not to build a specific monitoring well and instead to use distant geophysical monitoring technologies. Extensive geophysical and environmental monitoring have been put in place, including a 3D seismic survey, eight 4D seismic surveys, four microgravimetric measurements on the seabed, one electromagnetic survey, and two imaging surveys. The pressure and flow rate at the wellhead are regularly monitored and have remained the same since the injection began after the injection well was re-completed to address the injectivity issues that occurred in the early stages of the project [4, 17–19]. No signs of CO2 leakage from the storage unit have been detected [19].

In December 2019, Equinor released 4D seismic data with an area of 4 km x 7 km and a 2-second recording acquired in 1994, 1999, 2001, 2004, 2006, 2008, and 2010. Initially, the data was processed in 2001, using the 1994, 1999, and 2001 acquisitions for time-lapse analysis [68].

Subsequently, in 2007 PGS reprocessed the seismic data from 1994, 2001, 2004, and 2006, which improved the quality of the data [41]. For time-lapse analysis, the 1994, 2008 and 2010 acquisitions were processed in 2008 and 2010, and the 1994 data was separately reprocessed in both years. Moreover, the 2010 data was processed for both time-lapse and imaging [19, 69, 70]. To enhance seismic resolution, a 2D seismic survey was conducted in 2006 with source and receiver tow depths of 3 meters, instead of the more common depths of 6 meters and 8 meters in 3D surveys. This approach improved resolution by pushing the frequency notches beyond the spectrum of the reflected pulses from the CO2 target. The 2006 2D data could not be converted into a 3D dataset, but it demonstrated the potential for better-resolving CO2 layering in the reservoir. The data had a peak frequency of approximately 50 Hz, similar to the 2D data set. Additionally, the temporal tuning thickness was estimated to be around 7 meters, indicating enhanced resolution [17]. In the 2007 processing sequence, Tau-P deconvolution and 3D Pre-stack time-migration were used. To address the reduction in seismic velocities caused by the expansion of the CO2 plume, push-down observations were used to calculate the time-lapse stacking velocity reduction. Post-stack global matching of phase, time, amplitude, and frequency was also performed. In 2010, dual streamer data was studied using image processing and time-lapse processing, allowing for prestack wavefield separation and removal of receiver ghosts. This technique retrieved higher frequencies and achieved a peak frequency of 50 Hz, similar to the 2D dataset [17, 19]. Spectral decomposition analysis has also been employed to improve the lower resolution limit of seismic data. By utilizing a broader frequency spectrum, it allows for more detailed and precise analysis. In summary, these approaches in seismic data acquisition and analysis have been essential in increasing seismic resolution. The use of 2D surveys with specific source and receiver tow depths, image processing and time-lapse processing techniques, and advances in spectral decomposition analysis have collectively improved the resolution of seismic data and improved the ability to resolve CO2 layering in reservoirs [17–19].

The Sleipner field has inspired a multitude of research across all levels of geological heterogeneity; from simplified fluid flow numerical models [29, 71], to alternatives and more robust modeling schemes such as gravity drainage Invasion Percolation methods and advanced non-darcy fluid flow modeling pricilples [72]; to core-based studies [8, 73, 74] as well as some novel rock-physics based approaches [9, 10] leading up to an intensive seismic characterization efforts [15, 18, 70, 75, 76], all of which give way for researchers to expand their scope and seek state-of-the-art, novel and innovative solutions such as Full Waveform Inversion (FWI) [77, 78], as well as most recently machine-learning-based approaches such as [79–82].

Although the Sleipner dataset is unrivaled in the quality of the 4D study conducted, the significant challenge in interpreting the Sleipner dataset is the presence of non-repeatable noise between surveys and tuning effects in the data [81]. This noise introduces complexity and makes it difficult to distinguish the signal from the noise.

To address this, sophisticated data processing techniques and analysis methods are necessary to enhance the signal-to-noise ratio. Tuning effects further complicate the interpretation process, making it challenging to differentiate between seismic events accurately. Advanced processing algorithms and interpretation workflows are required to mitigate these effects.

Ongoing research and development efforts focus on refining data processing techniques and integrating advanced machine learning and artificial intelligence algorithms. These advancements aim to reduce the impact of nonrepeatable noise and improve the resolution and accuracy of interpretations. With advances in modern computing and seismic reservoir characterization, more integration work has been published recently such as the work done by [82], where the authors have tested a Joint Inversion of seismic data from Sleipner and synthetic resistivity data within a tensor flow machine learning scheme utilizing a simplified version of the rock physics models proposed by [8–10]. The work of [79] approaches the same Sleipner dataset with a convolutional neural network to extract 4D signals, while the work of [81] proposed a joint inversion-segmentation approach inverting for Ip models of the monitor and the base of the Sleipner data set based on a segmentation approach using the PyLops Python package.

Our proposed methodology was implemented on the Sleipner dataset by applying the necessary steps described in chapter 3. The Sleipner data set is retrieved from the CO2 data share [83], where there is a variety of data included in the data set. In addition to different processing of the seismic data, included within the data surfaces for the base of the Utsira formation, the top Utsira, thick shale, and finally the most famous sand-wedge L9, the final resting place of the Co2; along with the aforementioned surfaces, less confident surfaces of the intraformational subseismic resolution shale baffles, which is one of the main driving forces for the multilayer distributions arrangement of the CO2 plume.

Also provided in the data set are interval velocity data and interval velocity models prior to and post-injection, it is worth mentioning that the monitor velocity cubes are from 2013. Using the high confidence interperation of Top Sandwdge L9 and base Utsira formation surfaces to calculate reservoir thickness and translate the Top sand wedge up with half of the wavelet, 85 ms half of a 170 ms wavelet, after which the new translated L9 is copied and then translated downwards 510 ms seconds to form the base of our inversion grid. After the grinding, layering, well log upscaling, and seismic resampling our inversion model has the following dimensions 249 x 468 x 255 in the i, j, and k directions, respectively. It is important to note that we are using the same grid to model both inversion algorithms to be implemented in the thesis using the 2007 processed Sleipner data, as it is the one with the most seismic vintages in one processing, 1994, 2001, 2004 and 2006 data. Both methods implemented in this thesis have been executed with 6 iterations of 32 simulations each which provide the necessary input for further uncertainty assessment of the performance of algorithms.

It can be seen in fig. 4.1, the histograms of inverted Ip compared to well Ip from the both inversion methods and the detailed statistics can be found in the appendix in table A.2. The histogram form both methods shows that the inverted Ip models are honoring the experimental data from the well as they have the same minimum and maximum values, the reproduction of the mean Ip as inferred form the well log, and as well as the reduction of the variance in the model. The Ip variance in the GSI 4D compared to that of the GSI shows a reduction in the model variance, while the variance in Ip difference is higher in the GSI 4D than that of the GSI

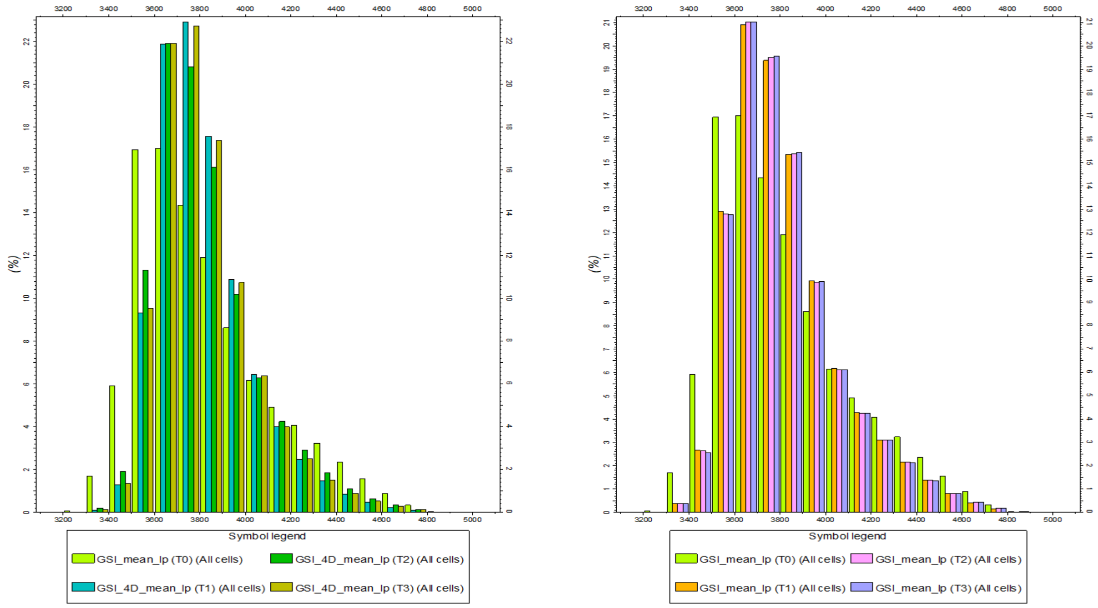

(a) Histogram GSI 4D

(b) Histogram GSI

Figure 4.1: Histogram Acoustic Impedance

The distribution shown in fig. 4.2 and table A.6 depict the histogram and statistics for Acoustic Impedance Similarity (bestccAI6) of both methods. The key takeaways are the concentration of high similarity values higher than 50 percent highlighting the ability of both methods to retrieve Ip traces that generate high similarity with the measured seismic response. While fig. 4.3 shows the histogram of synthetic seismic from both methods and table 4.1 compares the statistics to that of the respective real seismic data, where we can notice the differences in the minimum and maximum values from the synthetic of both methods and the real seismic, these differences also contribute to some visualization drawbacks as the color scales need to incorporate the global minimum and maximum to be valid for comparison of different properties. fig. 4.4 and table A.7 shows the Mean-CC histogram and descriptive statistics results respectively, which are the similarity between the generated synthetic seismic from the mean Ip model of the sixth iteration and the observed seismic. Similar to bestccAI6 results, it can be seen that the values are high and the majority is above 50 percent, highlighting the performance of both algorithms.

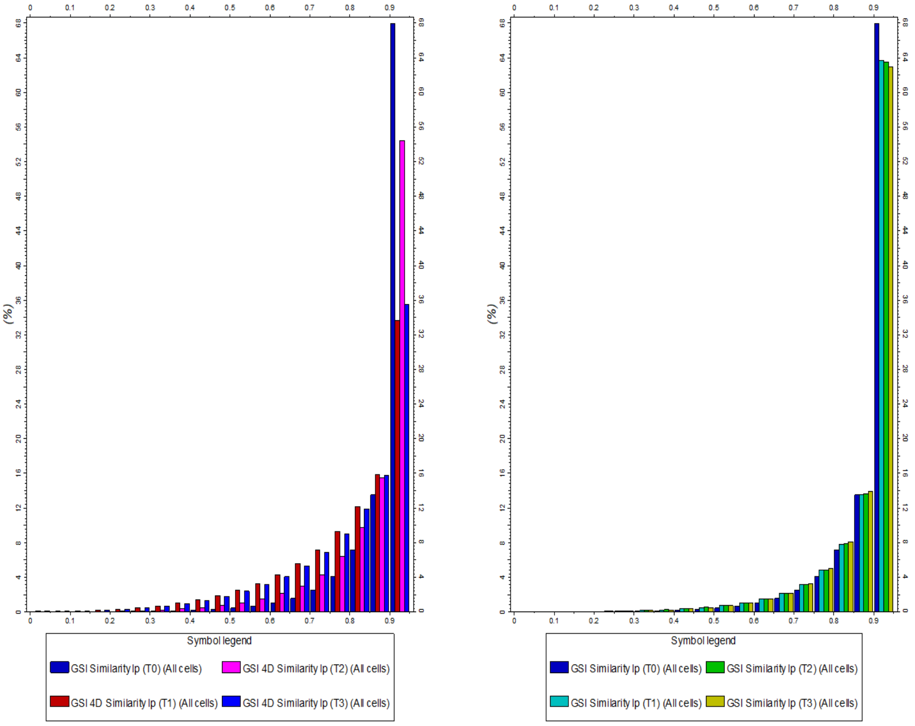

(a) GSI 4D

(b) GSI

Figure 4.2: Histogram similarity Ip

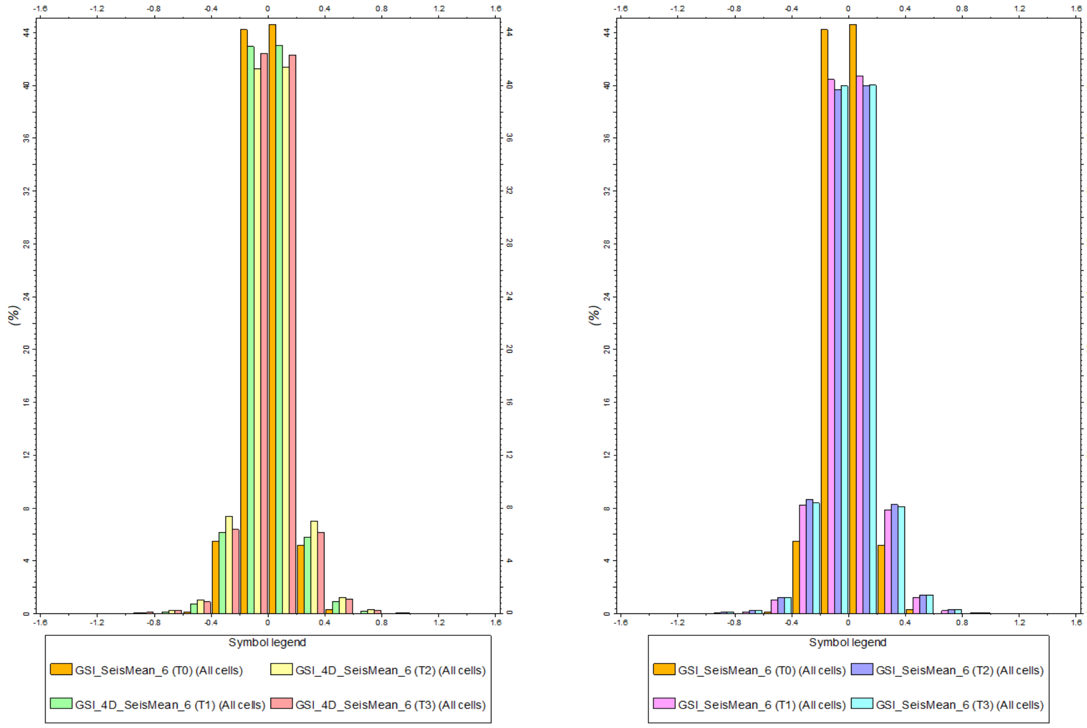

(a) GSI 4D

(b) GSI

Figure 4.3: Histogram Seismic

Figure fig. 4.5 show the spatial continuity revealing variograms in the major and minor directions, as described in chapter 3, for 1994, 2001, 2004, and 2006 seismic data respectively, which are crucial for any geostatistical study.

Table 4.1: Seismic

Name	Type	Min	Max	Delta	N	Mean	Std	Var	Sum
GSI_SeisMean_6 (T0)	Cont.	-0.59	0.63	1.22	29696535	0	0.13	0.02	-240.94
GSI_4D_SeisMean_6 (T1)	Cont.	-1.22	1.24	2.46	29696535	0	0.15	0.02	1556.03
GSI_SeisMean_6 (T1)	Cont.	-1.23	1.24	2.47	29696535	0	0.17	0.03	2112.4
GSI_4D_SeisMean_6 (T2)	Cont.	-1.33	1.33	2.66	29696535	0	0.17	0.03	-3197.93
GSI_SeisMean_6 (T2)	Cont.	-1.35	1.31	2.67	29696535	0	0.18	0.03	-1936.96
GSI_4D_SeisMean_6 (T3)	Cont.	-1.28	1.35	2.62	29696535	0	0.16	0.03	-5908.04
GSI_SeisMean_6 (T3)	Cont.	-1.32	1.34	2.66	29696535	0	0.18	0.03	-4237.69
RealSeismic (T0)	Cont.	-3.44	2.63	6.08	29696535	0	0.16	0.03	1423.29
RealSeismic (T1)	Cont.	-3.41	2.74	6.15	29696535	0	0.18	0.03	6455.36
RealSeismic (T2)	Cont.	-3.35	2.75	6.09	29696535	0	0.2	0.04	16771.07
RealSeismic (T3)	Cont.	-3.65	2.94	6.58	29696535	0	0.21	0.04	18530.6

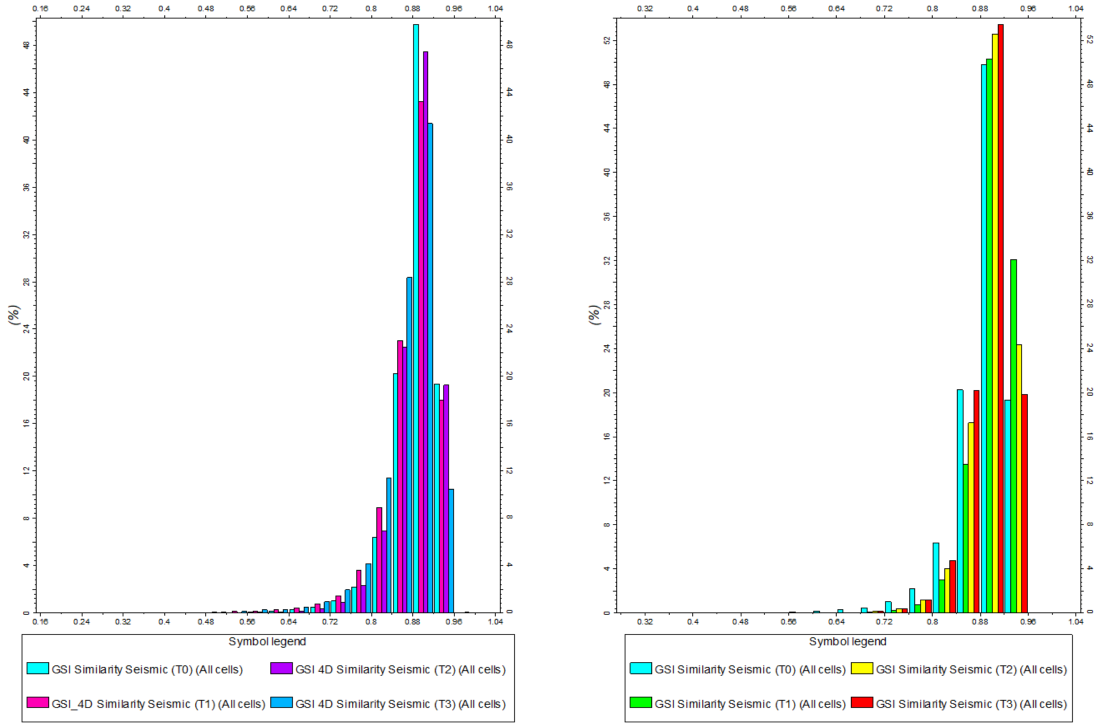

(a) Histogram MeanCC GSI 4D

(b) Histogram MeanCC GSI

Figure 4.4: Histogram MeanCC

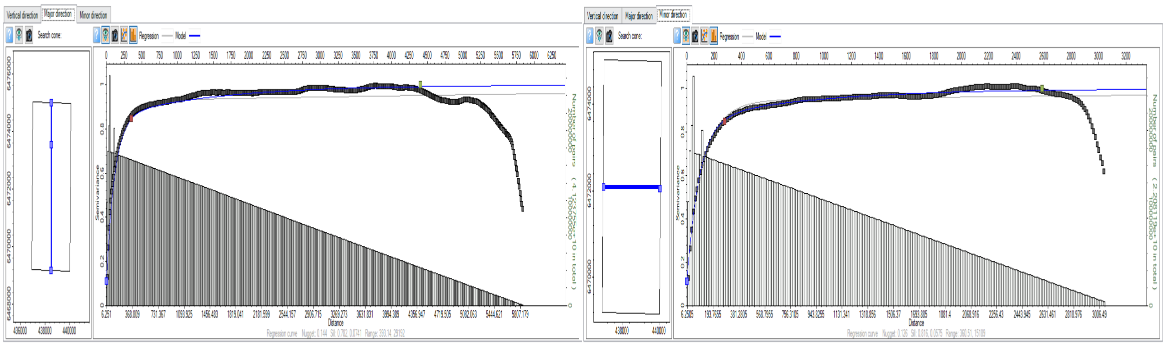

(a) Variogram Major 1994 **(b)** Variogram Minor 1994

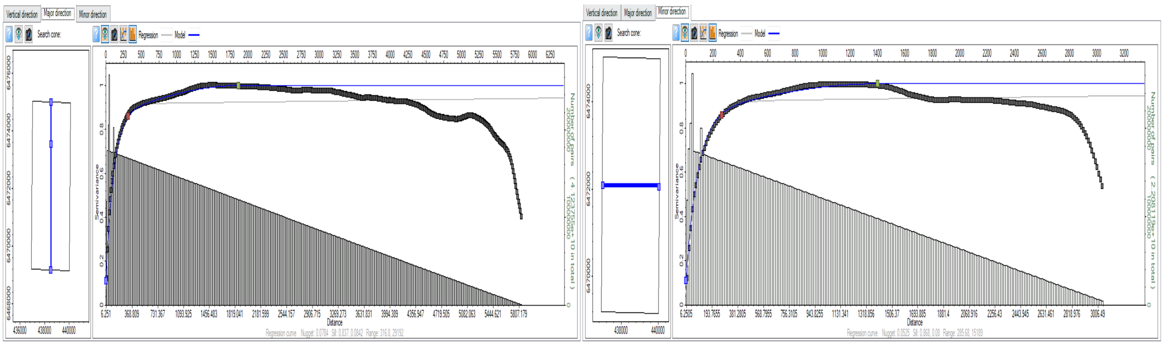

(c) Variogram Major 2001 **(d)** Variogram Minor 2001

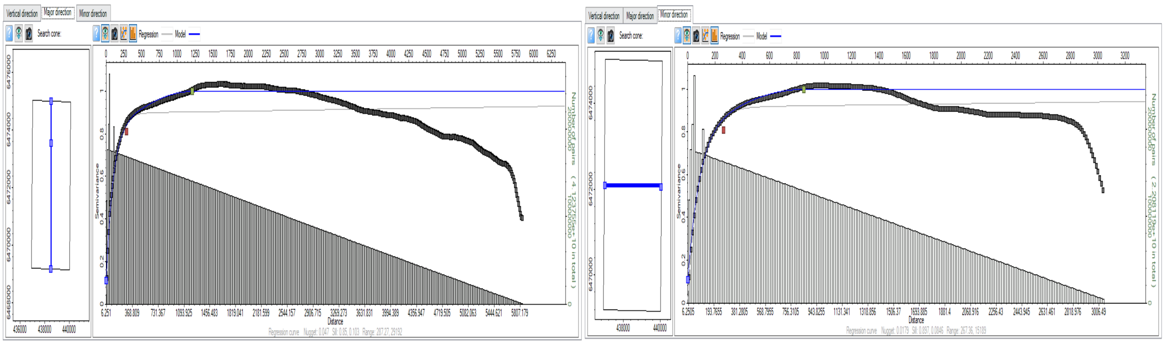

(e) Variogram Major 2004 **(f)** Variogram Minor 2004

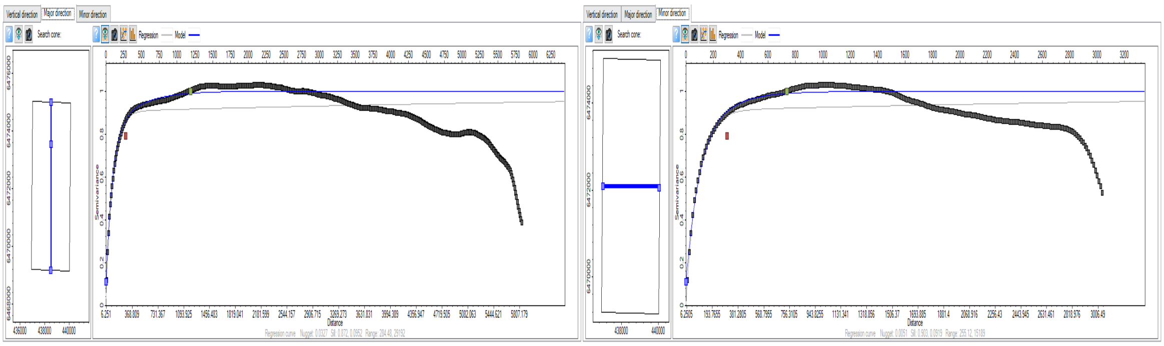

(g) Variogram Major 2006 **(h)** Variogram Minor 2006

Figure 4.5: Variogram 1994

Next section we will go through the results from GSI 4D, from all years in the study, examining the Ip and the corresponding best similarity coefficients along with the generated synthetic seismic and the corresponding Mean similarity coefficient between real and synthetic seismic. Then we will process and examine the results; first, we compare the real seismic with the synthetic seismic generated, then we compare the observed, that is, the real 4D difference subtracting the real base minus the real monitor, and the predicted 4D difference, the real base minus synthetic monitor, which is the essence of our proposed methodology objective function driving the convergence of the iterative procedure; lastly, we show the Ip base subtracted from the Ip monitor along with the point-wise variance.

4.2 Geostatistical Seismic Time Lapse (4D) Inversion

In this section, we will use the point of views in fig. 4.6 to present all the results from this thesis in a cross-section, plan view from layer 9 and layer 5 respectively. In the cross section, it shows well 15-9-13, the top bold line represents layer 9, the middle line represents layer 5 and bottom bold line represents the base of the utsira formation, converted using the 2013 velocity model provided, which is critical for analyzing the performance of both methods, giving a reference to velocity pushdown effects. In the plan veiw, it shows the location if the well relative to the plume outline from the 2010 monitor survey as well as highlights the location of the corss section utilized.

In this thesis we have used the following naming convention for our properties, first is the inversion method implemented GSI and GSI 4D then followed with the property name then followed with the time steps. The Ip is meanIp (Tn), Synthetic Seismic is SeisMean6, difference in Ip diff Ip (Tn), difference in seismic real is Real4D (Tn) and syntheic Synth 4D , Ip and seismic similiarities are best_CC_A6 (Tn)and meanCC (Tn) , respectively. The CO2 injection into the formation causes the reduction in the Ip values. Thus, the subtraction of the monitor from the base will be represented as a hard event signature in the 4D seismic signal.

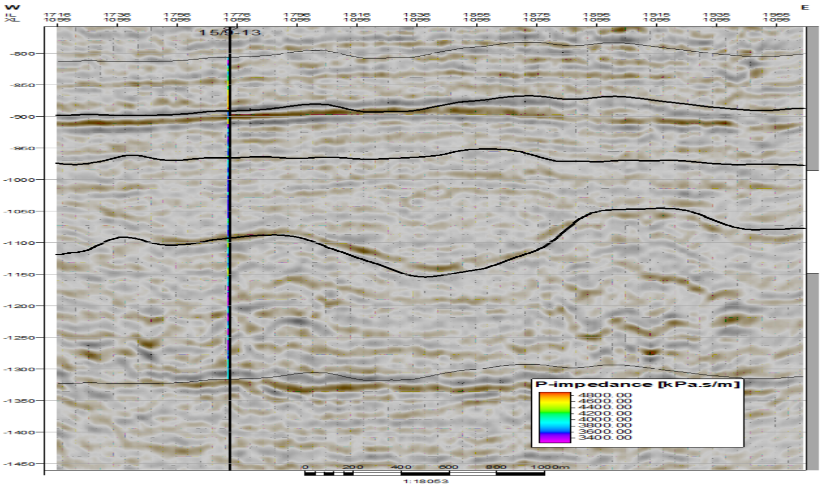

(a) Cross Section

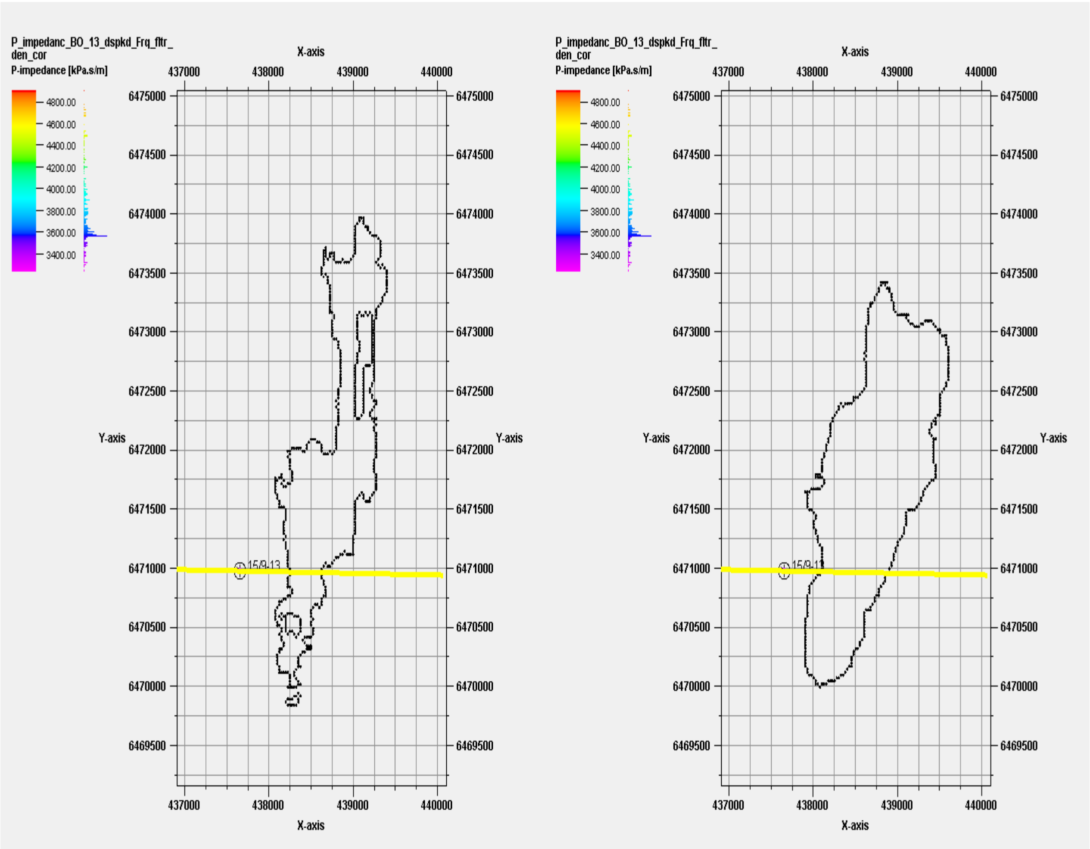

(b) Plan View L9

(c) Plan View L5

Figure 4.6: Results Display Positions.

4.2.1 Inversion

In figure 4.7 we can see the inversion results of the base seismic inversion for Ip from 1994 prior to injection, along with synthetic seismic and as well as the best CC Ip from the sixth iteration, and figure 4.8 shows real and synthetic for the baseline survey from the south, then the top view of Top Sand wedge L9 and the base of the shale layer L5 and overlain with the plume boundaries from 2010 provided in the data set.

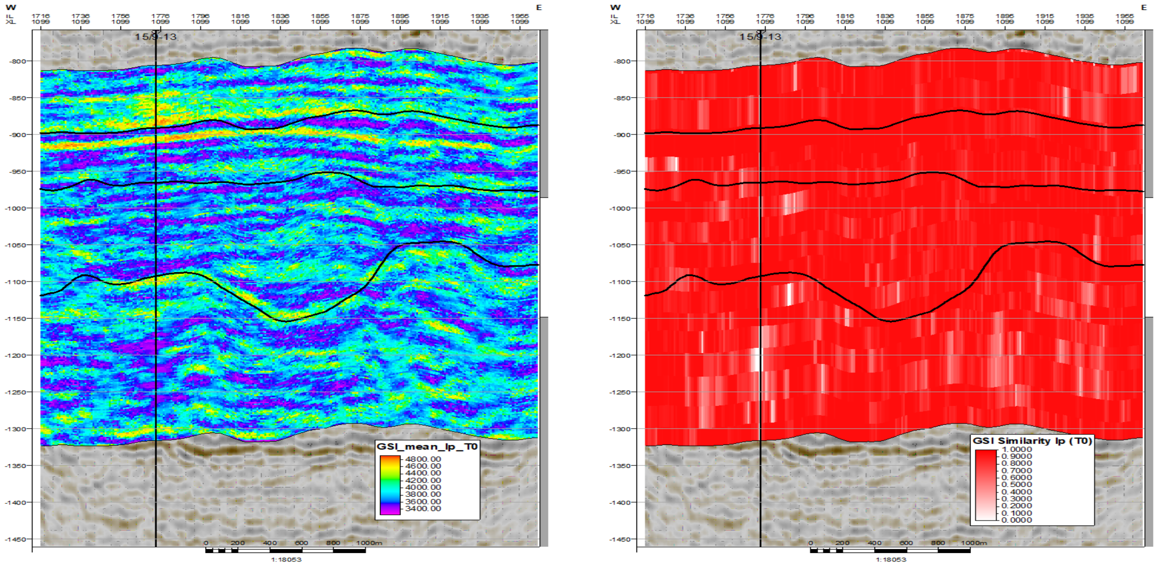

(a) Ip 1994 GSI 4D

(b) Similarity Ip 1994 GSI 4D

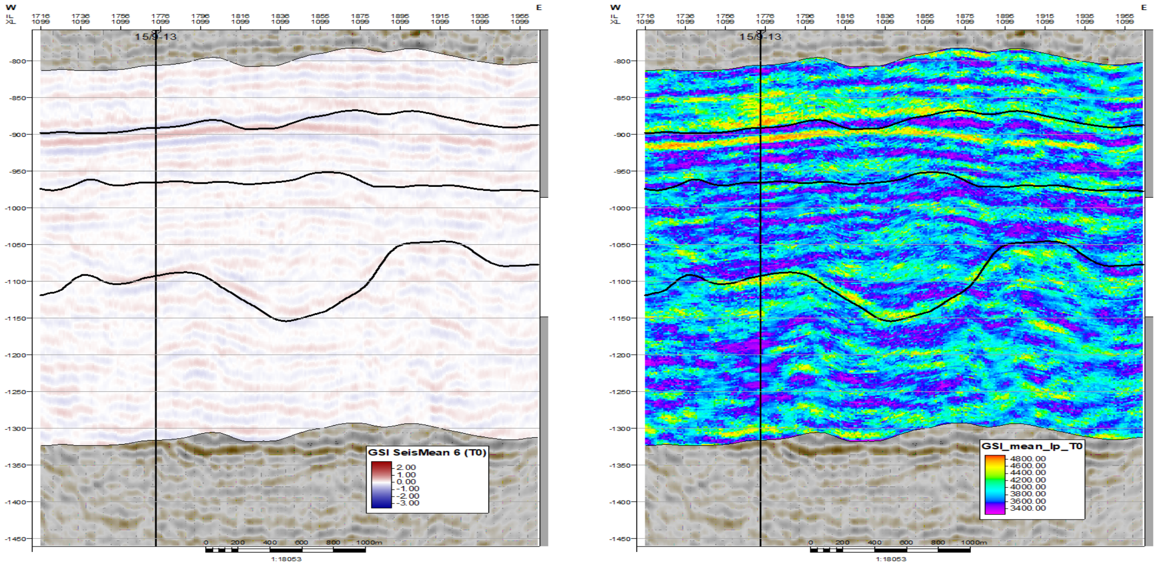

(c) Synthetic Seismic 1994 GSI 4D

(d) Mean CC 1994 GSI 4D

Figure 4.7: Inversion Results 1994 GSI 4D

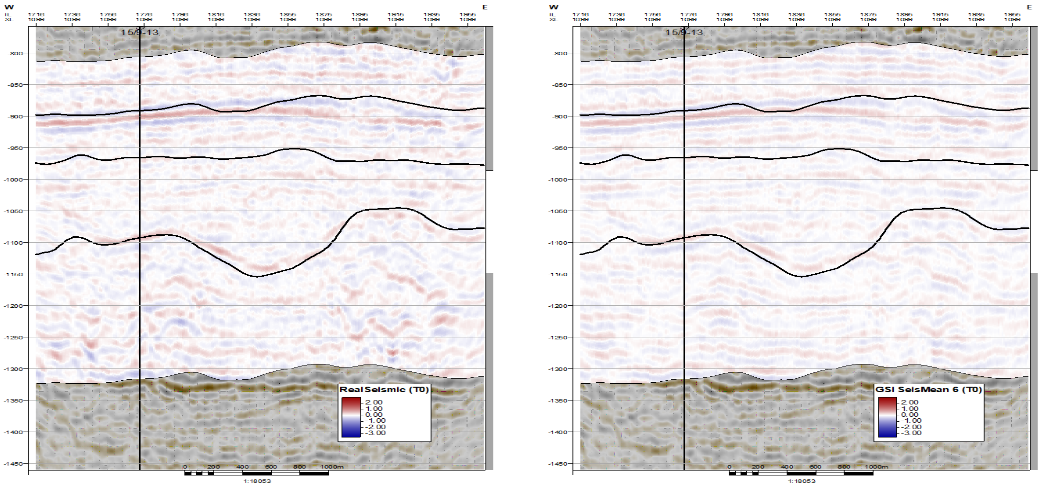

(a) Real Seismic 1994

(b) Synthetic Seismic 1994 GSI4D

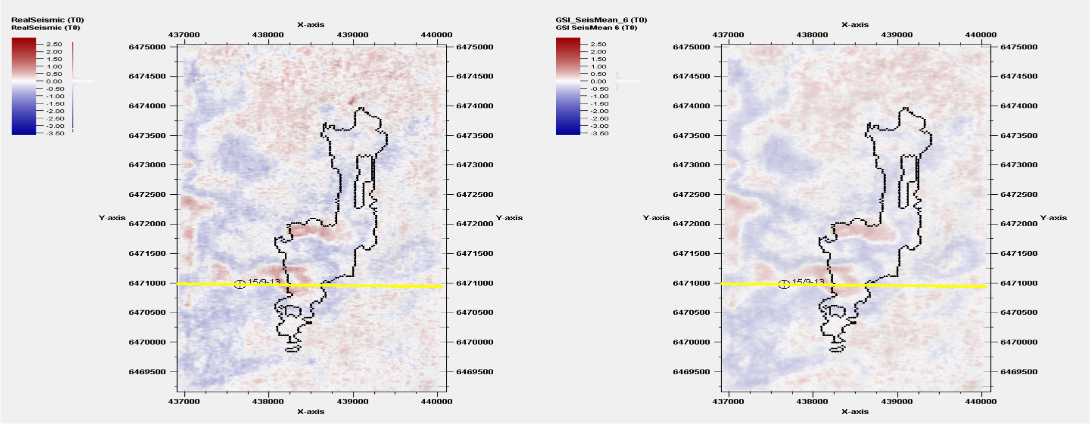

(c) Real Seismic 1994 L9

(d) Synthetic Seismic 1994 L9 GSI 4D

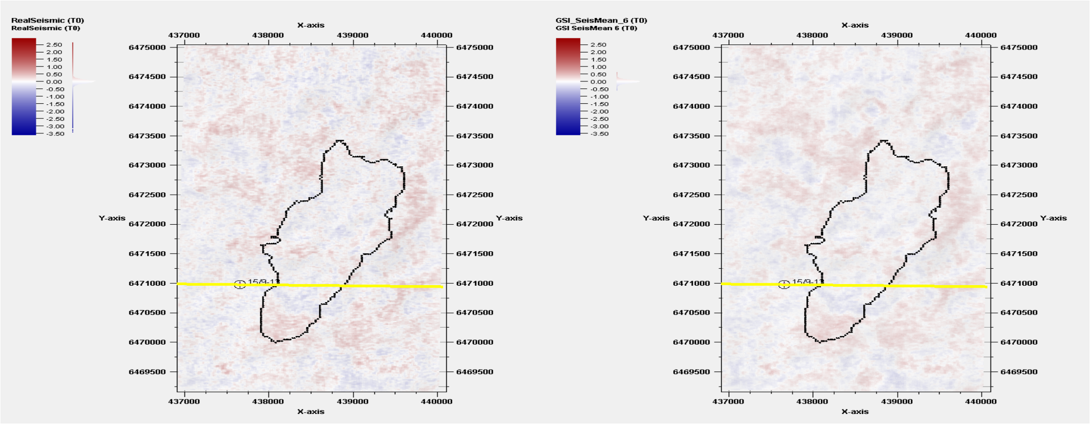

(e) Real Seismic 1994 L5

(f) Synthetic Seismic 1994 L5 GSI 4D

Figure 4.8: GSI 4D 1994 Results L9 L5

4.9, 4.10, and 4.11, show the inversion results of 2001, 2004, and 2006 monitors from the south, respectively. All these figures have 3 distinct features; first is the inversion of high resolution Ip models highlighting the internal architecture of the formation's interbedded interformational shales, second are the high values of both best cc Ip and mean CC and the corresponding synthetic seismic which is of great quality, especially with the increase of the CO2 saturation. While 4.12, 4.13, and 4.14, show the inversion results of 2001, 2004, and 2006 monitors from a top view of layers 9 and 5, respectively.

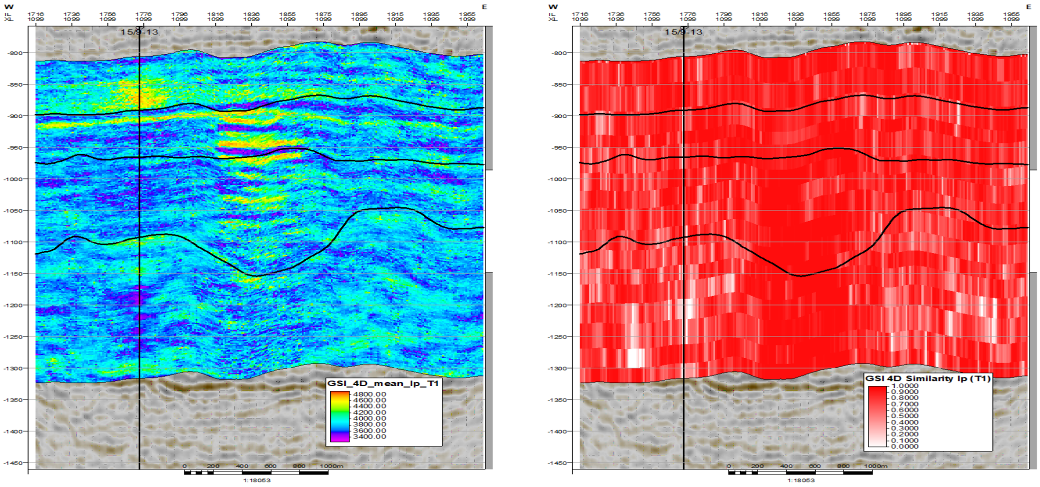

(a) Ip 2001 GSI 4D

(b) Similarity Ip 2001 GSI 4D

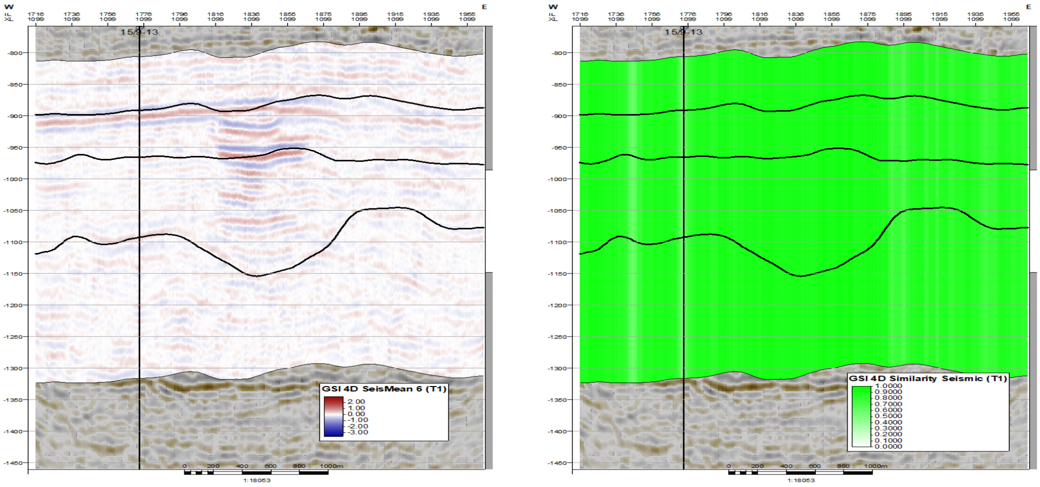

(c) Synthetic Seismic 2001 GSI 4D

(d) Mean CC 2001 GSI 4D

Figure 4.9: Inversion Results 2001 GSI 4D

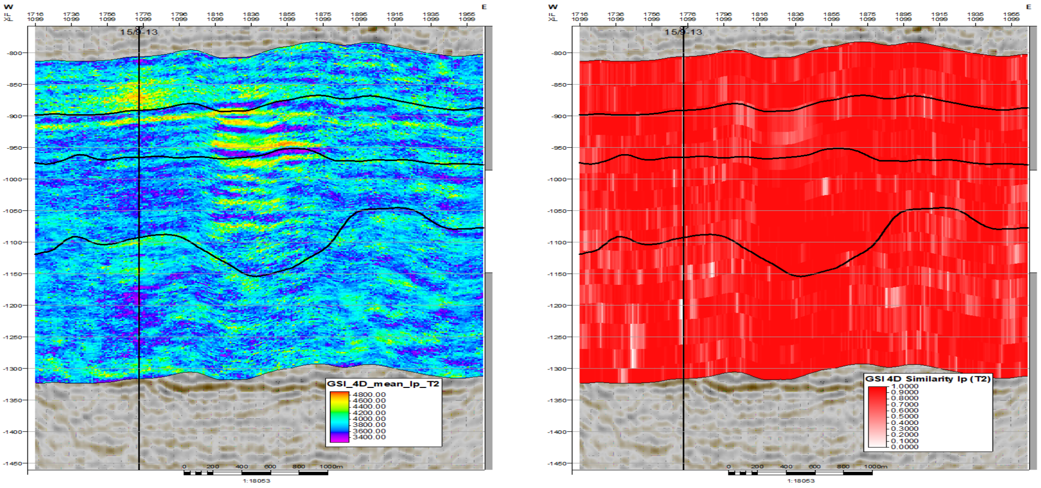

(a) Ip 2004 GSI 4D

(b) Similarity Ip 2004 GSI 4D

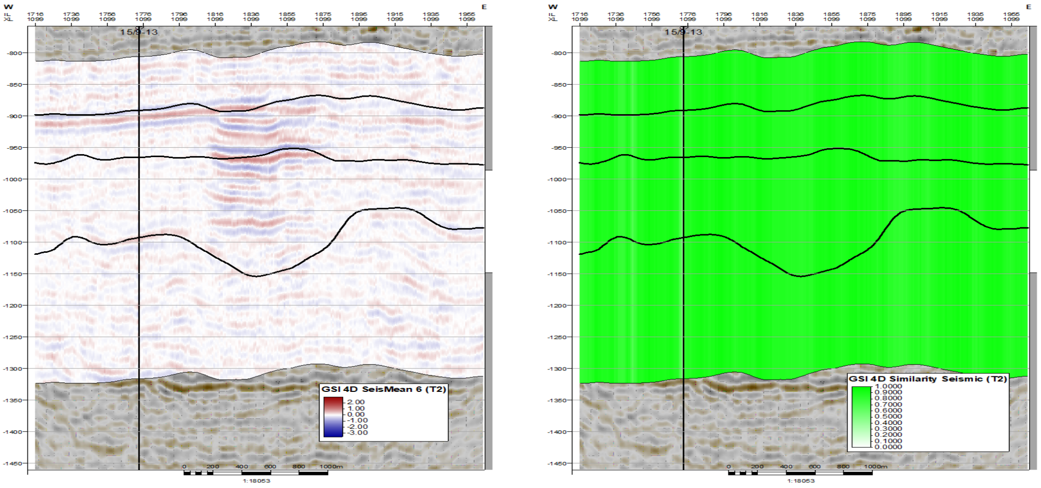

(c) Synthetic Seismic 2004 GSI 4D

(d) Mean CC 2004 GSI 4D

Figure 4.10: Inversion Results 2004 GSI 4D

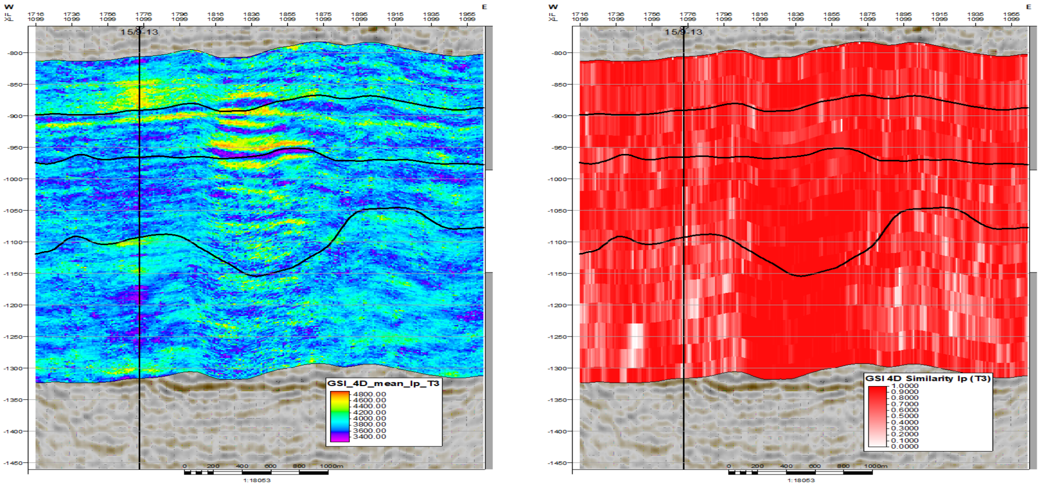

(a) Ip 2006 GSI 4D **(b)** Similarity Ip 2006 GSI 4D

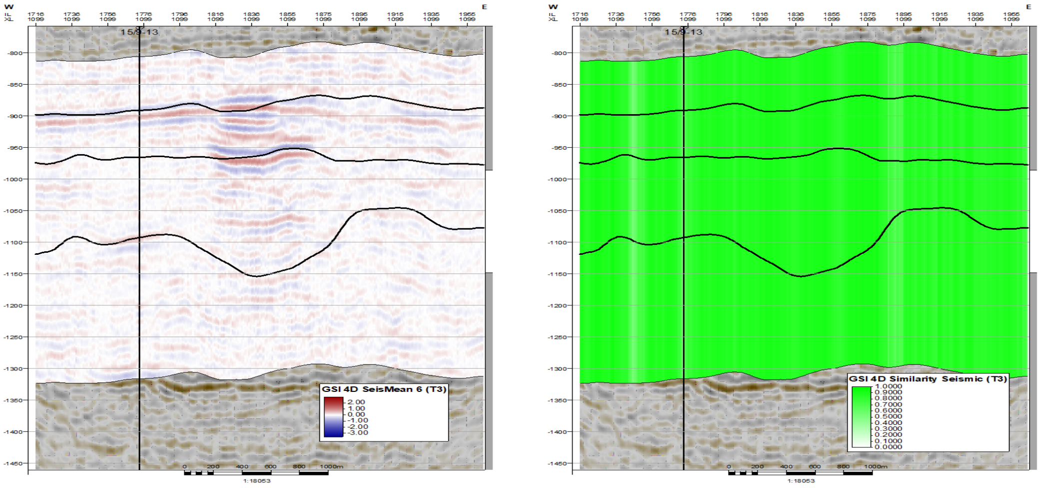

(c) Synthetic Seismic 2006 GSI 4D **(d)** Mean CC 2006 GSI 4D

Figure 4.11: Inversion Results 2006 GSI 4D

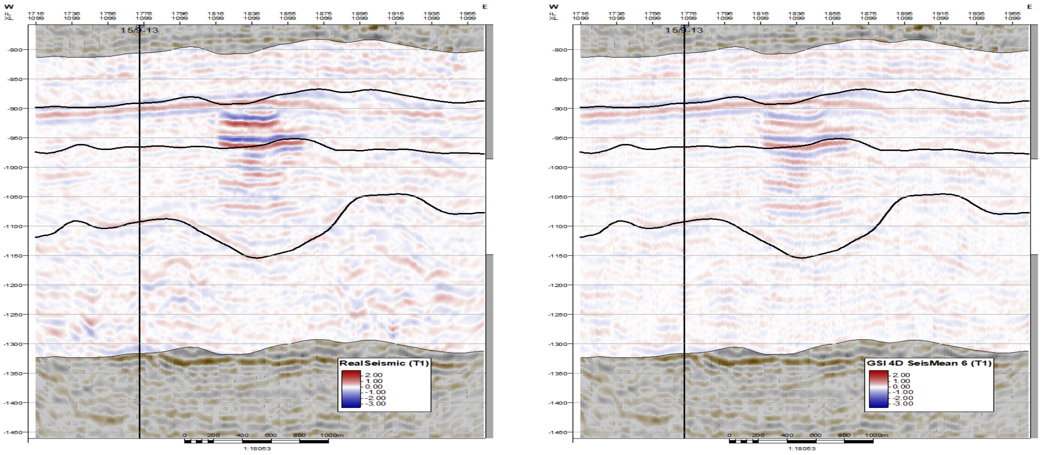

(a) Real Seismic 2001 **(b)** Synthetic Seismic 2001 GSI 4D

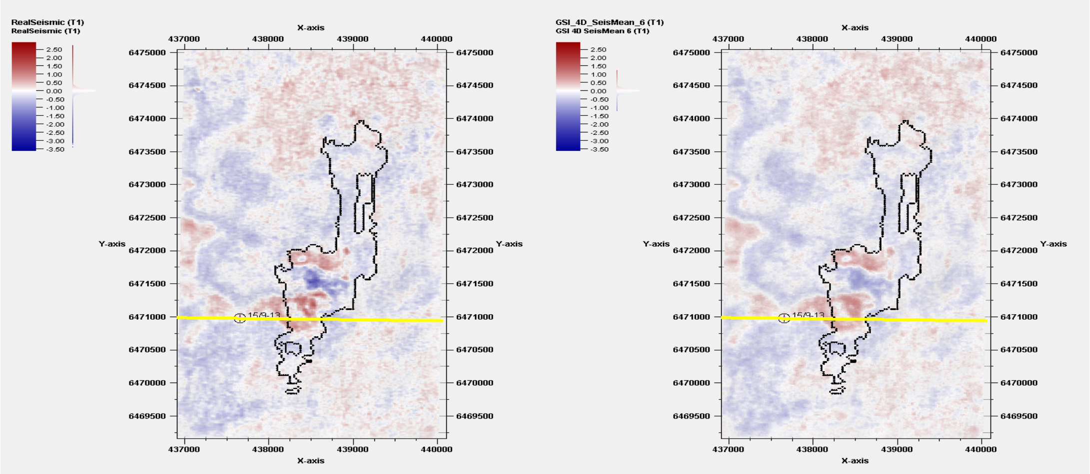

(c) Real Seismic 2001 L9 **(d)** Synthetic Seismic 2001 L9 GSI 4D

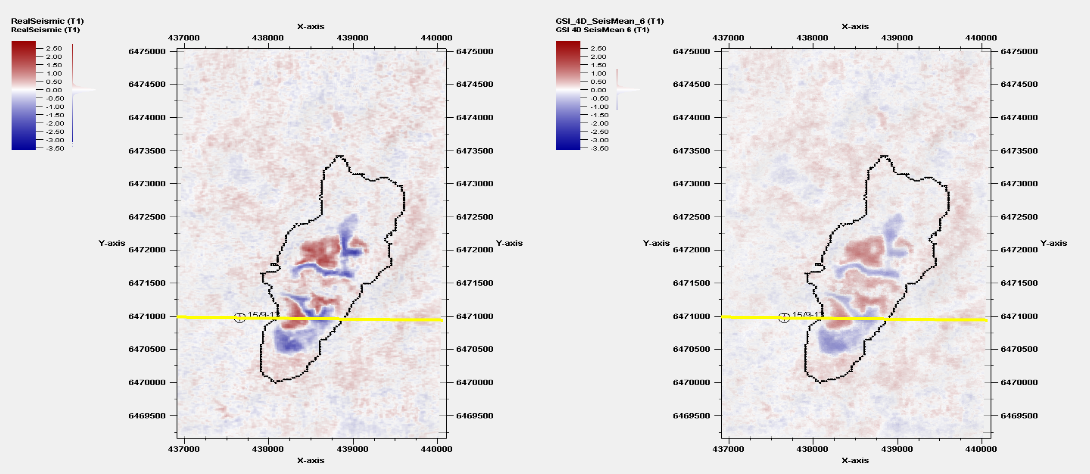

(e) Real Seismic 2001 L5 **(f)** Synthetic Seismic 2001 L5 4D

Figure 4.12: GSI 4D 2001 Results L9 L5

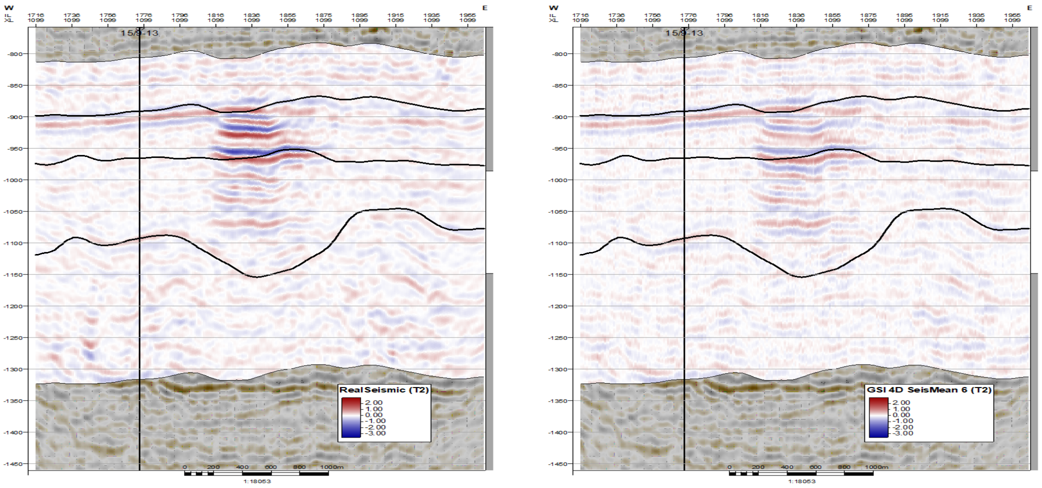

(a) Real Seismic 2004 **(b)** Synthetic Seismic 2004 GSI 4D

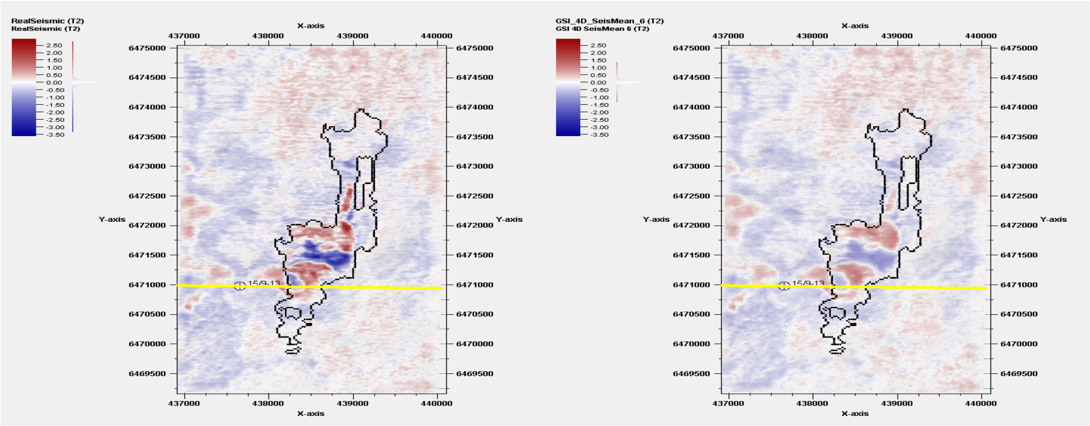

(c) Real Seismic 2004 L9 **(d)** Synthetic Seismic 2004 L9 GSI 4D

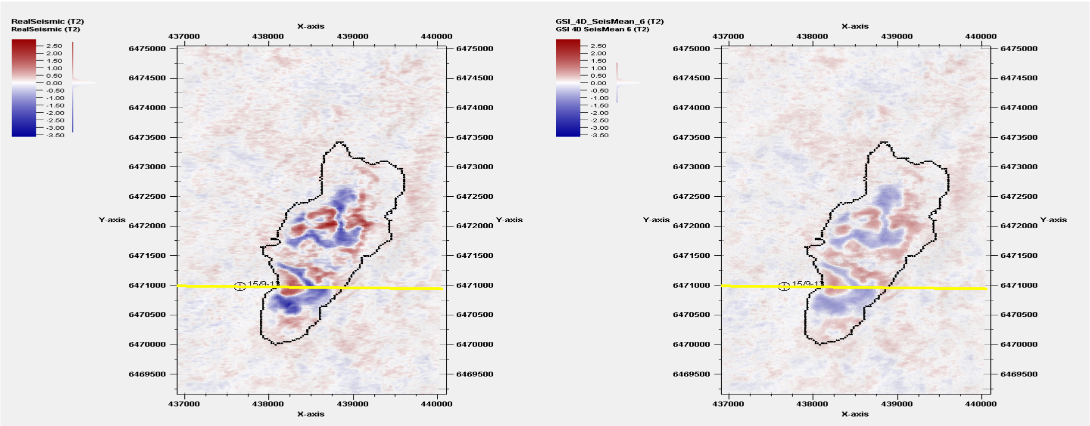

(e) Real Seismic 2004 L5 **(f)** Synthetic Seismic 2004 L5 4D

Figure 4.13: GSI 4D 2004 Results L9 L5

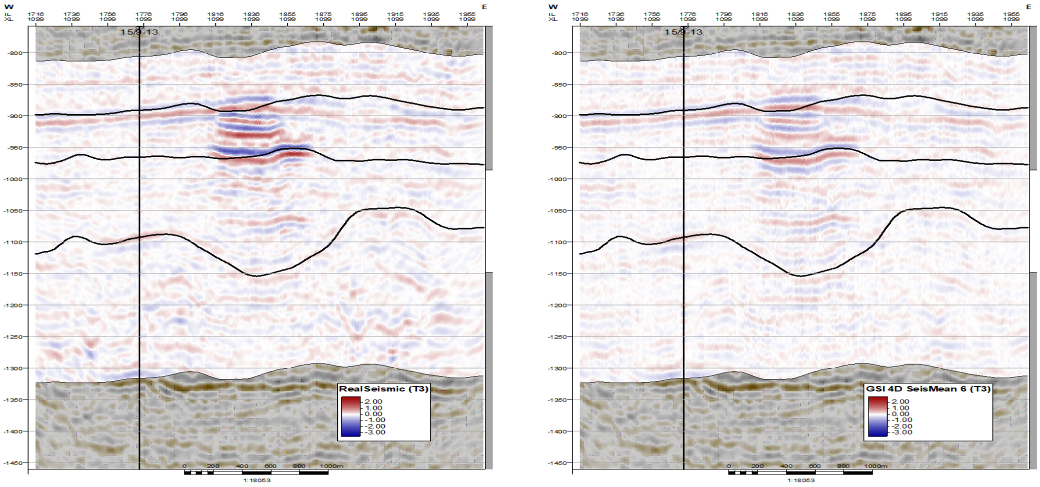

(a) Real Seismic 2006 **(b)** Synthetic Seismic 2006 GSI 4D

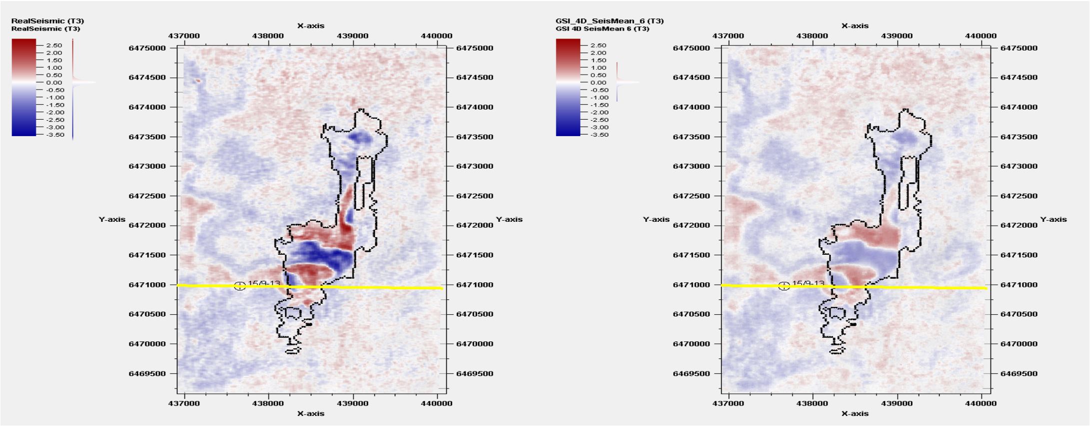

(c) Real Seismic 2006 L9 **(d)** Synthetic Seismic 2006 L9 GSI 4D

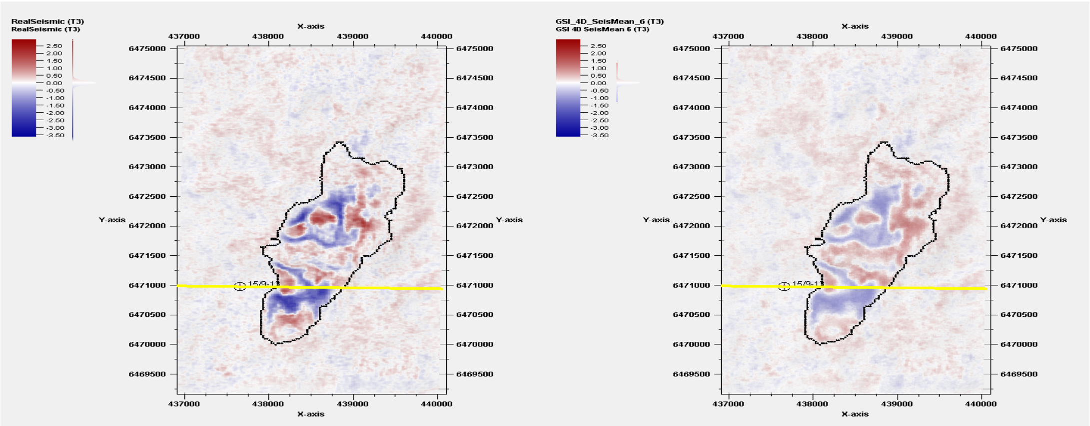

(e) Real Seismic 2006 L5 **(f)** Synthetic Seismic 2006 L5 4D

Figure 4.14: GSI 4D 2006 Results L9 L5

It can be seen in figures 4.15 and 4.16; the results from 2001 showing the real seismic compared with GSI synthetic seismic, the observed, ie. real 4D difference subtracting real base minus real monitor, and the predicted 4D difference, real base minus synthetic monitor, and show the Ip base subtracted from the Ip monitor along with the point-wise variance, with a view from the south and top view of base shale layer L5 respectively.

It can be seen in figures 4.17 and 4.18; the results from 2004 showing the real seismic compared with GSI synthetic seismic, the observed, ie. real 4D difference subtracting real base minus real monitor, and the predicted 4D difference, real base minus synthetic monitor, and show the Ip base subtracted from the Ip monitor along with the point-wise variance, with a view from the south and top view of base shale layer L5 respectively.

It can be seen in figures 4.19 and 4.20; the results from 2006 showing the real seismic compared with GSI synthetic seismic, the observed, ie. real 4D difference subtracting real base minus real monitor, and the predicted 4D difference, real base minus synthetic monitor, and show the Ip base subtracted from the Ip monitor along with the point-wise variance, with a view from the south and top view of base shale layer L5 respectively.

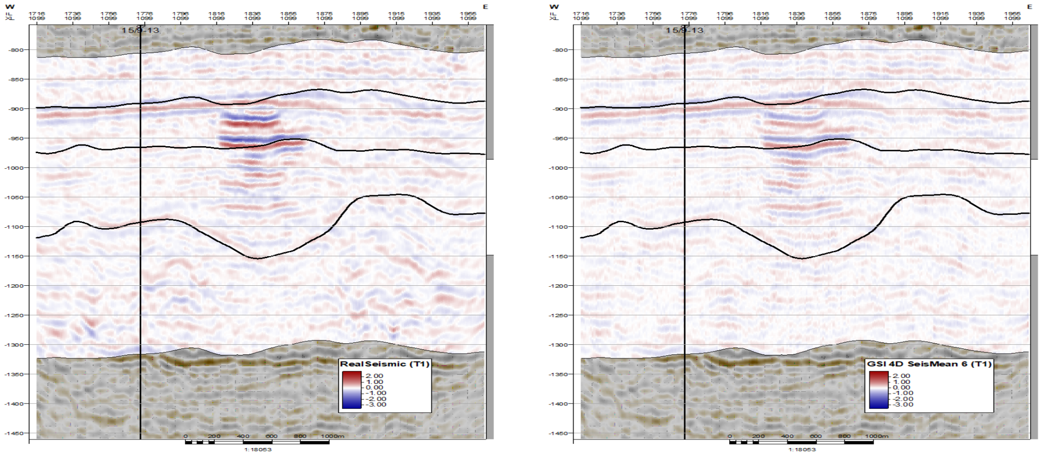

(a) Real Seismic 2001

(b) Synthetic Seismic 2001 GSI 4D

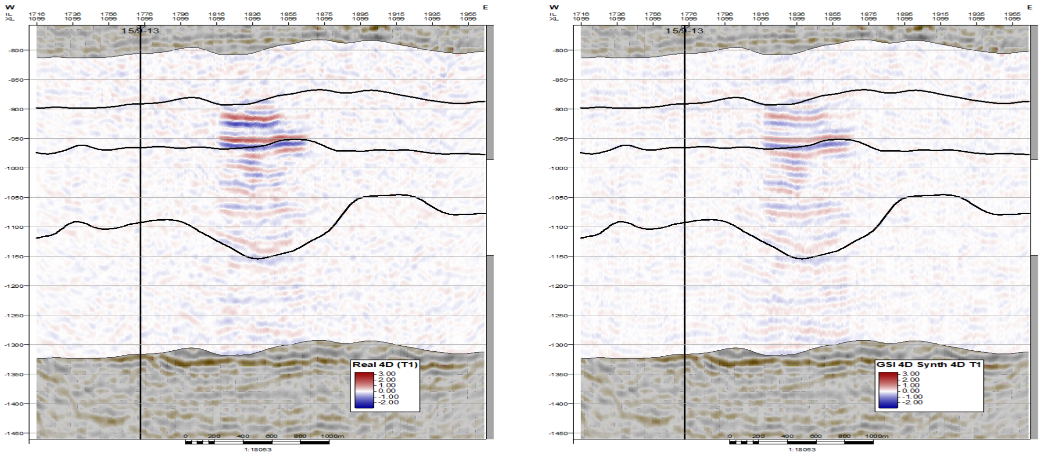

(c) Real Seismic Base minus Real Seismic Monitor

(d) Real Seismic Base minus Synthetic Seismic Monitor 2001 GSI 4D

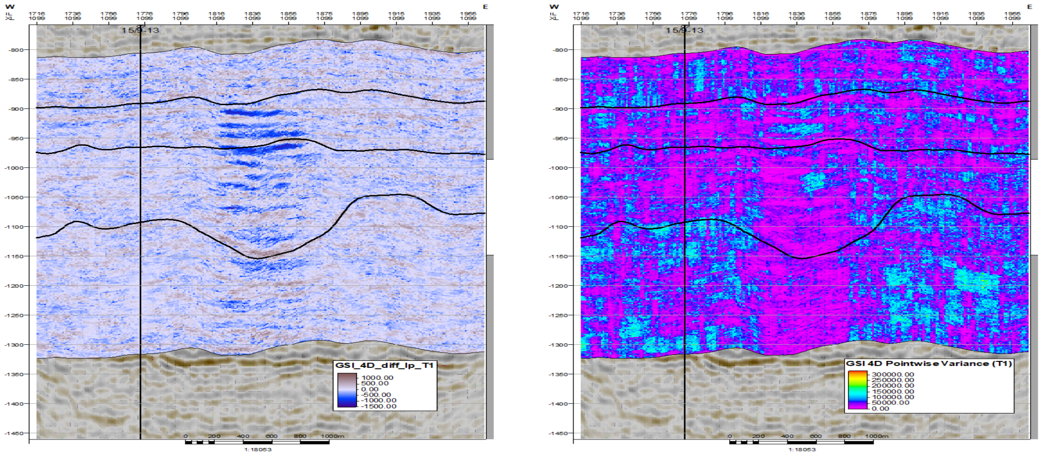

(e) Ip Base minus Ip Monitor 2001 GSI 4D

(f) Point-wise Variance

Figure 4.15: Processing GSI 4D 2001 Results

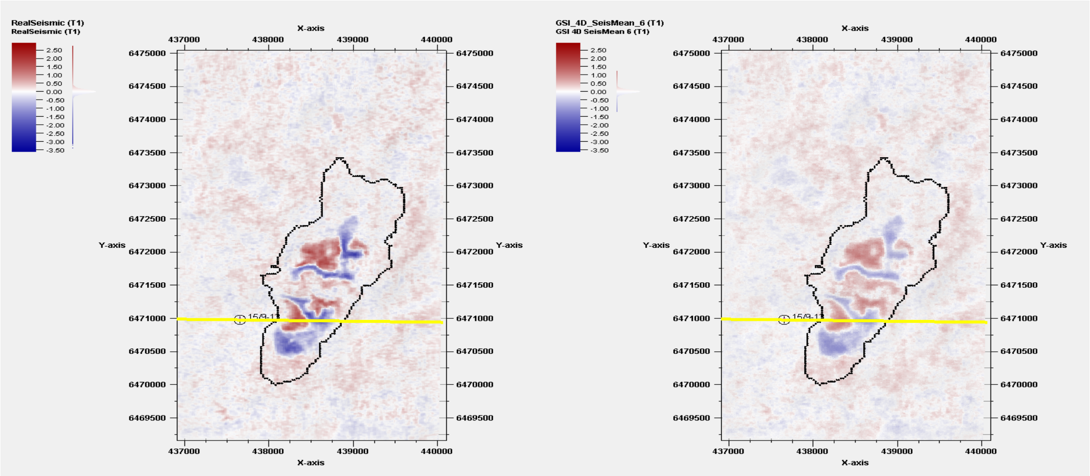

(a) Real Seismic 2001

(b) Synthetic Seismic 2001 GSI 4D

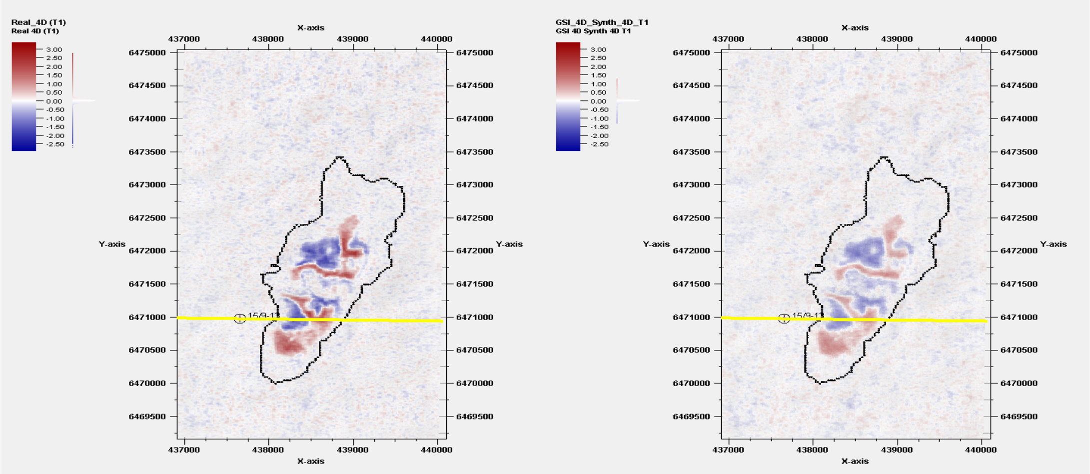

(c) Real Seismic Base minus Real Seismic Monitor

(d) Real Seismic Base minus Synthetic Seismic Monitor 2001 GSI 4D

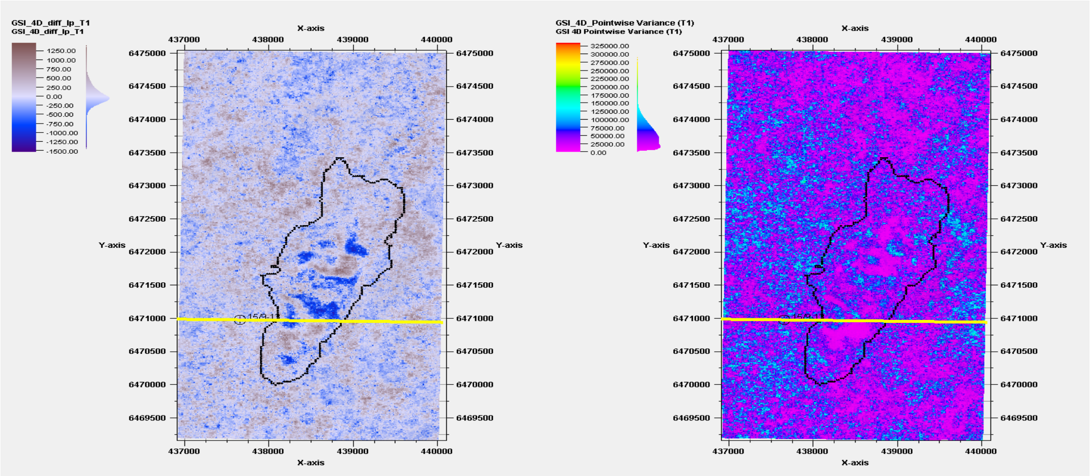

(e) Ip Base minus Ip Monitor 2001 GSI 4D

(f) Point-wise Variance

Figure 4.16: Processing GSI 4D 2001 Results L5

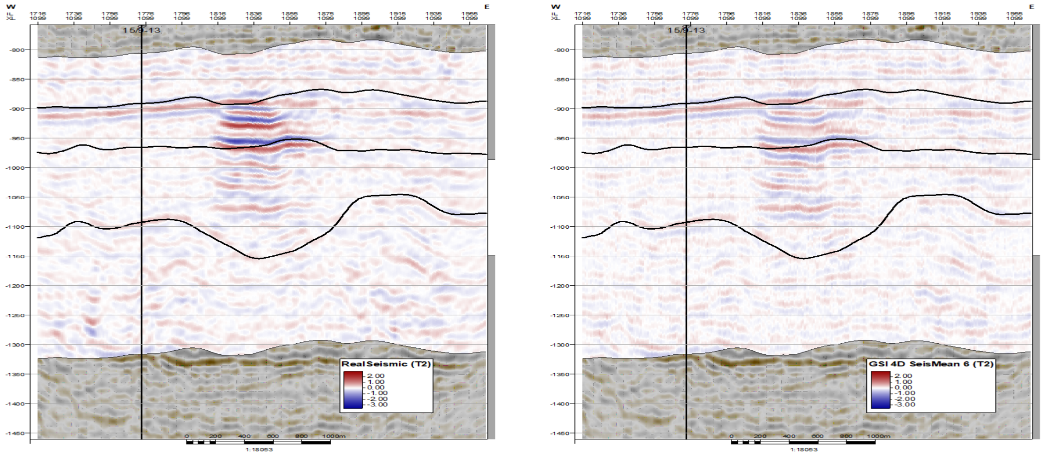

(a) Real Seismic 2004

(b) Synthetic Seismic 2004 GSI 4D

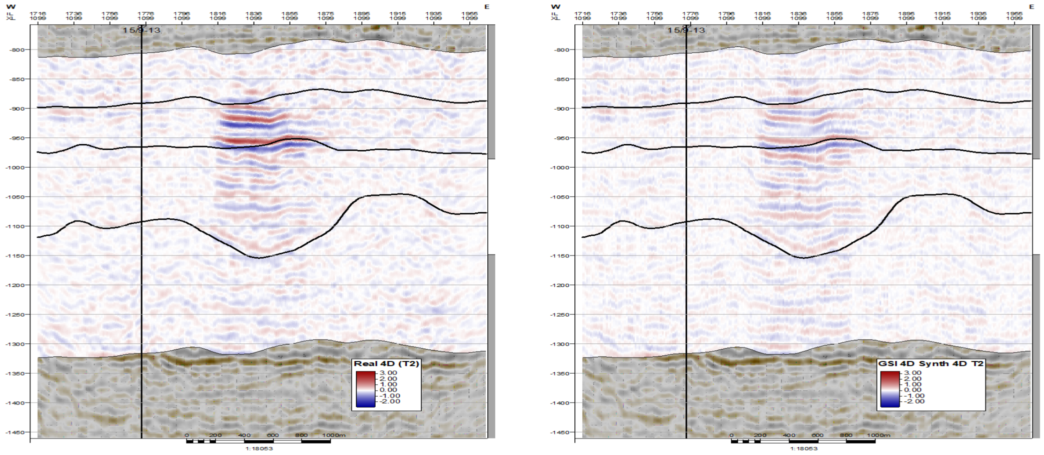

(c) Real Seismic Base minus Real Seismic Monitor

(d) Real Seismic Base minus Synthetic Seismic Monitor 2004 GSI 4D

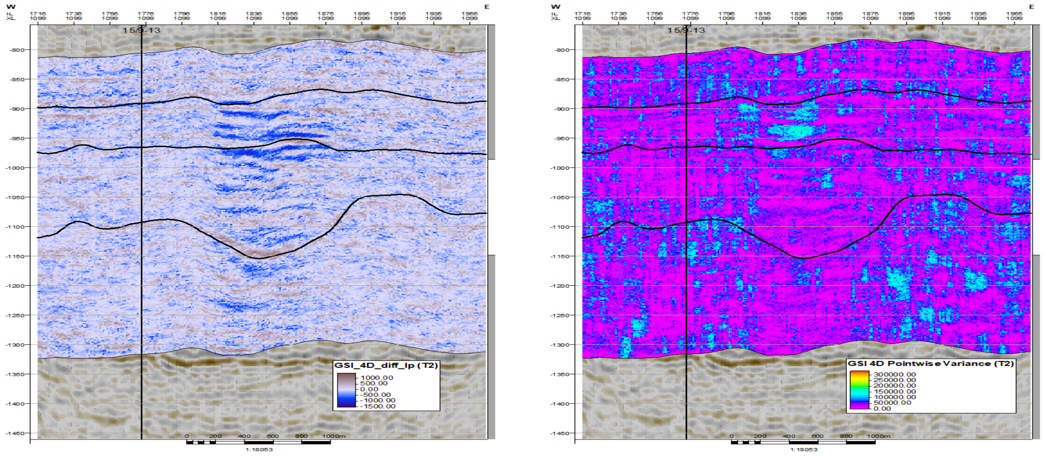

(e) Ip Base minus Ip Monitor 2004 GSI 4D

(f) Point-wise Variance

Figure 4.17: Processing GSI 4D 2004 Results

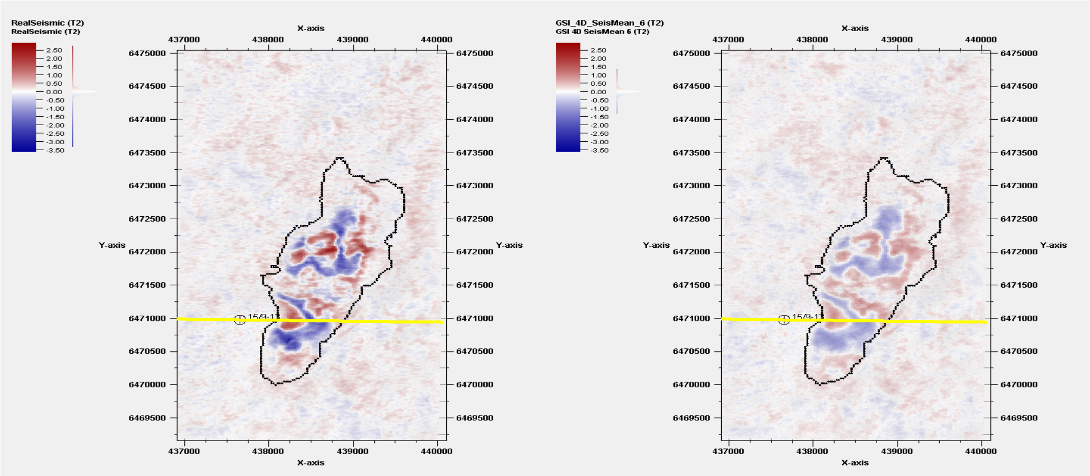

(a) Real Seismic 2004

(b) Synthetic Seismic 2004 GSI 4D

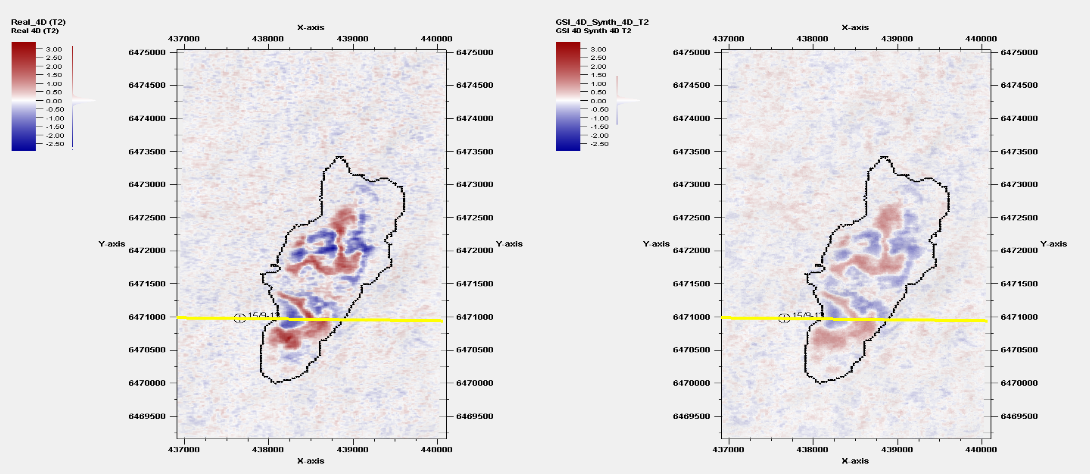

(c) Real Seismic Base minus Real Seismic Monitor

(d) Real Seismic Base minus Synthetic Seismic Monitor 2004 GSI 4D

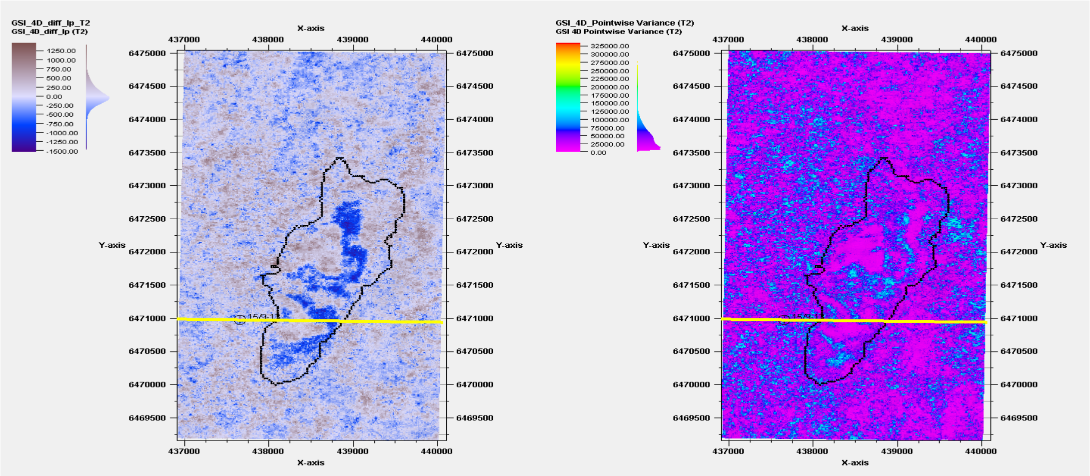

(e) Ip Base minus Ip Monitor 2004 GSI 4D

(f) Point-wise Variance

Figure 4.18: Processing GSI 4D 2004 Results L5

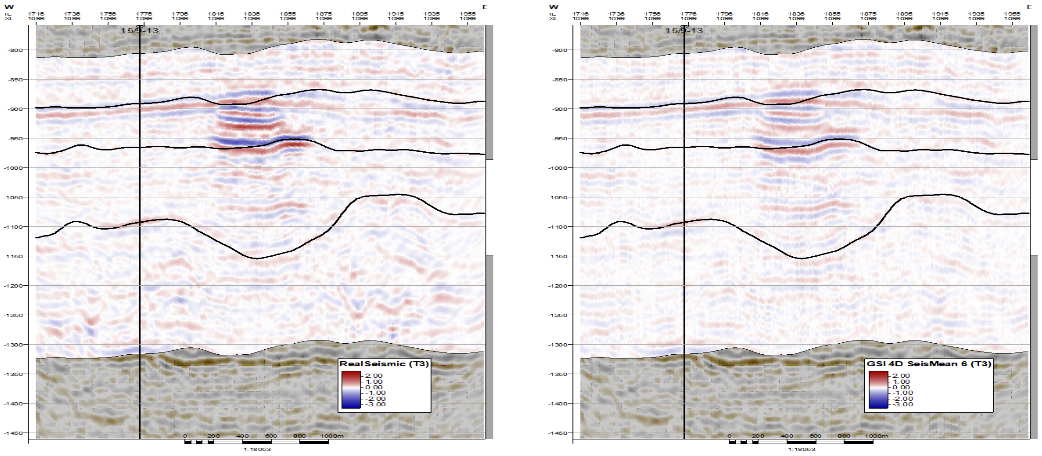

(a) Real Seismic 2006

(b) Synthetic Seismic 2006 GSI 4D

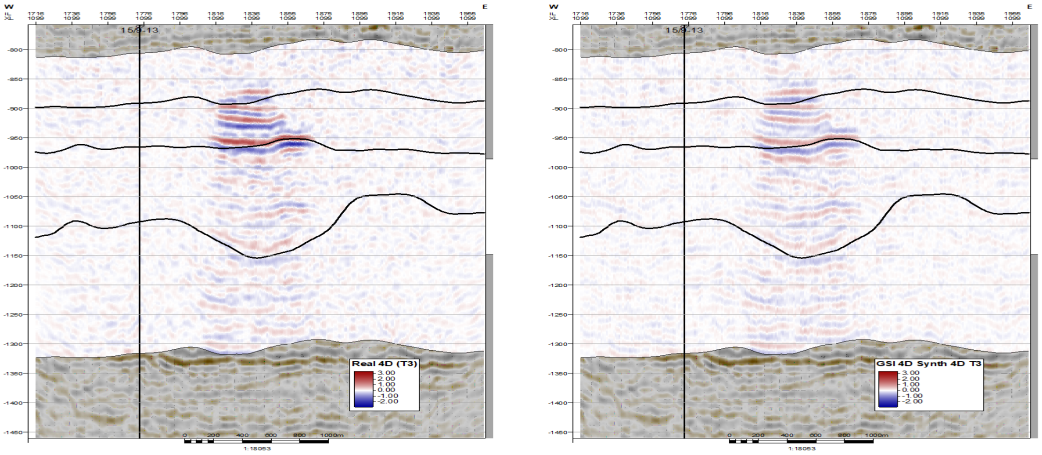

(c) Real Seismic Base minus Real Seismic Monitor

(d) Real Seismic Base minus Synthetic Seismic Monitor 2006 GSI 4D

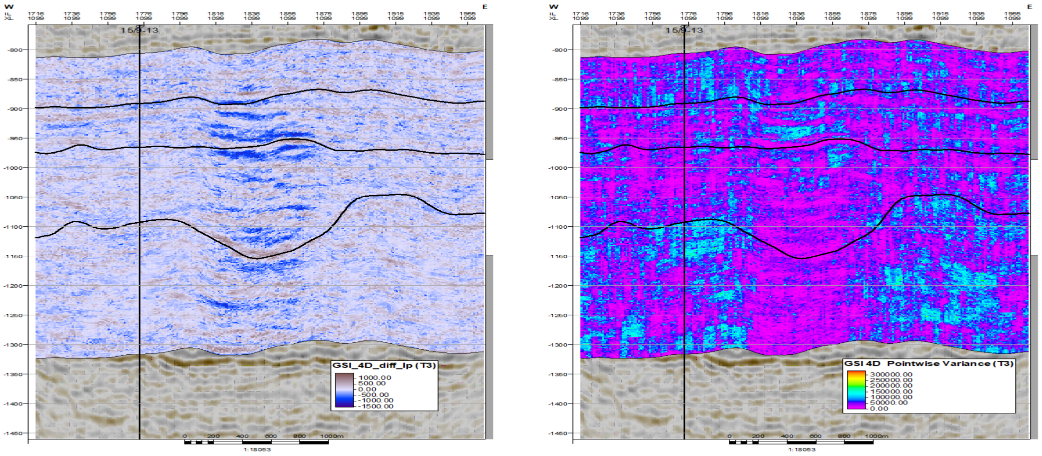

(e) Ip Base minus Ip Monitor 2006 GSI 4D

(f) Point-wise Variance

Figure 4.19: Processing GSI 4D 2006 Results

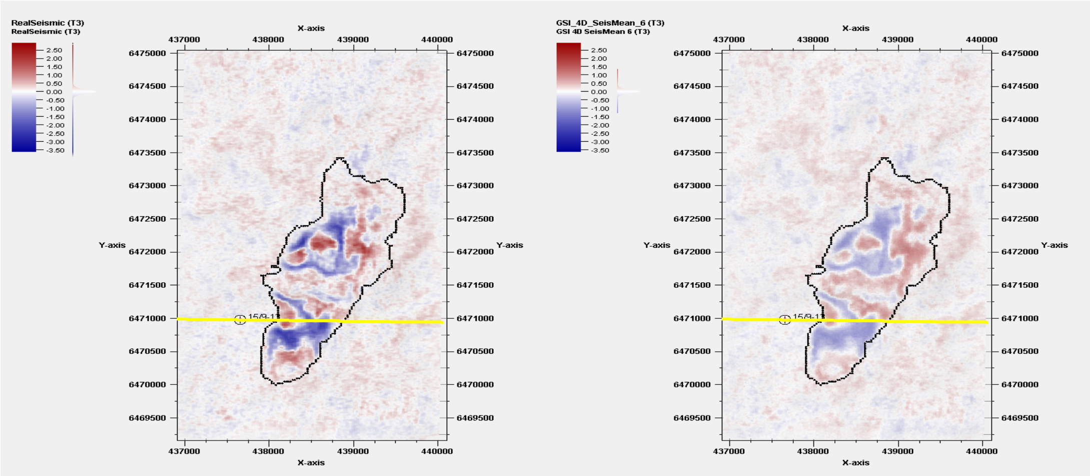

(a) Real Seismic 2006 **(b)** Synthetic Seismic 2006 GSI 4D

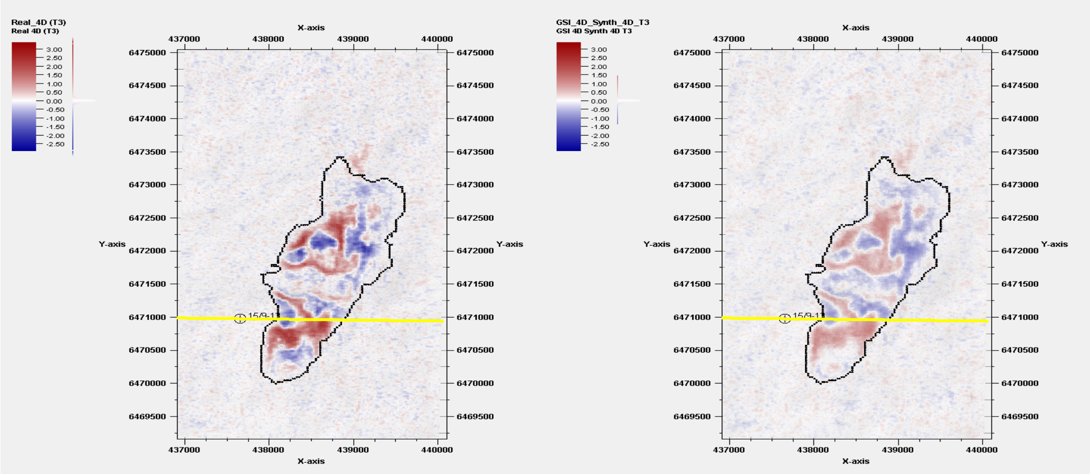

(c) Real Seismic Base minus Real Seismic Monitor **(d)** Real Seismic Base minus Synthetic Seismic Monitor 2006 GSI 4D

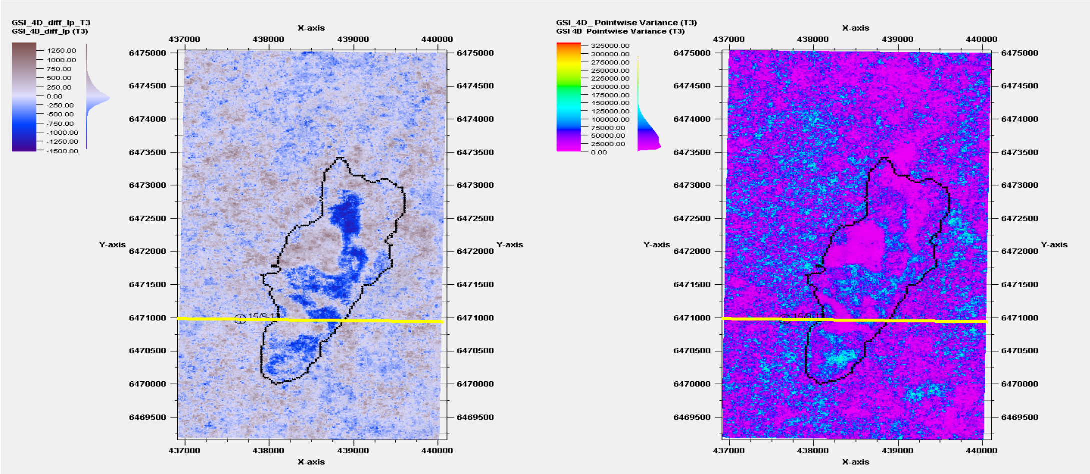

(e) Ip Base minus Ip Monitor 2006 GSI 4D **(f)** Point-wise Variance

Figure 4.20: Processing GSI 4D 2006 Results L5

4.3 GSI versus GSI 4D

In this section, we compare the results from GSI and GSI 4D, we look at the Ip results, base Ip minus monitor Ip as well as the point-wise variance of both methods to critically assess the results and present observations.

In order to have a consistent evaluation and assessment of the results, we processed the GSI results similar to the processing of the GSI 4D results. It can be seen in figures 4.21 and 4.22; the results from 2001 showing the real seismic compared with GSI synthetic seismic, the observed, ie. real 4D difference subtracting real base minus real monitor, and the predicted 4D difference, real base minus synthetic monitor, and show the Ip base subtracted from the Ip monitor along with the point-wise variance, with a view from the south and top view of base shale layer L5 respectively.

It can be seen in figures 4.23 and 4.24; the results from 2004 showing the real seismic compared with GSI synthetic seismic, the observed, ie. real 4D difference subtracting real base minus real monitor, and the predicted 4D difference, real base minus synthetic monitor, and show the Ip base subtracted from the Ip monitor along with the point-wise variance, with a view from the south and top view of base shale layer L5 respectively.

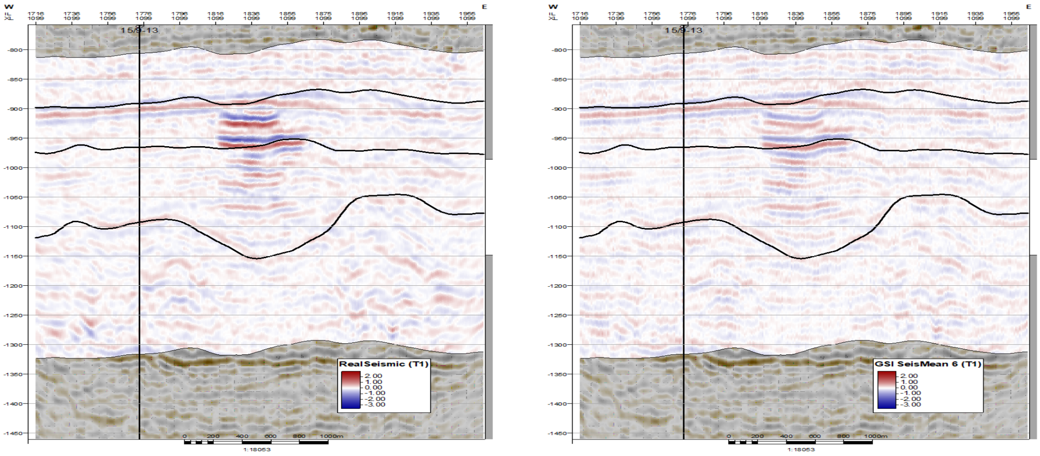

(a) Real Seismic 2001 **(b)** Synthetic Seismic 2001 GSI

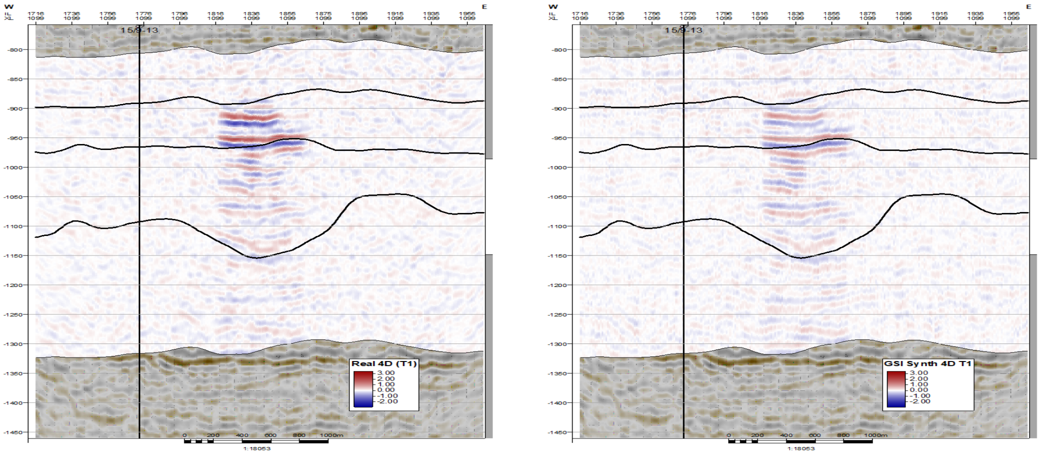

(c) Real Seismic Base minus Real Seismic Monitor 2001 **(d)** Real Seismic Base minus Synthetic Seismic Monitor 2001 GSI

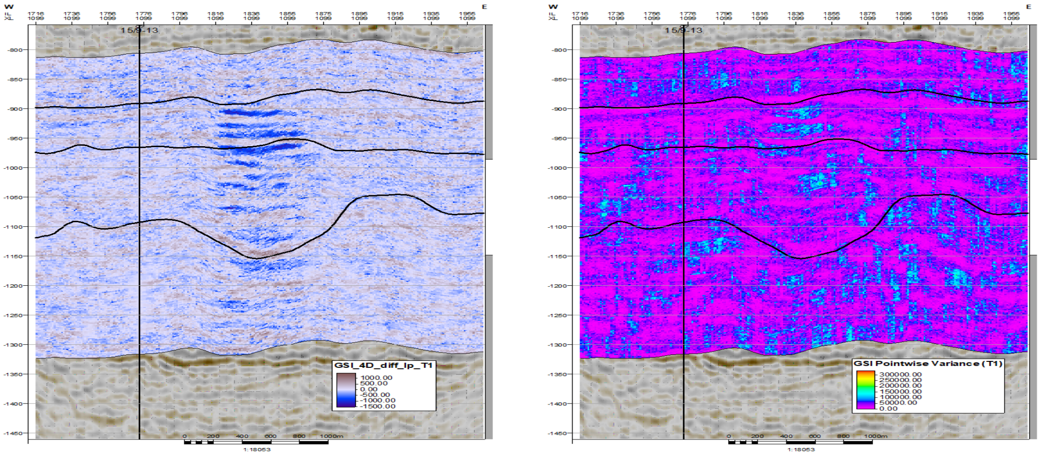

(e) Ip Base minus Ip Monitor 2001 GSI **(f)** Point-wise Variance

Figure 4.21: Processing GSI 2001 Results

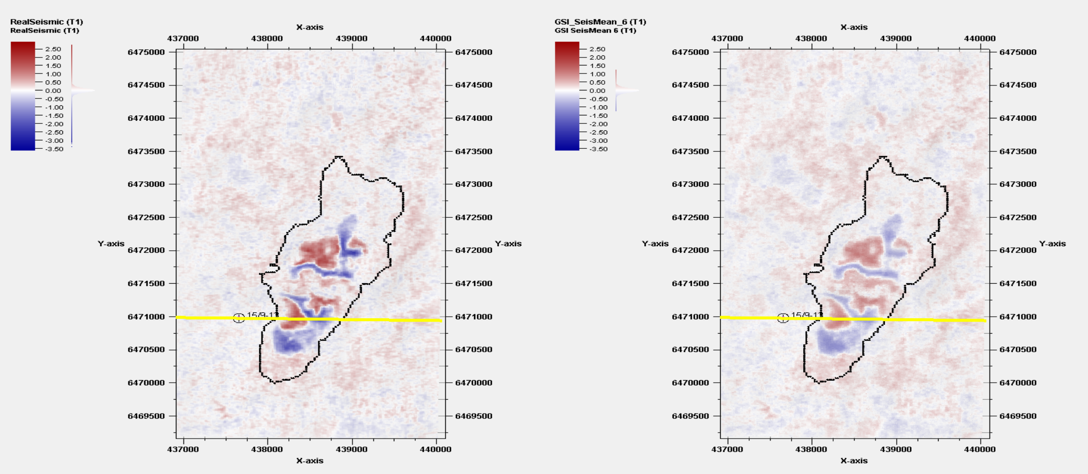

(a) Real Seismic 2001

(b) Synthetic Seismic 2001 GSI

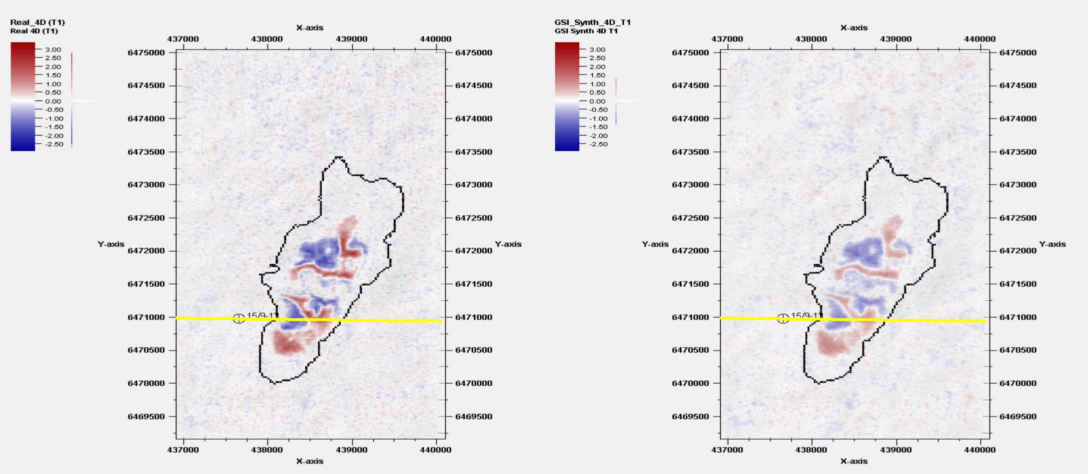

(c) Real Seismic Base minus Real Seismic Monitor

(d) Real Seismic Base minus Synthetic Seismic Monitor 2001 GSI

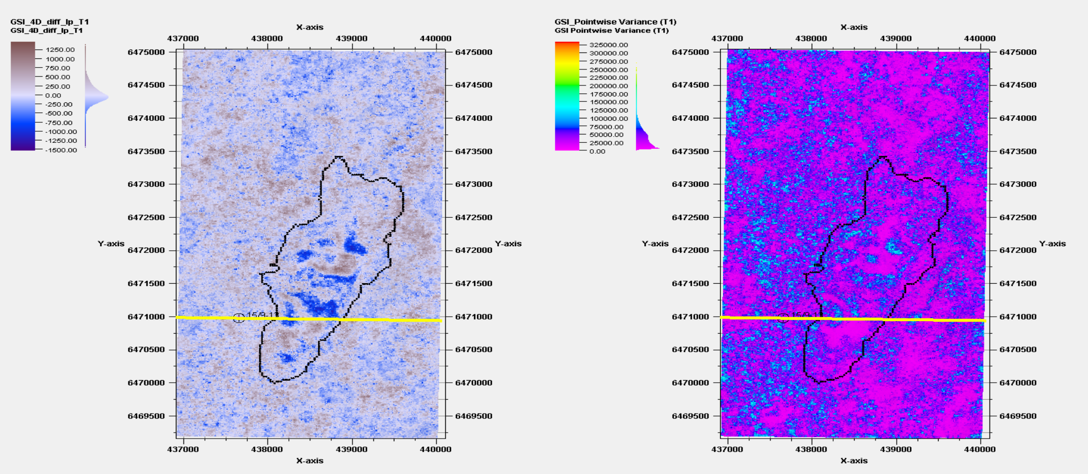

(e) Ip Base minus Ip Monitor 2001 GSI

(f) Point-wise Variance

Figure 4.22: Processing GSI 2001 L5 Results

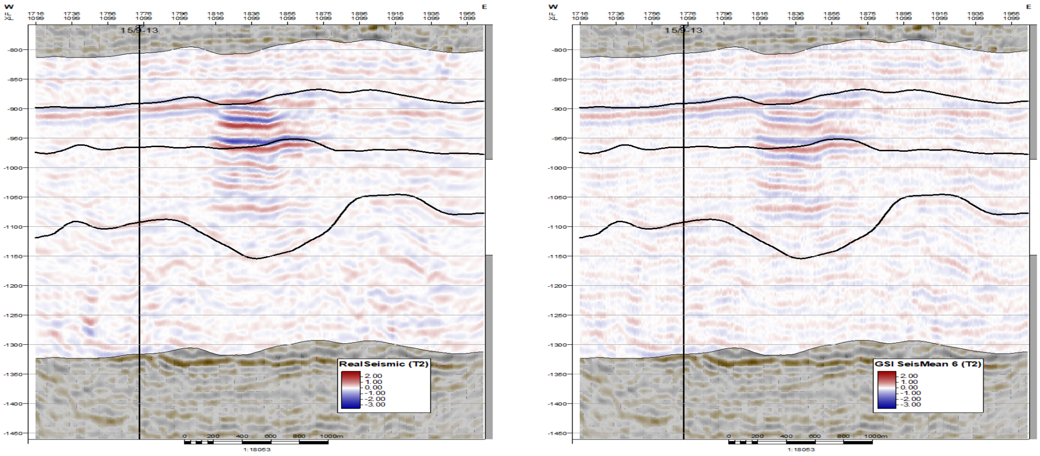

(a) Real Seismic 2004

(b) Synthetic Seismic 2004 GSI

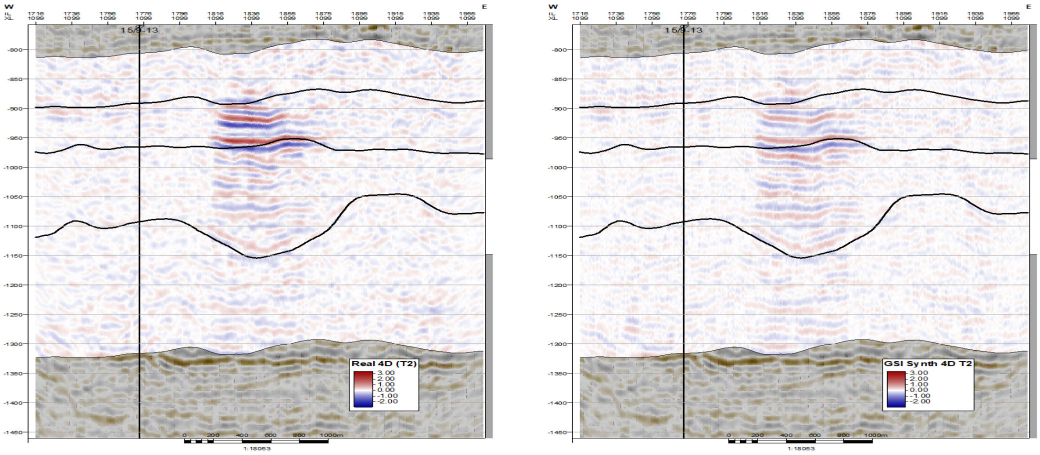

(c) Real Seismic Base minus Real Seismic Monitor 2004 GSI

(d) Real Seismic Base minus Synthetic Seismic Monitor 2004 GSI

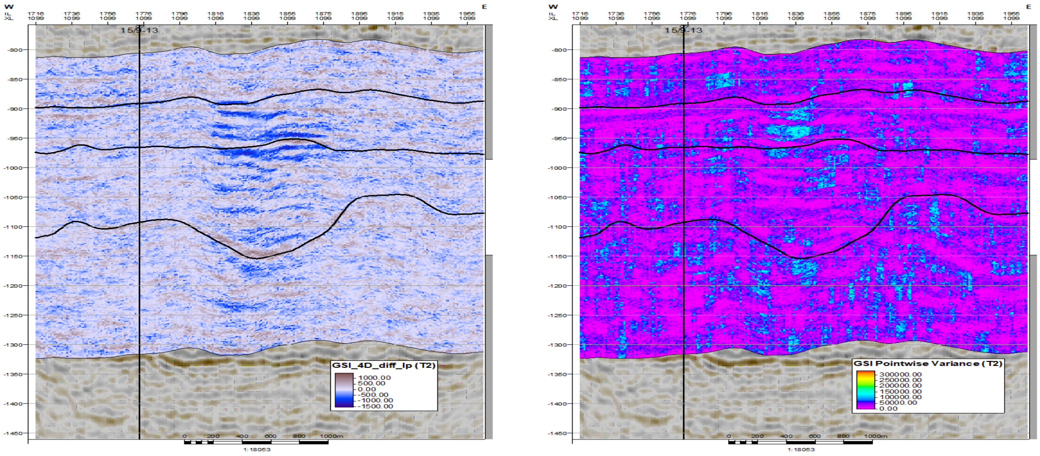

(e) Ip Base minus Ip Monitor 2004 GSI

(f) Point-wise Variance 2004 GSI

Figure 4.23: Processing GSI 2004 Results

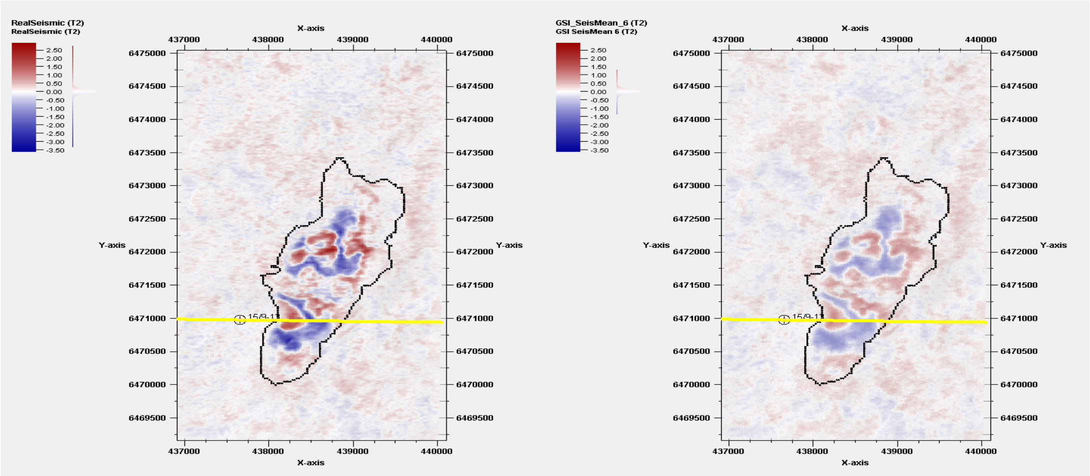

(a) Real Seismic 2004

(b) Synthetic Seismic 2004 GSI

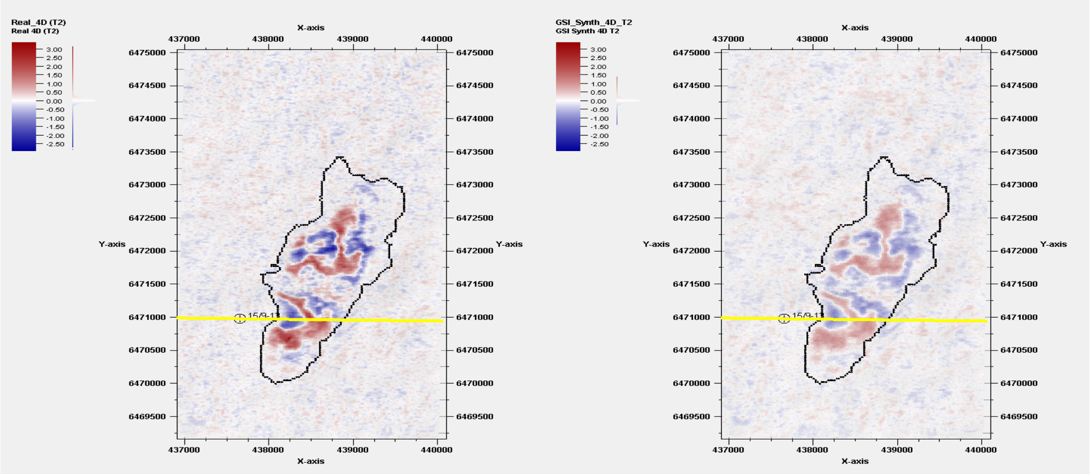

(c) Real Seismic Base minus Real Seismic Monitor 2004 GSI

(d) Real Seismic Base minus Synthetic Seismic Monitor 2004 GSI

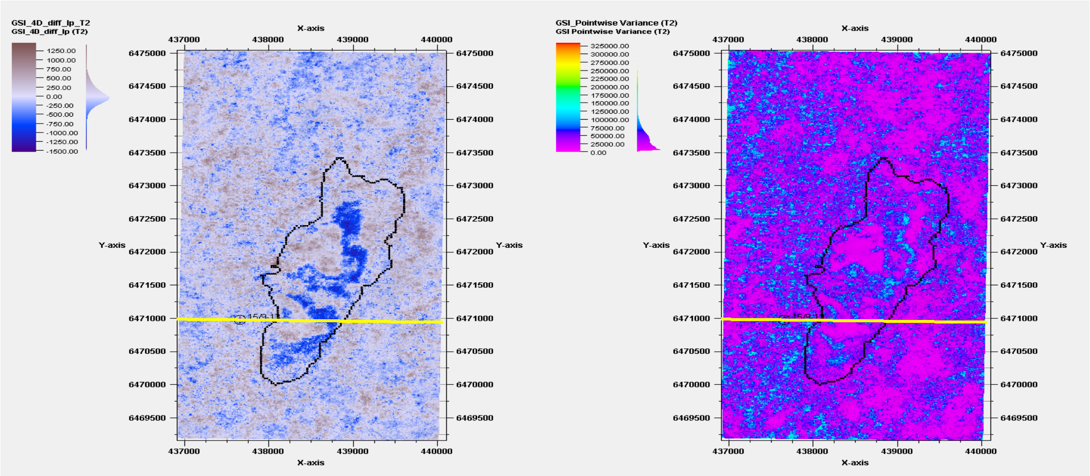

(e) Ip Base minus Ip Monitor 2004 GSI

(f) Point-wise Variance 2004 GSI

Figure 4.24: Processing GSI 2004 Results L5

It can be seen in figures 4.25 and 4.26; the results from 2006 showing the real seismic compared with GSI synthetic seismic, the observed, ie. real 4D difference subtracting real base minus real monitor, and the predicted 4D difference, real base minus synthetic monitor, and show the Ip base subtracted from the Ip monitor along with the point-wise variance, with a view from the south and top view of base shale layer L5 respectively.

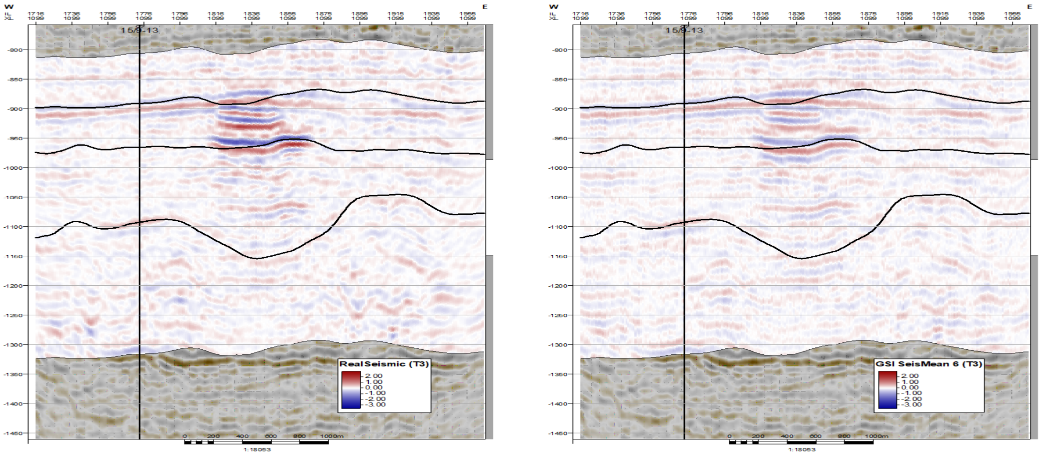

(a) Real Seismic 2006

(b) Synthetic Seismic 2006 GSI

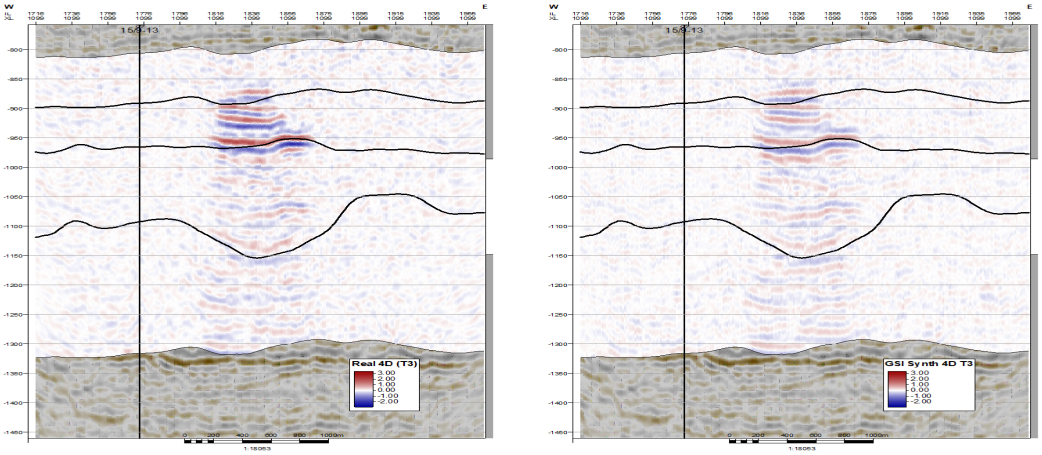

(c) Real Seismic Base minus Real Seismic Monitor

(d) Real Seismic Base minus Synthetic Seismic Monitor 2006 GSI

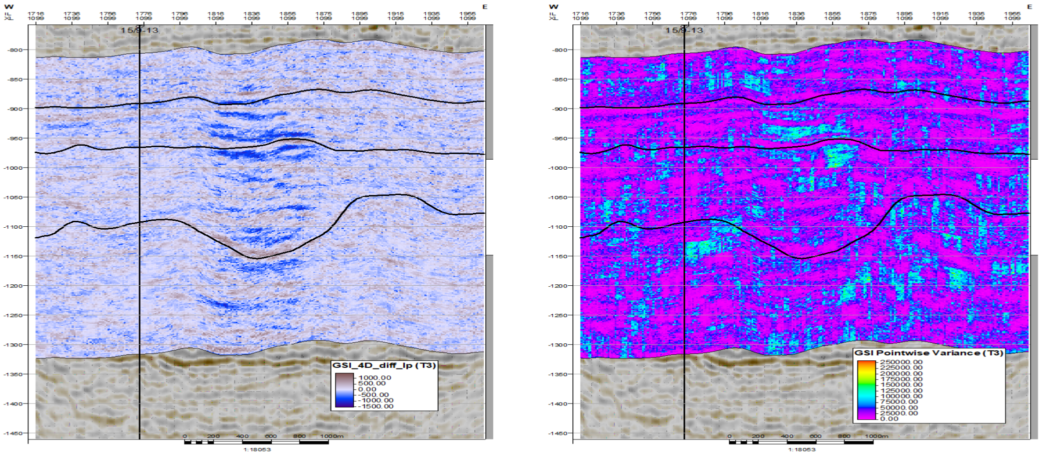

(e) Ip Base minus Ip Monitor 2006 GSI

(f) Point-wise Variance 2006 GSI

Figure 4.25: Processing GSI 2006 Results

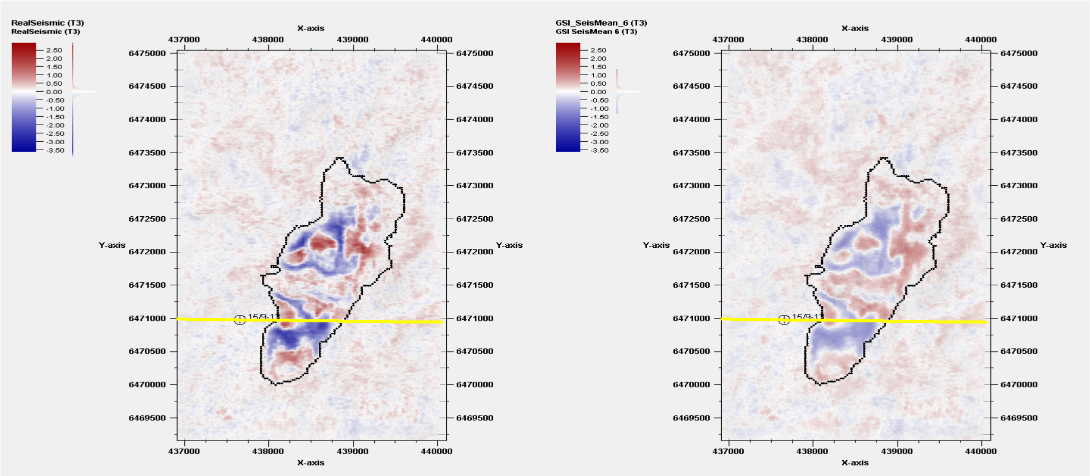

(a) Real Seismic 2006 **(b)** Synthetic Seismic 2006 GSI

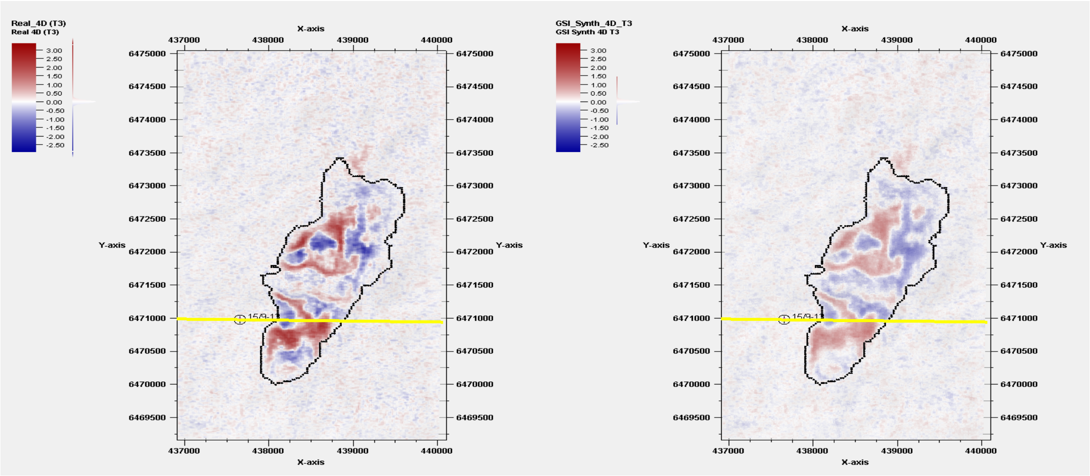

(c) Real Seismic Base minus Real Seismic Monitor **(d)** Real Seismic Base minus Synthetic Seismic Monitor 2006 GSI

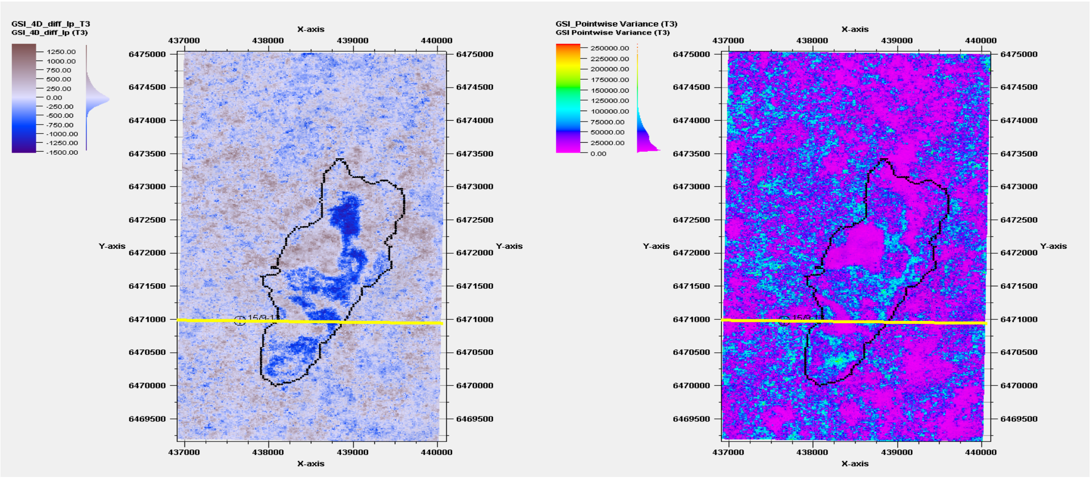

(e) Ip Base minus Ip Monitor 2006 GSI **(f)** Point-wise Variance 2006 GSI

Figure 4.26: Processing GSI 2006 Results L5

4.3.1 Discussion

Figures 4.27 and 4.28 show the results from GSI and GSI 4D, we look at the Ip results, base Ip minus monitor Ip as well as the point-wise variance from the 2001 dataset; while figures 4.29 and 4.30 show the results from GSI and GSI 4D, we look at the Ip results, base Ip minus monitor Ip as well as the point-wise variance from the 2004 dataset; and figures 4.31 and 4.32 show the results from GSI and GSI 4D, we look at the Ip results, base Ip minus monitor Ip as well as the point-wise variance from the 2006 dataset

It can be seen from figure 4.27 we see that the Ip results and base Ip minus monitor Ip as well, are almost identical except for some fuzziness at the base and flanks of the plume Ip due to the convergence being driven by 4D signals rather than the classic seismic driven convergence, we can also notice the distinctions in the variance results. Figure 4.28 shows top view of the results, where we found the difference of Ip is almost identical spatially but with slightly different amplitude intensity, which is probably due to the fact that we based our variograms on the seismic data to mitigate the lack of wells in the area; the Ip and variance results depicting the essence of our methodology and are the corner point of this thesis, depicting distinct differences GSI Ip 4D has a better characterization of the plume's boundary as well as internal architecture. It is worth noting that the GSI 4D captures the area outside the plume fairly good, not as well as the classic GSI, this is due to the fact that our methodology is driven by the 4D signal convergence and that implies a high noise content outside of the plume increases the local variance; this is where the algorithm will give less influence on higher variance regions and populating them with the mean values, which in our case is the base seismic data. Figures 4.29 to 4.32, show the same results from 2004 through 2006, which cement these observations even further. In the appendix A attached are the remaining visuals from the thesis for further analysis and review by the reader.

In all the results we can see stability of the base of the utsira formation from the diffrences results, Ip and seismic, which indicate that the performance of our methods was able to correctly position the 4D signals in the correct location which can be seen with the comparison of the signal at the base of formation. It is worth mentioning the the inverion reults from individaul time steps clearly show the pushdown effects before the subtraction with base. Our results have achived the objective of the thesis to link the different seismic survies in the temporal domain.

The key takeaway is that the differences in variance show the core strength of both algorithms. The classic GSI is able to capture distinct point breaks in the seismic amplitude, which can be a good indicator for the migration pathway of the CO2 in the subsurface while the GSI 4D is capturing the CO2 plume and the illuminated subseismic resolution shales excellently, which is demonstrated with almost zero variance inside the plume when compared to the classic GSI.

Our method shows great promise, as it is based on the fundamentals of the Global Stochastic Inversion [62], to be extended to Global Elastic Inversion and 4D Geo-mechanical Earth Modeling both of which are crucial to the next steps in the Energy Transition and Carbon Neutrality global efforts.

The stregnth of our propsed method is the ability to use the seismic directly, the probabilistic framework aids in the uncertainty assessment due to the difference in the resolution between well seismic data, and that it can be extended for elastic inversion.

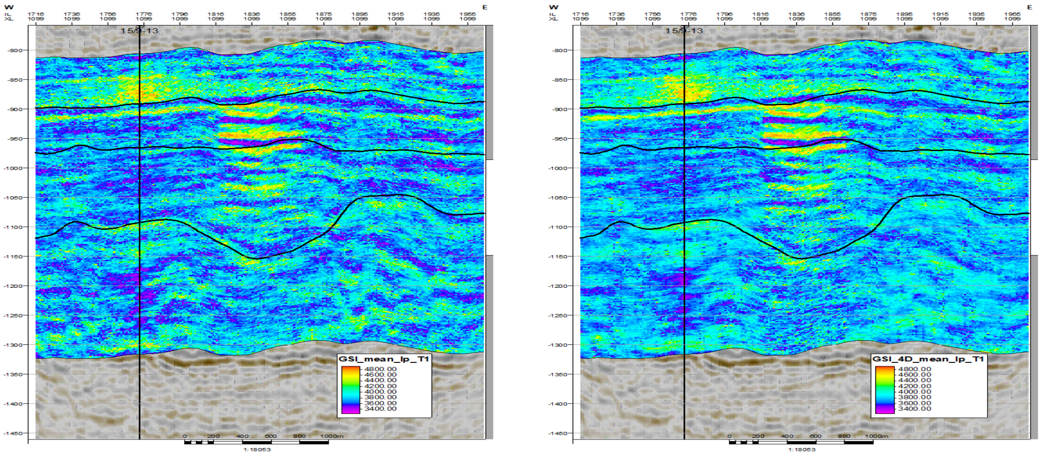

(a) Ip 2001 GSI **(b)** Ip 2001 GSI 4D

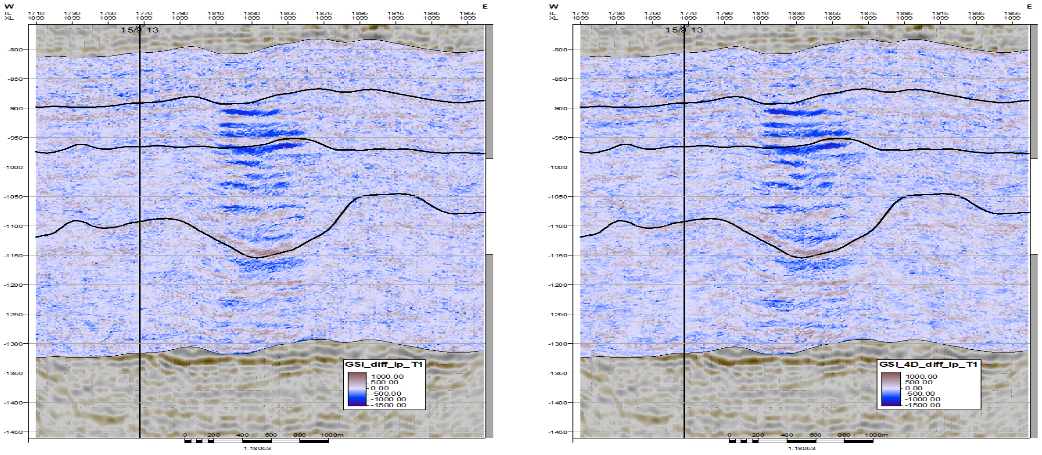

(c) Ip Base Minus Ip Monitors 2001 GSI **(d)** Ip Base Minus Ip Monitors 2001 GSI 4D

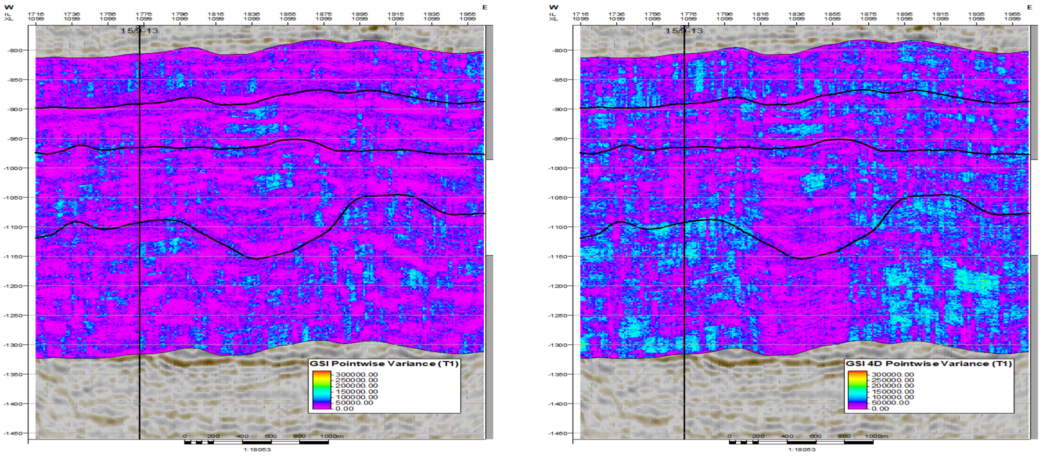

(e) Point-wise Variance 2001 GSI **(f)** Point-wise Variance 2001 GSI 4D

Figure 4.27: Model Domain 2001

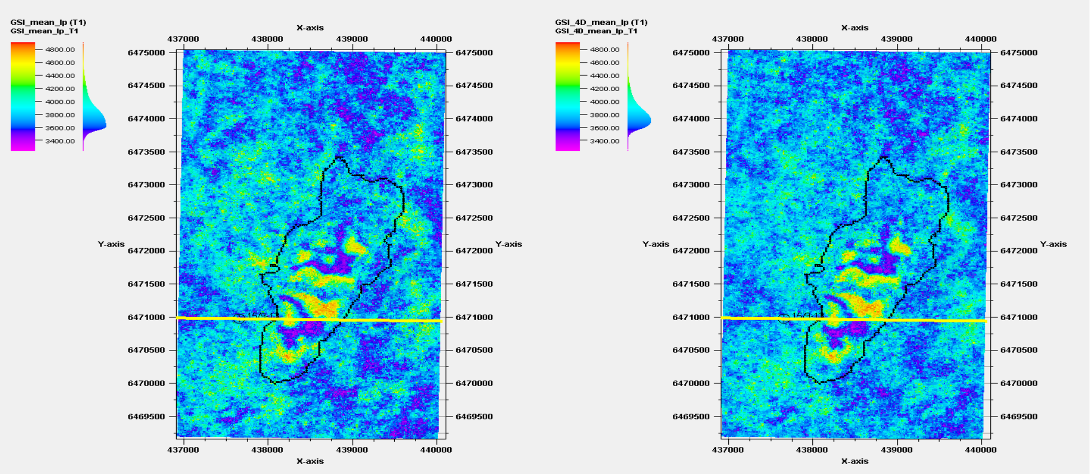

(a) Ip 2001 GSI

(b) Ip 2001 GSI 4D

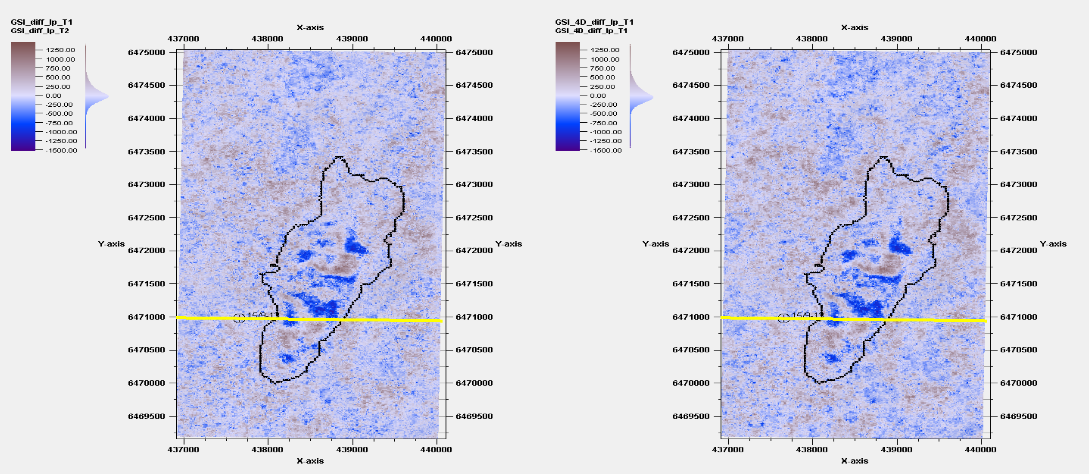

(c) Ip Base Minus Ip Monitors 2001 GSI

(d) Ip Base Minus Ip Monitors 2001 GSI 4D

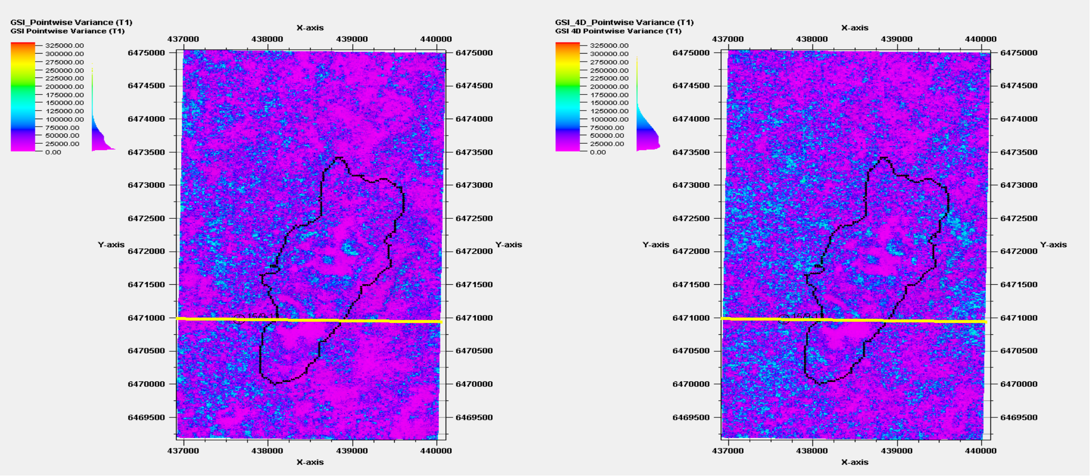

(e) Point-wise Variance 2001 GSI

(f) Point-wise Variance 2001 GSI 4D

Figure 4.28: Model Domain 2001 L5

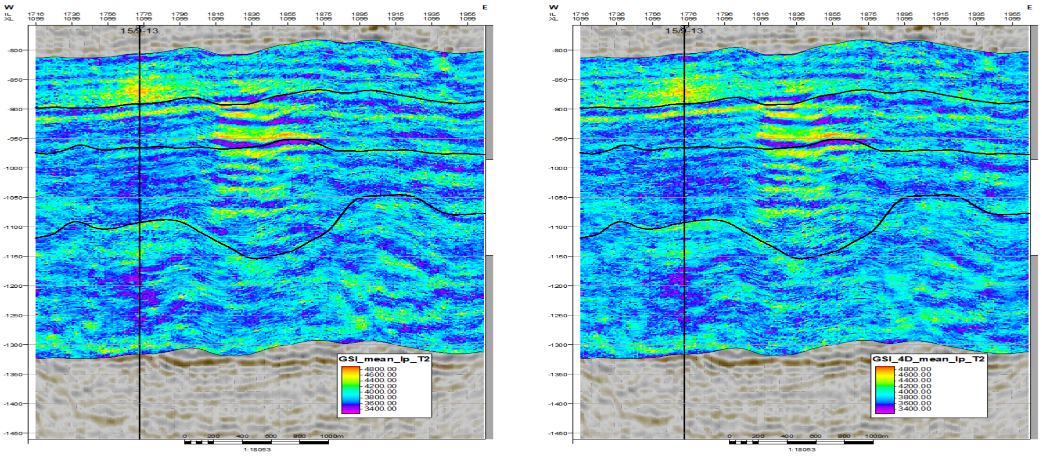

(a) Ip 2004 GSI

(b) Ip 2004 GSI 4D

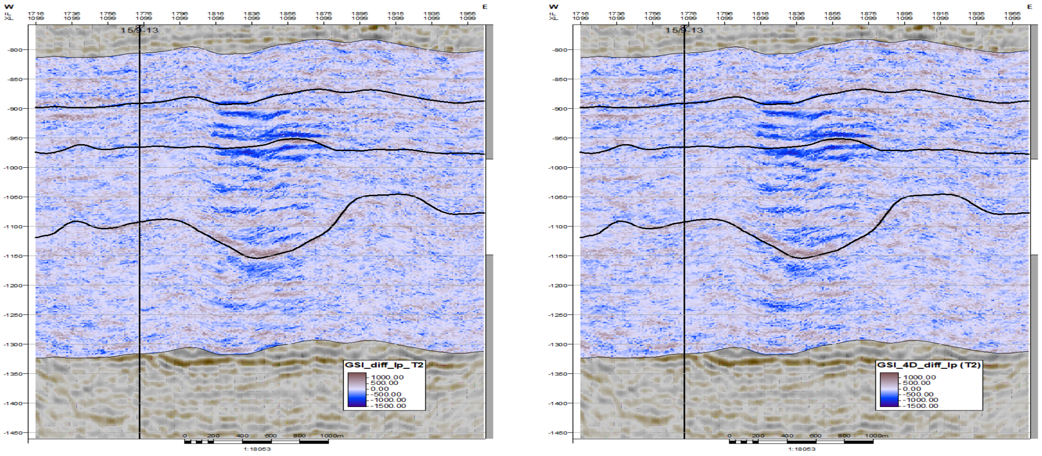

(c) Ip Base Minus Ip Monitors 2004 GSI

(d) Ip Base Minus Ip Monitors 2004 GSI 4D

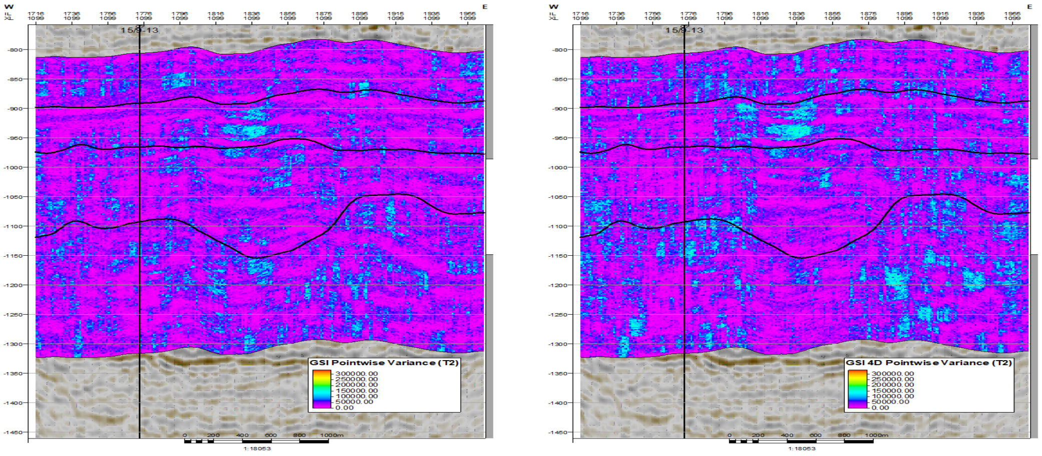

(e) Point-wise Variance 2004 GSI

(f) Point-wise Variance 2004 GSI 4D

Figure 4.29: Model Domain 2004

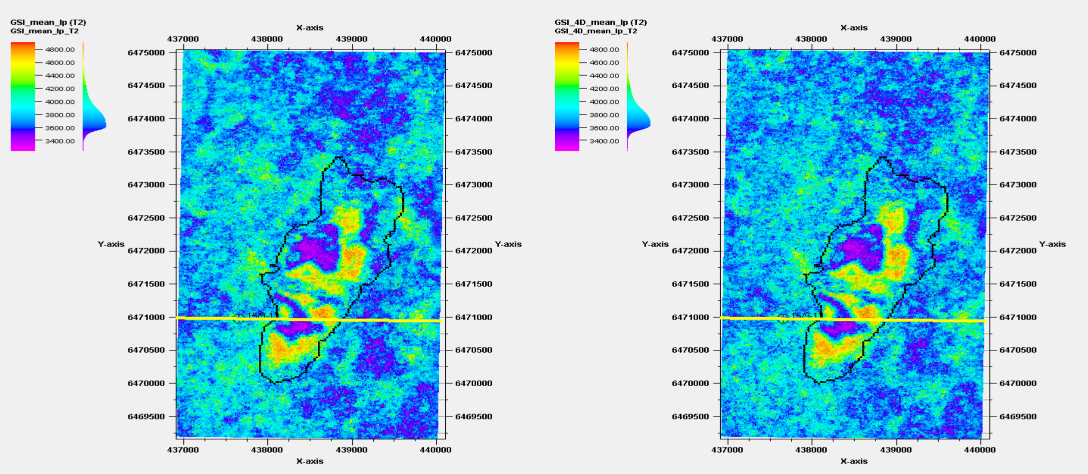

(a) Ip 2004 GSI

(b) Ip 2004 GSI 4D

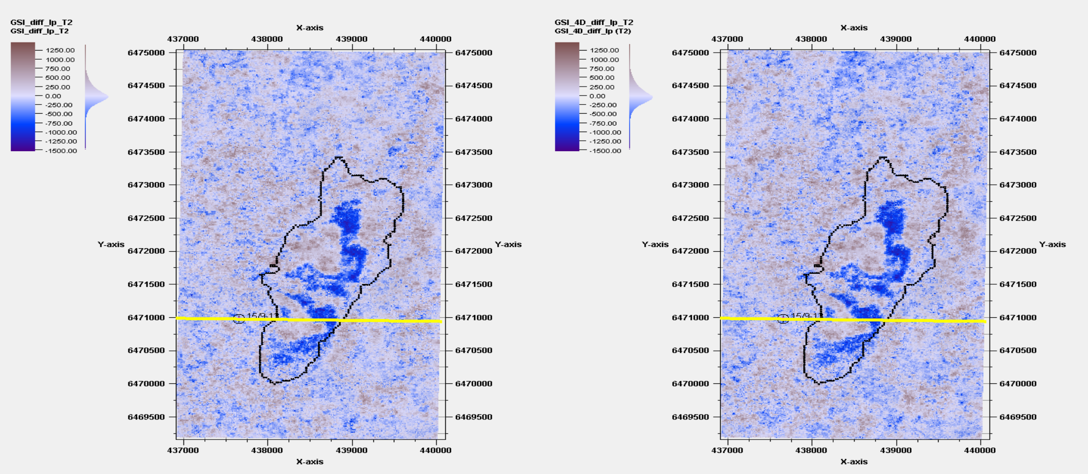

(c) Ip Base Minus Ip Monitors 2004 GSI

(d) Ip Base Minus Ip Monitors 2004 GSI 4D

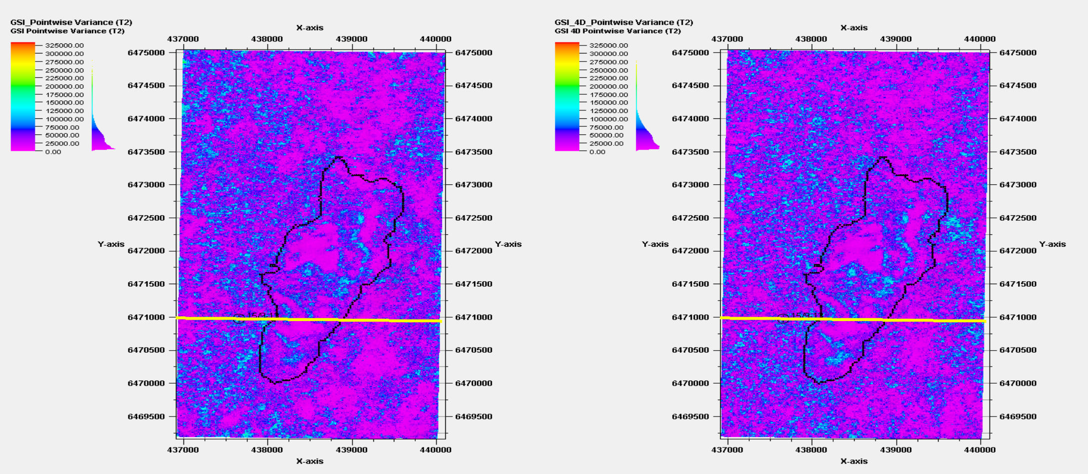

(e) Point-wise Variance 2004 GSI

(f) Point-wise Variance 2004 GSI 4D

Figure 4.30: Model Domain 2004 L5

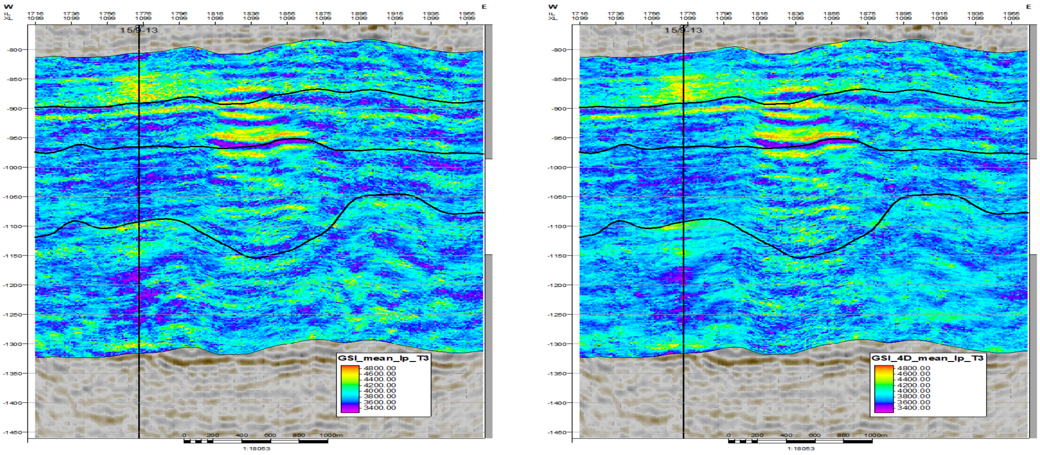

(a) Ip 2006 GSI

(b) Ip 2006 GSI 4D

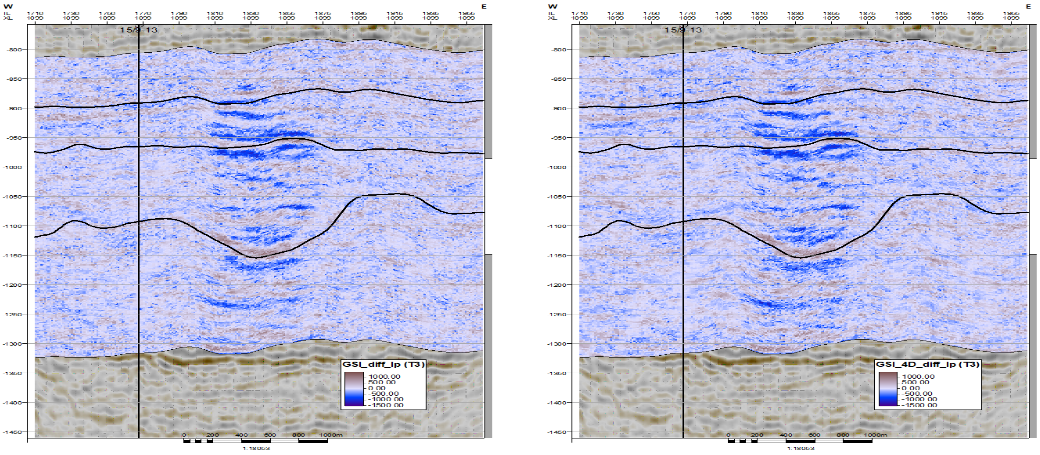

(c) Ip Base Minus Ip Monitors 2006 GSI

(d) Ip Base Minus Ip Monitors 2006 GSI 4D

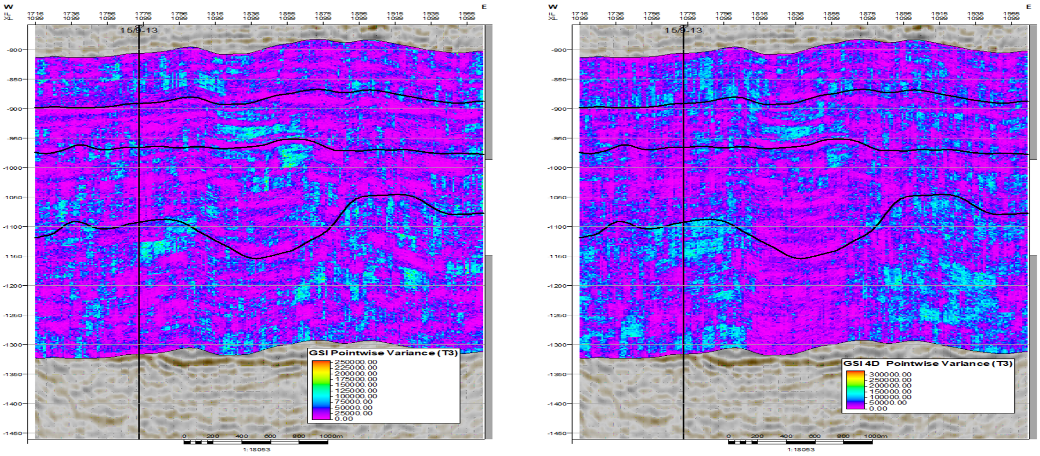

(e) Point-wise Variance 2006 GSI

(f) Point-wise Variance 2006 GSI 4D

Figure 4.31: Model Domain 2006

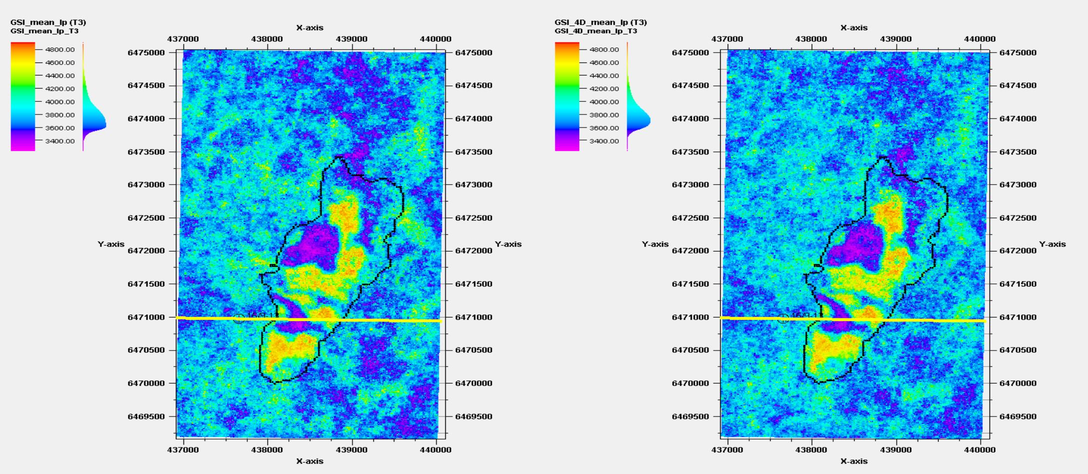

(a) Ip 2006 GSI **(b)** Ip 2006 GSI 4D

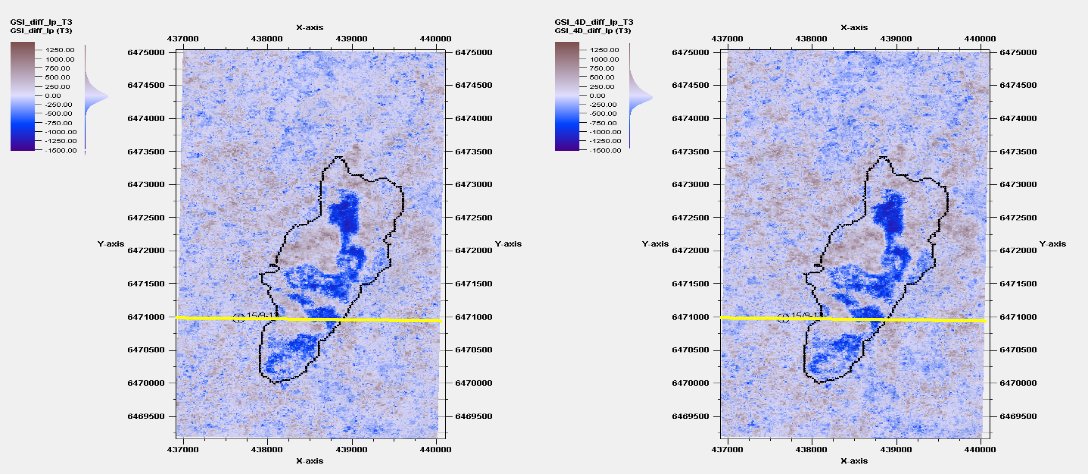

(c) Ip Base Minus Ip Monitors 2006 GSI **(d)** Ip Base Minus Ip Monitors 2006 GSI 4D

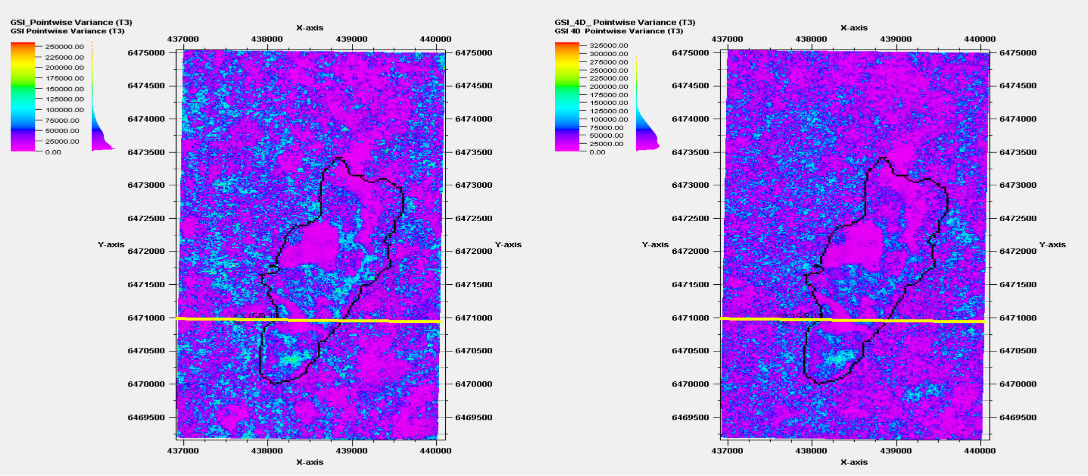

(e) Point-wise Variance 2006 GSI **(f)** Point-wise Variance 2006 GSI 4D

Figure 4.32: Model Domain 2006 L5

Figures 4.33 and A.19 show real seismic compared to synthetic seismic from both methods and real seismic base minus real seismic monitor compared with the real seismic base minus synthetic motor of each method from the 2001 dataset; while figures 4.34 and A.20 show real seismic compared to synthetic seismic from both methods and real seismic base minus real seismic monitor compared with real seismic base minus synthetic motor of each method from the 2004 dataset; and figures 4.35 and A.21 show real seismic compared to synthetic seismic from both methods and real seismic base minus real seismic monitor compared with the real seismic base minus synthetic motor of each method from the 2006 dataset.

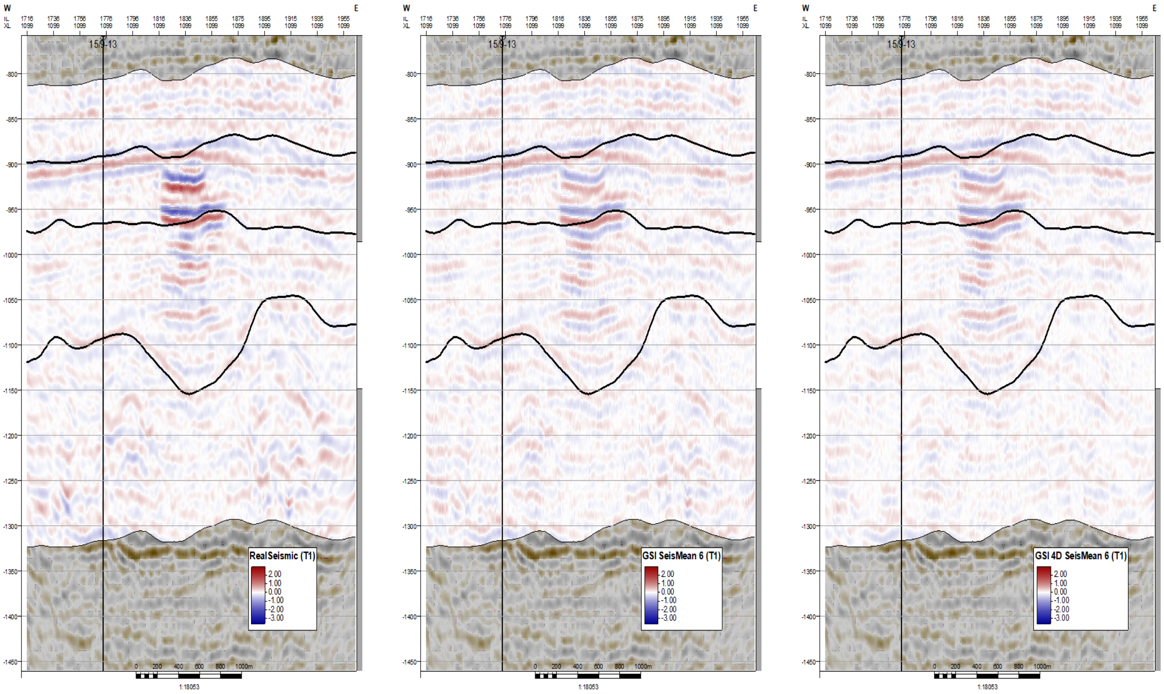

(a) Real Seismic 2001 **(b)** Synthetic Seismic 2001 GSI **(c)** Synthetic Seismic 2001 GSI 4D

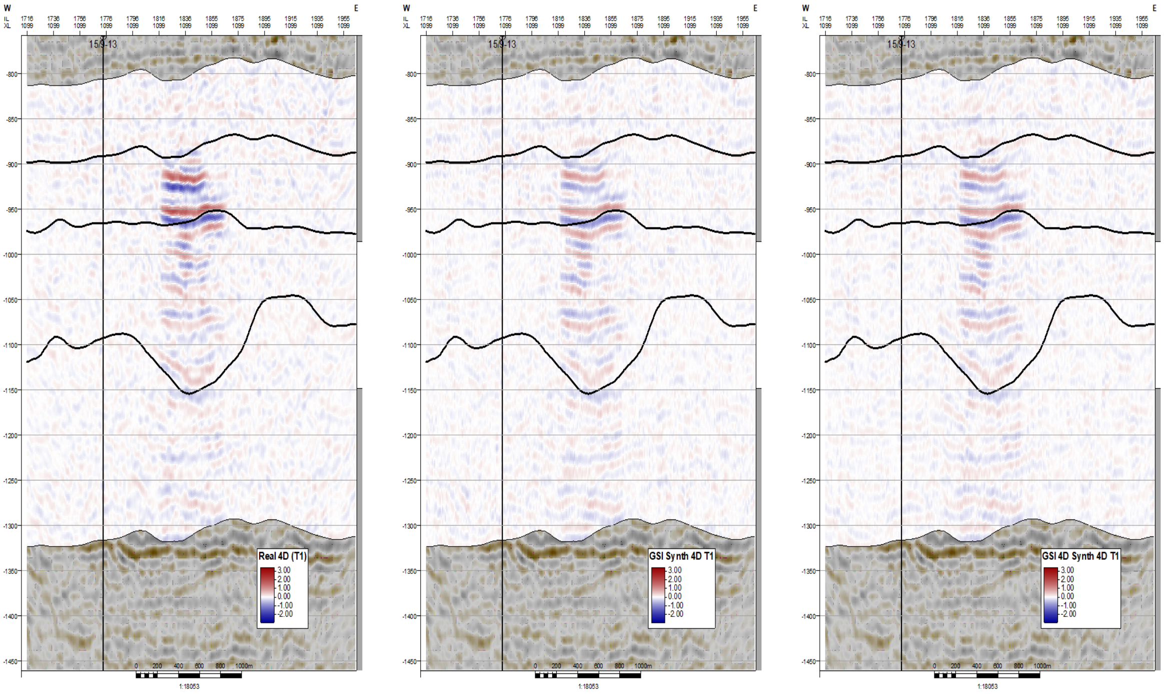

(d) Real Seismic Base Minus Real Seismic Monitors 2001 **(e)** Real Seismic Base Minus Synthetic Seismic Monitors 2001 GSI **(f)** Real Seismic Base Minus Synthetic Seismic Monitors 2001 GSI 4D

Figure 4.33: Seismic Domain 2001

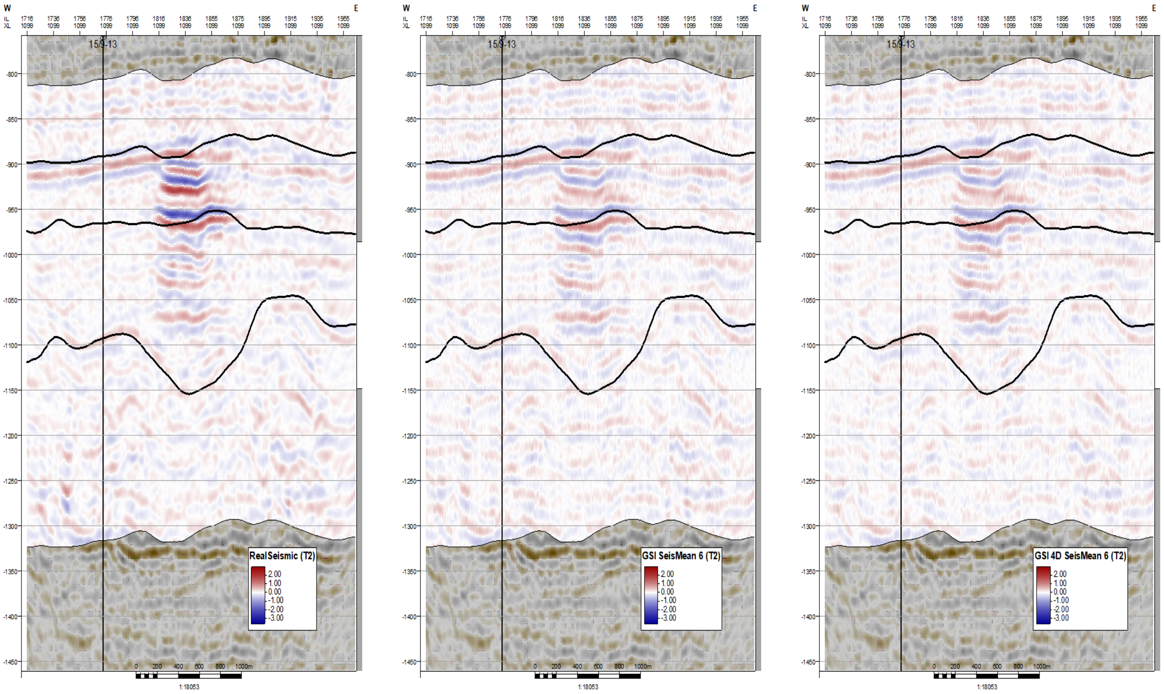

(a) Real Seismic 2004

(b) Synthetic Seismic 2004 GSI

(c) Synthetic Seismic 2004 GSI 4D

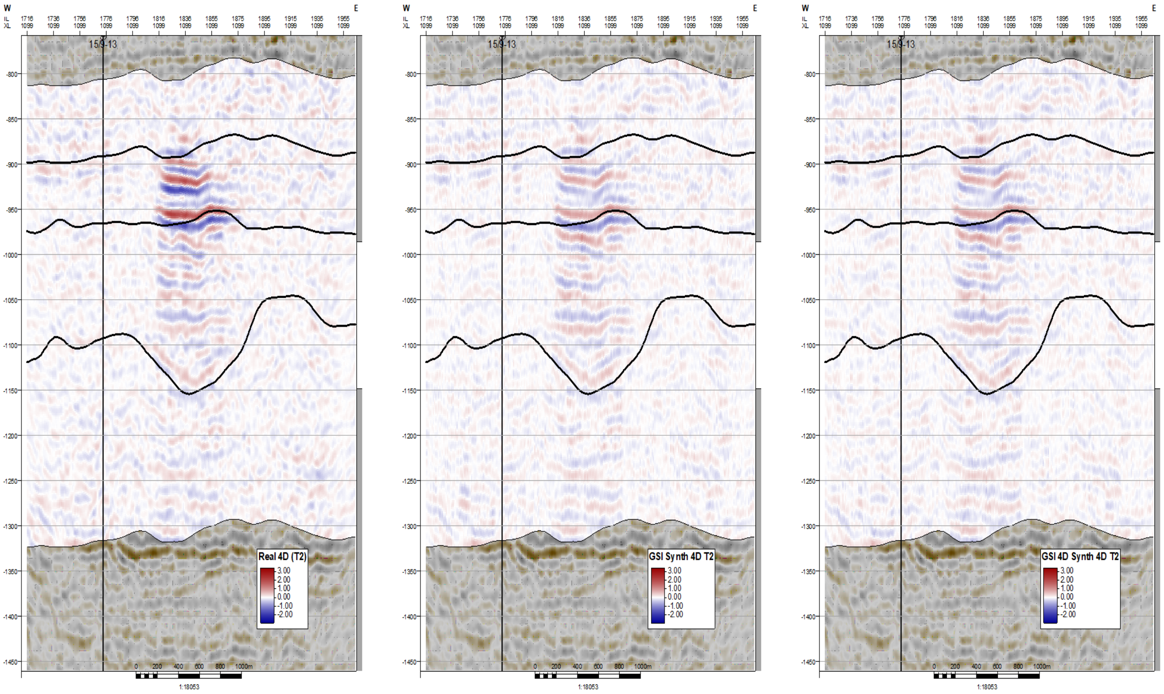

(d) Real Seismic Base Minus Real Seismic Monitors 2004

(e) Real Seismic Base Minus Synthetic Seismic Monitors 2004 GSI

(f) Real Seismic Base Minus Synthetic Seismic Monitors 2004 GSI 4D

Figure 4.34: Seismic Domain 2004

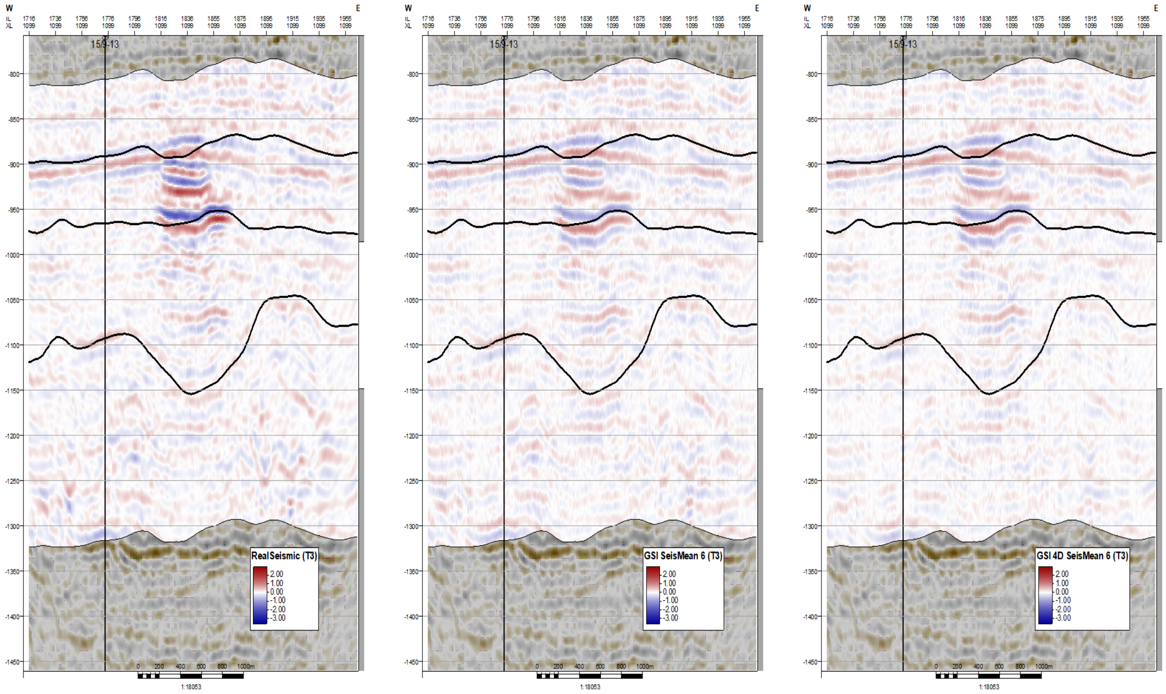

(a) Real Seismic 2006 **(b)** Synthetic Seismic 2006 GSI **(c)** Synthetic Seismic 2006 GSI 4D

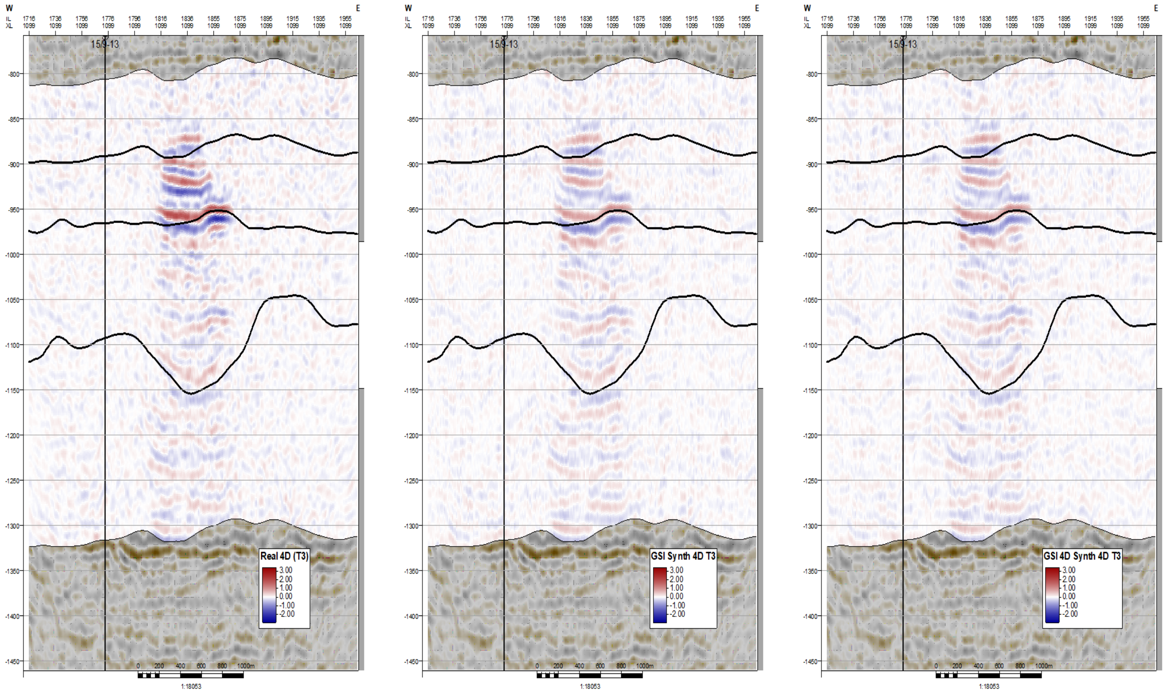

(d) Real Seismic Base Minus Real Seismic Monitors 2006 **(e)** Real Seismic Base Minus Synthetic Seismic Monitors 2006 GSI **(f)** Real Seismic Base Minus Synthetic Seismic Monitors 2006 GSI 4D

Figure 4.35: Seismic Domain 2006

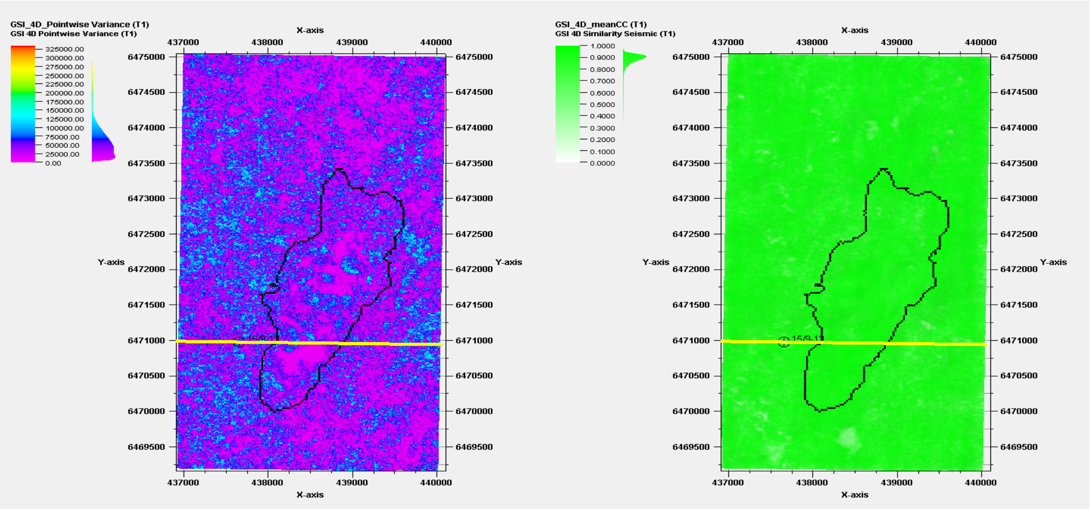

(a) Point-wise Variance 2001 acGSI 4D L5

(b) MeanCC 2001 GSI 4D L5

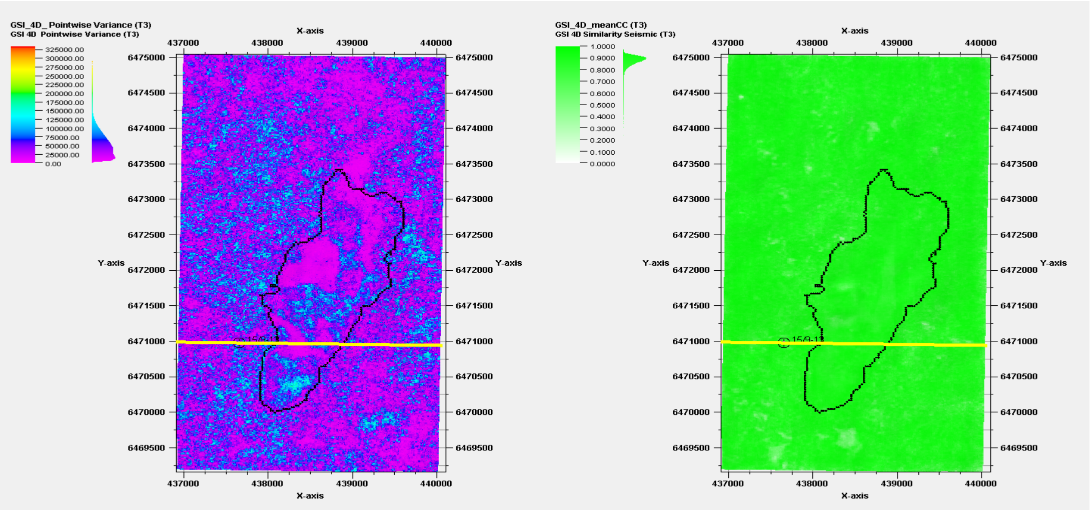

(c) Point-wise Variance 2006 GSI 4D L5

(d) MeanCC 2006 GSI 4D L5

Figure 4.36: MeanCC and Point-wise Variance GSI 4D L5

Finally, figuers fig. 4.36 and fig. 4.37 shows the point-wise variance and meanCC from the top view of layer 5 in year 2001 and 2006 utilizing GSI 4D and GSI, repectivly. The key takeaway is that the differences in variance show the core strength of both algorithms. The classic GSI is able to capture distinct point breaks in the seismic amplitude, which can be a good indicator for the migration pathway of the CO2 in the subsurface while the GSI 4D is capturing the CO2 plume and the illuminated subseismic resolution shales excellently, which is demonstrated with almost zero variance inside the plume when compared to the classic GSI.

Our method shows great promise, as it is based on the fundamentals of the Global Stochastic Inversion [62], to be extended to Global Elastic Inversion and 4D Geo-mechanical Earth Modeling both of which are crucial to the next steps in the Energy Transition and Carbon Neutrality global efforts.

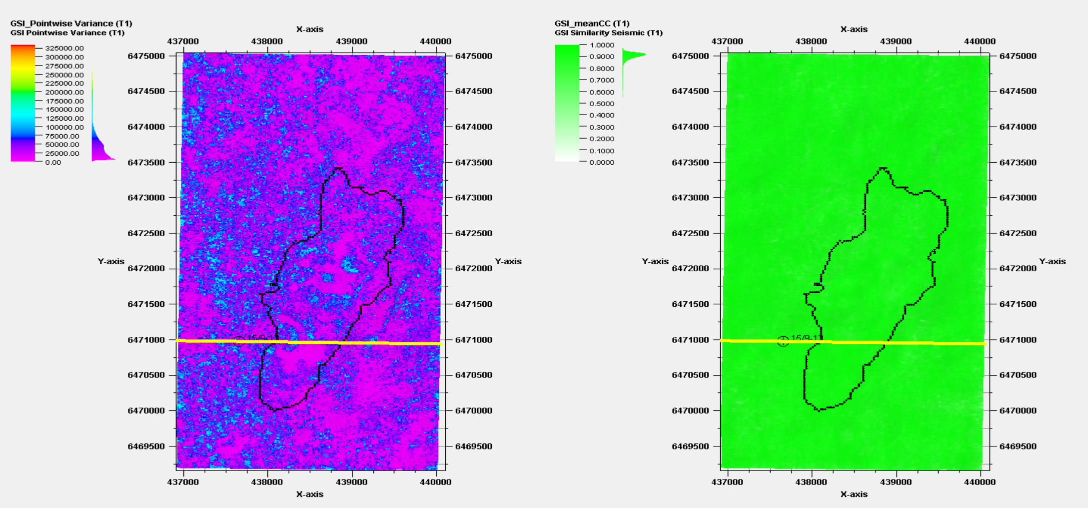

(a) Point-wise Variance 2001 GSI

(b) MeanCC 2001 GSI

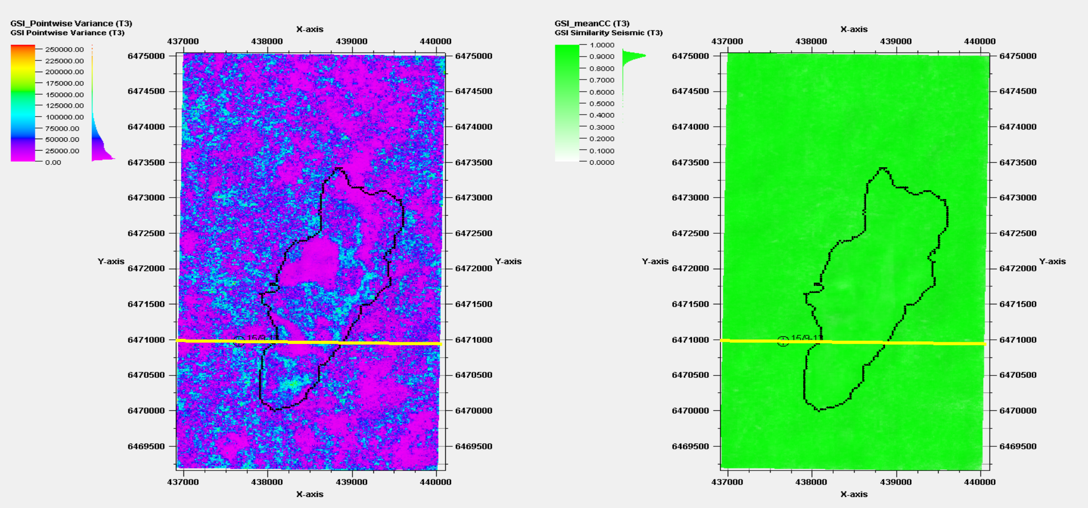

(c) Point-wise Variance 2006 GSI

(d) MeanCC 2006 GSI

Figure 4.37: MeanCC and Point-wise Variance GSI

5

Conclusions

In this thesis we have covered the relevant literature reviewing the fundamentals of the geophysical inverse problem, followed by a comparison between deterministic and probabilistic inversion methods with a focus on the state of the art and the direction of the seismic reservoir characterization and inversion research domain; finally, we highlighted the relevant Time-Lapse 4D interpretation methods.

In Chapter Three, we described the necessary steps to be applied before the implementation of our proposed methodology. First, we described Exploratory Data Analysis which deals with mining the data, analyzing, visualizing, and describing the data; then we walked through the procedures for creating the Geocellular model for the inversion and followed with the methodology implemented for the calculation of the experimental variogram as well as elaborating the spatial continuity revealing nested variogram models. After which we gave a brief description of the Geostatistical Seismic Inversion methodology implemented as a benchmark for our proposed iterative geostatistical inversion. Finally, we described the stages of our proposed algorithm, highlighted the novelty of our approach, and the objective function that drives the convergence of our inversion. Chapter four started with a description of the Sleipner data set utilized to demonstrate our proposed methodology, followed by an illustration of the results of the GSI algorithm to be implemented as a benchmark, and the results of our proposed methodology are discussed.

Future recommendations, other than the possible extension of the algorithm, should include the addition of more well controls in the area. Another area for possible improvements is the wavelet extraction, petrophysical analysis as well and detailed rock physics models. The Sleipner data set has never been used with our GSI methodologies, this presents an opportunity to use the benchmark GSI inversions to evaluate the changes in the reservoir properties such permeability enhancement or impairment due the injection of supercritical CO2 which is an excellent collaboration point with our colleges form geochemistry.

Another avenue for development woulb be to mix our methodology with the Bayesian framework [84] inverting for the ratio of Ip rather than inverting for 4D differences.

Bibliography

[1] I. Change, "2006 ipcc guidelines for national greenhouse gas inventories," *Institute for Global Environmental Strategies, Hayama, Kanagawa, Japan*, 2006.

[2] "IPCC Updates Methodology for Greenhouse Gas Inventories — IPCC." [Online]. Available: https://www.ipcc.ch/2019/05/13/ipcc-2019-refinement/

[3] I. Energy Agency, "Net Zero by 2050 - A Roadmap for the Global Energy Sector," 2050. [Online]. Available: www.iea.org/t&c/

[4] P. S. Ringrose, "The CCS hub in Norway: Some insights from 22 years of saline aquifer storage," *Energy Procedia*, vol. 146, pp. 166–172, 2018, publisher: Elsevier Ltd.

[5] P. S. Ringrose and T. A. Meckel, "Maturing global co2 storage resources on offshore continental margins to achieve 2ds emissions reductions," *Scientific reports*, vol. 9, no. 1, pp. 1–10, 2019.

[6] A. Hamieh, F. Rowaihy, M. Al-Juaied, A. N. Abo-Khatwa, A. M. Afifi, and H. Hoteit, "Quantification and analysis of CO2 footprint from industrial facilities in Saudi Arabia," *Energy Conversion and Management: X*, vol. 16, p. 100299, Dec. 2022. [Online]. Available: https://www.sciencedirect.com/science/article/pii/S2590174522001222

[7] J. Ye, A. Afifi, F. Rowaihy, G. Baby, A. De Santiago, A. Tasianas, A. Hamieh, A. Khodayeva, M. Al-Juaied, T. A. Meckel, and H. Hoteit, "Evaluation of geological CO2 storage potential in Saudi Arabian sedimentary basins," *Earth-Science Reviews*, vol. 244, p. 104539, Sep. 2023. [Online]. Available: https://www.sciencedirect.com/science/article/pii/S0012825223002283

[8] B. Dupuy, S. Garambois, A. Asnaashari, H. Balhareth, M. Landro, A. Stovas, and J. Virieux, "Estimation of rock physics properties from seismic attributes - Part 2: Applications," *GEOPHYSICS*, vol. 81, no. 4, pp. M55–M69, Jul. 2016.

[9] B. Dupuy, P. Nordmann, A. Romdhane, and P. Eliasson, "Bayesian rock physics inversion for CO2 storage monitoring," in *4th EAGE Conference on Petroleum Geostatistics*. European Association of Geoscientists and Engineers, EAGE, 2019.

[10] B. Dupuy, A. Romdhane, P. Eliasson, and H. Yan, “Combined geophysical and rock physics workflow for quantitative CO2 monitoring,” *International Journal of Greenhouse Gas Control*, vol. 106, Mar. 2021, publisher: Elsevier Ltd.

[11] M. Maleki, A. Davolio, and D. J. Schiozer, “Using simulation and production data to resolve ambiguity in interpreting 4d seismic inverted impedance in the norne field,” *Petroleum Geoscience*, vol. 24, no. 3, pp. 335–347, 2018.

[12] ——, “Qualitative time-lapse seismic interpretation of norne field to assess challenges of 4d seismic attributes,” *The Leading Edge*, vol. 37, no. 10, pp. 754–762, 2018.

[13] C. Sambo, C. C. Iferobia, A. A. Babasafari, S. Rezaei, and O. A. Akanni, “The Role of Time Lapse(4D) Seismic Technology as Reservoir Monitoring and Surveillance Tool: A Comprehensive Review,” *Journal of Natural Gas Science and Engineering*, vol. 80, p. 103312, Aug. 2020, publisher: Elsevier.

[14] R. A. Chadwick, R. Arts, and O. Eiken, “4D seismic quantification of a growing CO2 plume at Sleipner, North Sea,” in *Petroleum Geology Conference Proceedings*, vol. 6, 2005, pp. 1385–1399, issue: 0 ISSN: 20479921.

[15] N. Delepine, K. Labat, V. Clochard, P. Ricarte, and C. Le Bras, “4D joint pre-stack seismic stratigraphic inversion of the Sleipner-CO2 Case,” vol. 4, 2010, pp. 2876–2880. [Online]. Available: https://www.scopus.com/inward/record.uri?eid=2-s2.0-78249255794&partnerID=40&md5=c01a19deb9f191a40fc4c20d4a6daa44

[16] S. Danaei, M. Hermana, and D. P. Ghosh, “4D seismic reservoir surveillance for a field located in Malaysian basins using different time-lapse seismic attributes,” *79th EAGE Conference and Exhibition 2017*, 2017, publisher: European Association of Geoscientists and Engineers, EAGE ISBN: 9789462822177.

[17] A.-K. Furre and O. Eiken, “Dual sensor streamer technology used in Sleipner CO 2 injection monitoring,” *Geophysical Prospecting*, vol. 62, pp. 1075–1088, 2014. [Online]. Available: https://onlinelibrary.wiley.com/doi/10.1111/1365-2478.12120

[18] A. Furre, A. Kiær, and O. Eiken, “CO2-induced seismic time shifts at Sleipner,” *INTERPRETATION-A JOURNAL OF SUBSURFACE CHARACTERIZATION*, vol. 3, no. 3, pp. SS23–SS35, Aug. 2015.

[19] A. Furre, O. Eiken, H. Alnes, J. Vevatne, and A. Kiær, “20 years of monitoring CO2-injection at Sleipner,” T. Dixon, L. Laloui, and S. Twinning, Eds., vol. 114, 2017, pp. 3916–3926.

[20] G. A. Williams and R. A. Chadwick, “An Improved History-match for Layer Spreading within the Sleipner Plume Including Thermal Propagation Effects,” *Energy Procedia*, vol. 114, pp. 2856–2870, 2017, publisher: Elsevier Ltd.

[21] ——, “Influence of reservoir-scale heterogeneities on the growth, evolution and migration of a CO2 plume at the Sleipner Field, Norwegian North Sea,” *International Journal of Greenhouse Gas Control*, vol. 106, Mar. 2021, publisher: Elsevier Ltd.

[22] A. Soares, “Direct Sequential Simulation and Cosimulation,” *Mathematical Geology 2001 33:8*, vol. 33, no. 8, pp. 911–926, 2001, publisher: Springer. [Online]. Available: https://link.springer.com/article/10.1023/A:1012246006212

[23] A. Soares, R. Nunes, and L. Azevedo, “Integration of Uncertain Data in Geostatistical Modelling,” *Mathematical Geosciences*, vol. 49, no. 2, pp. 253–273, 2017, publisher: Springer Verlag. [Online]. Available: https://www.scopus.com/inward/record.uri?eid=2-s2.0-85007552751&doi=10.1007%2fs11004-016-9667-5&partnerID=40&md5=630ebae1bab7a7fd958c72a6047bbcbf

[24] L. Azevedo, J. Narciso, R. Nunes, and A. Soares, “Self-updating local distributions in geostatistical seismic inversion,” in *4th EAGE Conference on Petroleum Geostatistics*. European Association of Geoscientists and Engineers, EAGE, 2019. [Online]. Available: https://www.scopus.com/inward/record.uri?eid=2-s2.0-85073103131&doi=10.3997%2f2214-4609.201902268&partnerID=40&md5=e2b5caaa9a9dd6cb4bfe9f89edac5faf

[25] ——, “Geostatistical seismic inversion with self-updating of local probability distributions,” *Mathematical Geosciences*, vol. 53, no. 5, pp. 1073–1093, 2021, cited By 3.

[26] [U+FFFD] Pereira, L. Azevedo, and [U+FFFD] A. Soares, “Updating Local Anisotropies with Template Matching During Geostatistical Seismic Inversion,” *Mathematical Geosciences 2023*, pp. 1–23, Mar. 2023, publisher: Springer. [Online]. Available: https://link.springer.com/article/10.1007/s11004-023-10051-3

[27] R. Miele, D. Grana, J. Costa, P. Bürkle, L. Varella, B. Barreto, and L. Azevedo, “Permeability prediction with geostatistical seismic inversion constrained by rock physics,” in *2nd EAGE Conference on Seismic Inversion*. EAGE Publishing BV, 2022. [Online]. Available: https://www.scopus.com/inward/record.uri?eid=2-s2.0-85125185889&doi=10.3997%2f2214-4609.202229032&partnerID=40&md5=ea62a2de8dc5d29a24a2501f9fa9e6cc

[28] M. Cyz, L. Azevedo, and M. Malinowski, “Application of geostatistical seismic AVA inversion for shale reservoir characterization and brittleness prediction with machine learning,” in *81st EAGE Conference and Exhibition 2019*. EAGE Publishing BV, 2019.

[Online]. Available: https://www.scopus.com/inward/record.uri?eid=2-s2.0-85086058765&doi=10.3997%2f2214-4609.201900691&partnerID=40&md5=f8f4639087c1c0dd8ae1f75c7c86c454

[29] A. J. Cavanagh and R. S. Haszeldine, "The Sleipner storage site: Capillary flow modeling of a layered CO2 plume requires fractured shale barriers within the Utsira Formation," *International Journal of Greenhouse Gas Control*, vol. 21, pp. 101–112, 2014, publisher: Elsevier Ltd.

[30] D. Grana and T. Mukerji, "Bayesian inversion of time-lapse seismic data for the estimation of static reservoir properties and dynamic property changes," *Geophysical Prospecting*, vol. 63, no. 3, pp. 637–655, 2015.

[31] A. Soares and L. Azevedo, *Geostatistics for seismic characterization of oil reservoirs*. Springer International Publishing, 2018, publication Title: Handbook of Mathematical Geosciences: Fifty Years of IAMG. [Online]. Available: https://www.scopus.com/inward/record.uri?eid=2-s2.0-85053358197&doi=10.1007%2f978-3-319-78999-6_25&partnerID=40&md5=d5a772e7b200396b2b55336d93262bdf

[32] A. Abbas Babasafari, S. Rezaei, [U+FFFD] Ahmed, M. A. Salim, [U+FFFD] Sayed, H. Kazemeini, and D. P. Ghosh, "Petrophysical seismic inversion based on lithofacies classification to enhance reservoir properties estimation: a machine learning approach," vol. 11, pp. 673–684, 2021, iSBN: 0123456789. [Online]. Available: https://doi.org/10.1007/s13202-020-01013-0

[33] M. Cyz and L. Azevedo, "Direct Geostatistical Seismic Amplitude Versus Angle Inversion for Shale Rock Properties," *IEEE Transactions on Geoscience and Remote Sensing*, vol. 59, no. 6, pp. 5335–5344, 2021, publisher: Institute of Electrical and Electronics Engineers Inc. [Online]. Available: https://www.scopus.com/inward/record.uri?eid=2-s2.0-85106689011&doi=10.1109%2fTGRS.2020.3017091&partnerID=40&md5=6eea897c53b65ba2c8a0a483723e8822

[34] R. Miele, D. Grana, L. E. Seabra Varella, B. Viola Barreto, and L. Azevedo, "Iterative geostatistical seismic inversion with rock physics constraints for permeability prediction," *GEOPHYSICS*, pp. 1–51, Mar. 2023, publisher: Society of Exploration Geophysicists.

[35] P. Avseth, T. Mukerji, and G. Mavko, "Quantitative seismic interpretation: Applying rock physics tools to reduce interpretation risk," *Quantitative Seismic Interpretation*, 2005.

[36] D. Grana, L. Azevedo, L. De Figueiredo, P. Connolly, and T. Mukerji, "Probabilistic inversion of seismic data for reservoir petrophysical characterization: Review and examples," *Geophysics*, vol. 87, no. 5, 2022, publisher: Society of Exploration Geophysicists. [Online]. Available: https://www.scopus.com/inward/record.uri?eid=2-s2.0-85133013150&doi=10.1190%2fgeo2021-0776.1&partnerID=40&md5=5642460cd0bfa84c913a9ad82c8631d6

[37] A. Tarantola, *Inverse problem theory and methods for model parameter estimation*. SIAM, 2005.

[38] M. Bosch, T. Mukerji, and E. Gonzalez, "Seismic inversion for reservoir properties combining statistical rock physics and geostatistics: A review," *Geophysics*, vol. 75, no. 5, pp. X75A165–75A176, 2010.

[39] B. Russell, "Introduction to seismic inversion methods," *Introduction to Seismic Inversion Methods*, 1988, cited By 197.

[40] B. Russell and D. Hampson, "Comparison of poststack seismic inversion methods," 1991, pp. 876–878, cited By 208.

[41] T. Tylor-Jones and L. Azevedo, *A Practical Guide to Seismic Reservoir Characterization*. Springer Nature, 2023.

[42] S. Lancaster and D. Whitcombe, "Fast-track 'coloured' inversion," 2000, cited By 35.

[43] A. Buland and H. Omre, "Bayesian linearized AVO inversion," *Geophysics*, vol. 68, no. 1, pp. 185–198, 2003.

[44] D. Grana and E. Della Rossa, "Probabilistic petrophysical-properties estimation integrating statistical rock physics with seismic inversion," *Geophysics*, vol. 75, no. 3, pp. XO21–O37, 2010, cited By 386.

[45] D. Grana, T. Fjeldstad, and H. Omre, "Bayesian gaussian mixture linear inversion for geophysical inverse problems," *Mathematical Geosciences*, vol. 49, no. 4, pp. 493–515, 2017, cited By 132.

[46] M. Bosch, "Lithologic tomography: From plural geophysical data to lithology estimation," *Journal of Geophysical Research: Solid Earth*, vol. 104, no. B1, pp. 749–766, 1999.

[47] L. Azevedo, R. Nunes, A. Soares, E. Mundin, and G. Neto, "Integration of well data into geostatistical seismic amplitude variation with angle inversion for facies estimation," *Geophysics*, vol. 80, no. 6, pp. M113–M128, 2015, publisher: Society of Exploration Geophysicists. [Online]. Available: https://www.scopus.com/inward/record.uri?eid=2-s2.0-84940759199&doi=10.1190%2fGEO2015-0104.1&partnerID=40&md5=02a60150ae609f4cb16c680fcfb5f9f5

[48] L. Azevedo and A. Soares, "Geostatistical methods for reservoir geophysics," *Geostatistical Methods for Reservoir Geophysics*, 2017, cited By 90.

[49] P. Avseth, T. Mukerji, and G. Mavko, *Quantitative seismic interpretation: Applying rock physics tools to reduce interpretation risk*, 2010. [Online]. Available: https://books.google.com/books?hl=en&lr=&id=rKYhAwAAQBAJ&oi=fnd&pg=PR1&ots=u4EN1tGwyo&sig=6gWi4LFKvcGbQu-nX9Lt5UfK3_E

[50] T. N. Meek, M. Professor, and M. Totten, “Applications of 3D seismic attribute analysis workflows: a case study from Ness County, Kansas, USA,” 2015. [Online]. Available: http://krex.k-state.edu/dspace/handle/2097/19000

[51] F. Barclay, A. Bruun, K. Rasmussen, J. A. O. . . . , and u. 2008, “Seismic inversion: Reading between the lines,” *oarklibrary.com*.

[52] K. D. Oyeyemi, M. T. Olowokere, and A. P. Aizebeokhai, “Evaluation of optimal reservoir prospectivity using acoustic-impedance model inversion: A case study of an offshore field, western Niger Delta, Nigeria,” *NRIAG Journal of Astronomy and Geophysics*, vol. 6, no. 2, pp. 300–310, Dec. 2017, publisher: Informa UK Limited.

[53] K. Aki and P. Richards, *Quantitative Seismology: Theory and Methods*, 1980.

[54] G. Mavko, T. Mukerji, and J. Dvorkin, “The Rock Physics Handbook,” Jan. 2020, iSBN: 9781108333016 9781108420266 Publisher: Cambridge University Press. [Online]. Available: https://www.cambridge.org/core/books/rock-physics-handbook/667464585A2B42E10B345B0217D8442F

[55] L. Azevedo, R. Nunes, P. Correia, A. Soares, G. Neto, and L. Guerreiro, “Stochastic direct facies seismic AVO inversion,” in *Society of Exploration Geophysicists International Exposition and 83rd Annual Meeting, SEG 2013: Expanding Geophysical Frontiers*. Society of Exploration Geophysicists, 2019, pp. 2352–2356. [Online]. Available: https://www.scopus.com/inward/record.uri?eid=2-s2.0-85058108797&doi=10.1190%2fsegam2013-0555.1&partnerID=40&md5=a19dd2ef528aaf53b0d7ee4a2e4a5e6c

[56] T. Taha, P. Ward, G. Peacock, J. H. S. R. . . . , and u. 2019, “History matching using 4D seismic in an integrated multi-disciplinary automated workflow,” *onepetro.org*. [Online]. Available: https://onepetro.org/SPERCSC/proceedings-abstract/19RCSC/3-19RCSC/D031S022R001/219080

[57] O. Gosselin, S. I. Aanonsen, I. Aavatsmark, A. Cominelli, R. Gonard, M. Kolasinski, F. Ferdinandi, L. Kovacic, and K. Neylon, “History Matching Using Time-lapse Seismic (HUTS),” *Proceedings - SPE Annual Technical Conference and Exhibition*, pp. 3647–3661, Oct. 2003, publisher: OnePetro.

[58] P. Pinto, L. Azevedo, M. Ribeiro, and J. Gomes, “Compositional simulation for time-lapse seismic modelling on a synthetic reservoir with a high content of CO2,” in *Society of Petroleum Engineers - Abu Dhabi International Petroleum Exhibition and Conference 2016*, vol. 2016-January. Society of Petroleum Engineers, 2016. [Online]. Available: https://www.scopus.com/inward/record.uri?eid=2-s2.0-85044363602&doi=10.2118%2f183212-ms&partnerID=40&md5=20f57da7ee10f49759c30939659c5082

[59] P. Thore, H. Klemm, and L. Azevedo, "The impact of seismic inversion methods on facies prediction," in *1st EAGE Conference on Seismic Inversion*. European Association of Geoscientists and Engineers, EAGE, 2020. [Online]. Available: https://www.scopus.com/inward/record.uri?eid=2-s2.0-85126453529&doi=10.3997%2f2214-4609.202037021&partnerID=40&md5=1029aa510149f3b30e2d21e870e8f217

[60] D. S. Oliver, K. Fossum, T. Bhakta, I. Sandø, G. Nævdal, and R. J. Lorentzen, "4d seismic history matching," *Journal of Petroleum Science and Engineering*, vol. 207, p. 109119, 2021.

[61] D. R. Rosa, J. M. Santos, R. M. Souza, D. Grana, D. J. Schiozer, A. Davolio, and Y. Wang, "Comparing different approaches of time-lapse seismic inversion," *Journal of geophysics and engineering*, vol. 17, no. 6, pp. 929–939, 2020.

[62] A. Soares, J. Diet, and L. Guerreiro, "Stochastic inversion with a global perturbation method," in *Petroleum Geostatistics 2007*, Cascais, 2007. [Online]. Available: https://www.scopus.com/inward/record.uri?eid=2-s2.0-84900668117&partnerID=40&md5=fb9262949604b6ca500fe9aa447661f4

[63] L. Azevedo and A. Soares, "Integration of geophysical data for reservoir modeling and characterization," *Advances in Oil and Gas Exploration and Production*, pp. 51–89, 2017, publisher: Springer. [Online]. Available: https://www.scopus.com/inward/record.uri?eid=2-s2.0-85067984808&doi=10.1007%2f978-3-319-53201-1_4&partnerID=40&md5=87e616cc6ece2940c31d0bcdb5cb0e5e

[64] T. Hansen, A. Journel, A. Tarantola, and K. Mosegaard, "Linear inverse gaussian theory and geostatistics," *Geophysics*, vol. 71, no. 6, pp. R101–R111, 2006, cited By 140.

[65] U. Gregersen, O. Michelsen, and J. C. Sørensen, "Stratigraphy and facies distribution of the Utsira formation and the Pliocene sequences in the northern North Sea," *Marine and Petroleum Geology*, vol. 14, no. 7-8, pp. 893–914, Nov. 1997, publisher: Elsevier.

[66] R. A. Chadwick, G. A. Kirby, and S. Holloway, "Saline Aquifer CO2 Storage (SACS2) Final report: Geological Characterisation of the Utsira Sand reservoir and caprocks (Work Area 1)," Tech. Rep., 2002. [Online]. Available: www.thebgs.co.uk

[67] V. T. Pham, F. Riis, I. T. Gjeldvik, E. K. Halland, I. M. Tappel, and P. Aagaard, "Assessment of CO2 injection into the south Utsira-Skade aquifer, the North Sea, Norway," *Energy*, vol. 55, pp. 529–540, Jun. 2013, publisher: Elsevier Ltd.

[68] M. Hamborg, G. Kirby, A. E. Lothe, and P. Zweigel, "A contribution to the Saline Aquifer CO 2 Storage (SACS) project Seismic mapping and simulation of CO 2 migration in the upper Utsira sand wedge east of the Sleipner injection site," 2003. [Online]. Available: http://www.bgs.ac.uk/

[69] F. C. Boait, N. J. White, M. J. Bickle, R. A. Chadwick, J. A. Neufeld, and H. E. Huppert, "Spatial and temporal evolution of injected CO2 at the Sleipner Field, North Sea," *Wiley Online Library*, vol. 117, no. 3, p. 3309, Mar. 2012, publisher: Blackwell Publishing Ltd. [Online]. Available: https://agupubs.onlinelibrary.wiley.com/doi/abs/10.1029/2011JB008603

[70] A. Chadwick, G. Williams, N. Delepine, V. Clochard, K. Labat, S. Sturton, M. L. Buddensiek, M. Dillen, M. Nickel, A. L. Lima, R. Arts, F. Neele, and G. Rossi, "Quantitative analysis of time-lapse seismic monitoring data at the Sleipner CO2 storage operation," *Leading Edge (Tulsa, OK)*, vol. 29, no. 2, pp. 170–177, 2010, publisher: Society of Exploration Geophysicists.

[71] V. Singh, S. Asa, and A. Cavanagh, "SPE 134891 Reservoir Modeling of CO 2 Plume Behavior Calibrated Against Monitoring Data From Sleipner, Norway," Tech. Rep., 2010.

[72] A. Callioli Santi, P. Ringrose, J. Eidsvik, and T. A. Haugdahl, "Assessing co2 storage containment risks using an invasion percolation markov chain concept," *Available at SSRN 4282992*, 2022.

[73] K. Bateman, C. A. Rochelle, G. Purser, S. J. Kemp, and D. Wagner, "Geochemical Interactions Between CO2 and Minerals within the Utsira Caprock: A 5-year Experimental Study," *Energy Procedia*, vol. 37, pp. 5307–5314, Jan. 2013, publisher: Elsevier.

[74] I. Falcon-Suarez, G. Papageorgiou, A. Chadwick, L. North, A. I. Best, and M. Chapman, "CO2-brine flow-through on an Utsira Sand core sample: Experimental and modelling. Implications for the Sleipner storage field," *International Journal of Greenhouse Gas Control*, vol. 68, pp. 236–246, Jan. 2018. [Online]. Available: https://www.sciencedirect.com/science/article/pii/S1750583617306370

[75] M. Queißer and S. Singh, "Time lapse seismic monitoring of CO2 sequestration at Sleipner using time domain 2D full waveform inversion," 2010, pp. 2875–2879. [Online]. Available: https://www.scopus.com/inward/record.uri?eid=2-s2.0-84949185358&partnerID=40&md5=4a6d29bcfe568881fedc104cdb59dbb7

[76] A. Fornel and A. Estublier, "To a dynamic update of the sleipner CO2 storage geological model using 4D seismic data," vol. 37, 2013, pp. 4902–4909. [Online]. Available: https://www.scopus.com/inward/record.uri?eid=2-s2.0-84898759084&doi=10.1016%2fj.egypro.2013.06.401&partnerID=40&md5=78032ad0b750b60f7ef55203624518b6

[77] M. Queißer and S. Singh, "Full waveform inversion in the time lapse mode applied to CO2 storage at Sleipner," *Geophysical Prospecting*, vol. 61, no. 3, pp. 537–555, 2013. [Online]. Available: https://www.scopus.com/inward/record.uri?eid=2-s2.0-84876164988&doi=10.1111%2fj.1365-2478.2012.01072.x&partnerID=40&md5=3e045c50048da877ae26b280b726da22

[78] A. Romdhane and E. Querendez, “CO2 characterization at the Sleipner field with full waveform inversion: Application to synthetic and real data,” *Energy Procedia*, vol. 63, pp. 4358–4365, 2014, publisher: Elsevier Ltd.

[79] B. Li and Y. E. Li, “Neural Network-Based CO2 Interpretation From 4D Sleipner Seismic Images,” *Journal of Geophysical Research: Solid Earth*, vol. 126, no. 12, p. e2021JB022524, Dec. 2021, publisher: John Wiley & Sons, Ltd. [Online]. Available: https://onlinelibrary.wiley.com/doi/full/10.1029/2021JB022524

[80] B. Nazarian and A.-K. Furre, “Simulation Study of Sleipner Plume on Entire Utsira Using A Multi-Physics Modelling Approach,” 2022. [Online]. Available: https://doi.org/10.1016/j.egypro.2017.03.1523

[81] J. Romero, N. Luiken, and M. Ravasi, “Seeing through the CO2plume: Joint inversion-segmentation of the Sleipner 4D seismic data set,” *Leading Edge*, vol. 42, no. 7, pp. 457–464, 2023. [Online]. Available: https://www.scopus.com/inward/record.uri?eid=2-s2.0-85168308192&doi=10.1190%2ftle42070457.1&partnerID=40&md5=4a453150b873ddaf8cdea8893c829eef

[82] M. Liu, D. Vashisth, D. Grana, and T. Mukerji, “Joint Inversion of Geophysical Data for Geologic Carbon Sequestration Monitoring: A Differentiable Physics-Informed Neural Network Model,” *Journal of Geophysical Research: Solid Earth*, vol. 128, no. 3, p. e2022JB025372, 2023, _eprint: https://onlinelibrary.wiley.com/doi/pdf/10.1029/2022JB025372. [Online]. Available: https://onlinelibrary.wiley.com/doi/abs/10.1029/2022JB025372

[83] O. Andersen, G. Tangen, P. Ringrose, and S. E. Greenberg, “Co2 data share: a platform for sharing co2 storage reference datasets from demonstration projects,” in *14th greenhouse gas control technologies conference Melbourne*, 2018, pp. 21–26.

[84] F. Bordignon, L. Figueiredo, L. Azevedo, A. Soares, M. Roisenberg, and G. Neto, “Integration of bayesian linearized inversion into geostatistical seismic inversion,” in *78th EAGE Conference and Exhibition 2016*, vol. 2016, no. 1. European Association of Geoscientists & Engineers, 2016, pp. 1–5.

A

Appendix Inversion Results

A.1 Inversion Results L9 and L5

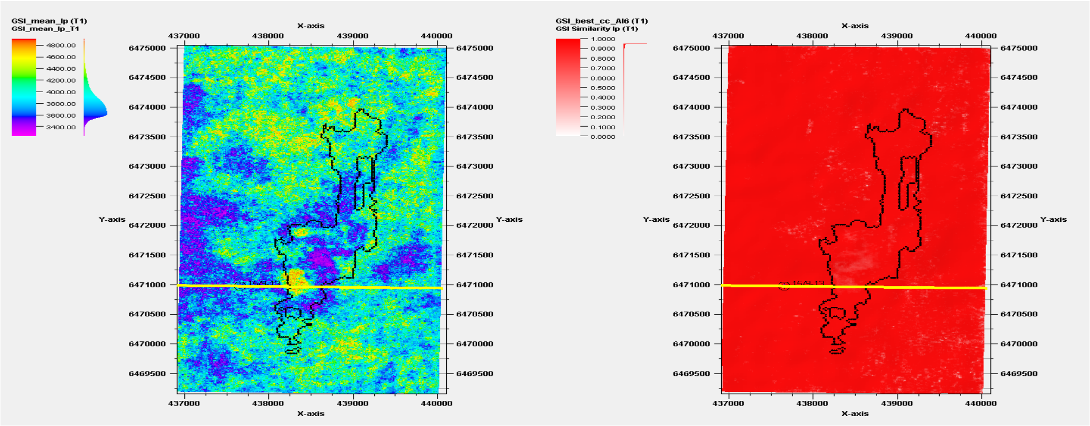

(a) Ip 2001 GSI

(b) best cc AI6 2001 GSI

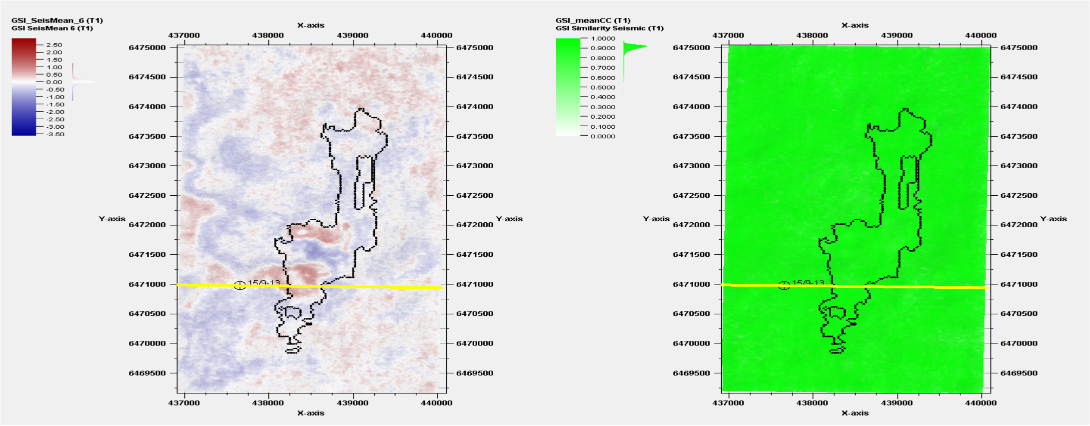

(c) Synthetic Seismic 2001 GSI

(d) Mean CC 2001 GSI

Figure A.1: Inversion Results 2001 L9 GSI

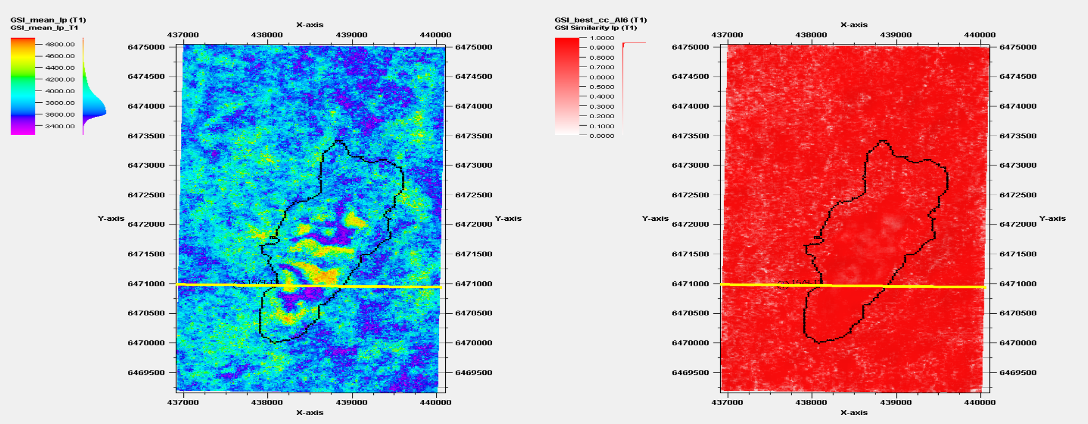

(a) Ip 2001 GSI

(b) best cc AI6 2001 GSI

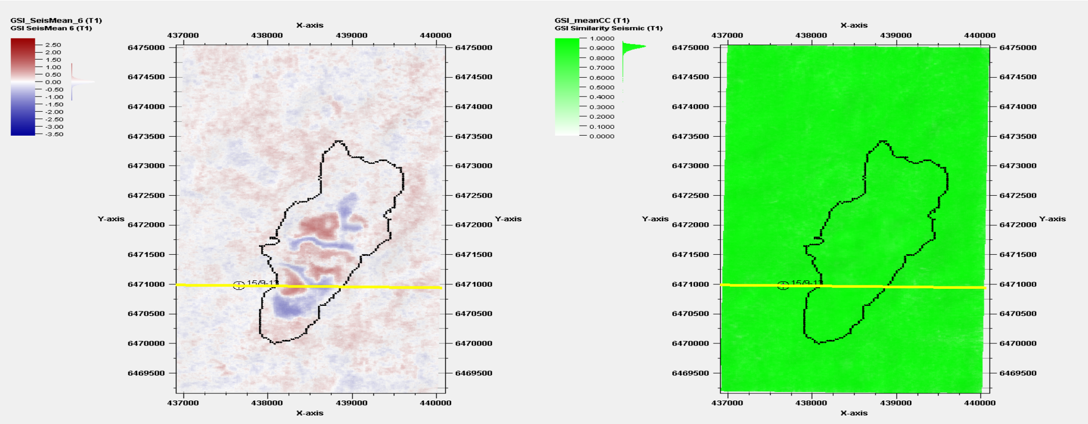

(c) Synthetic Seismic 2001 GSI

(d) Mean CC 2001 GSI

Figure A.2: Inversion Results 2001 L5 GSI

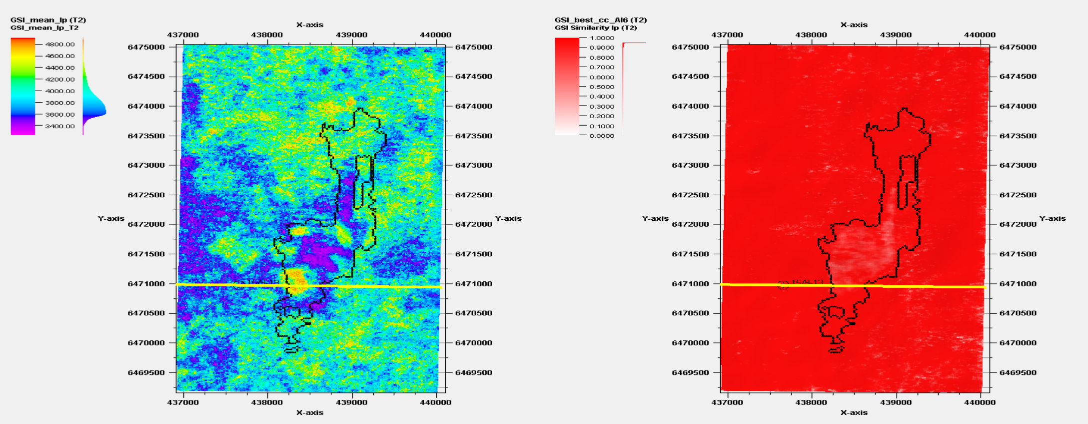

(a) Ip 2004 GSI **(b)** best cc AI6 2004 GSI

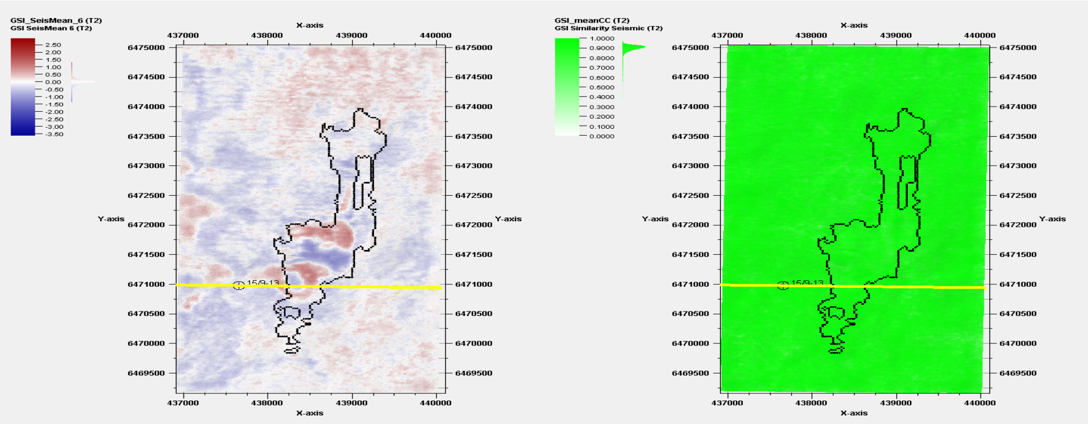

(c) Synthetic Seismic 2004 GSI **(d)** Mean CC 2004 GSI

Figure A.3: Inversion Results 2004 L9 GSI

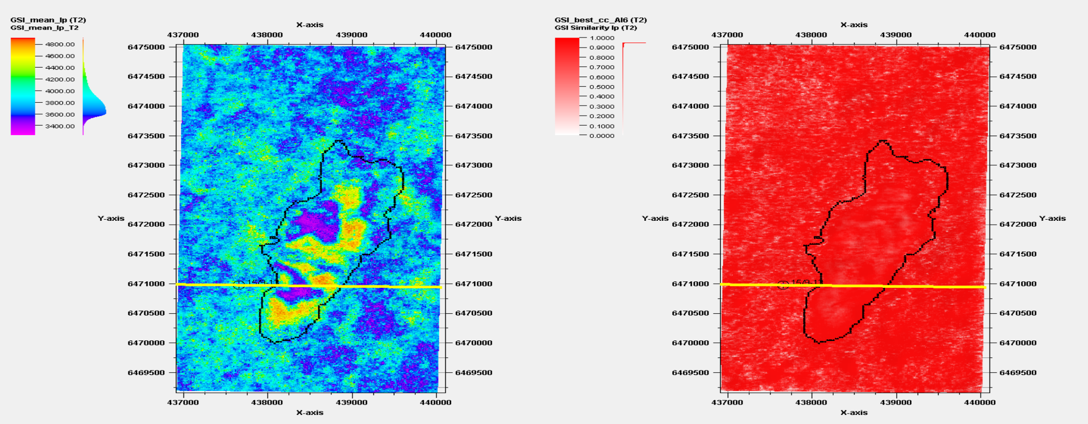

(a) Ip 2004 GSI

(b) best cc AI6 2004 GSI

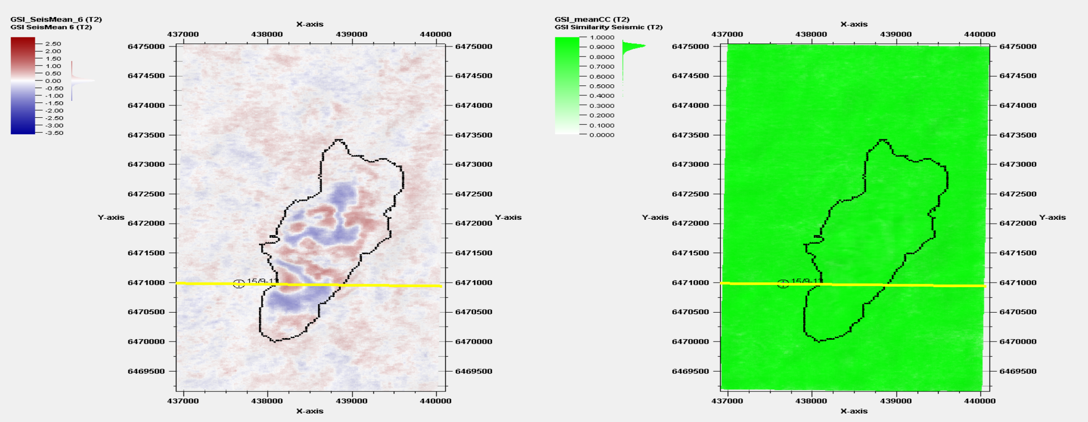

(c) Synthetic Seismic 2004 GSI

(d) Mean CC 2004 GSI

Figure A.4: Inversion Results 2004 L5 GSI

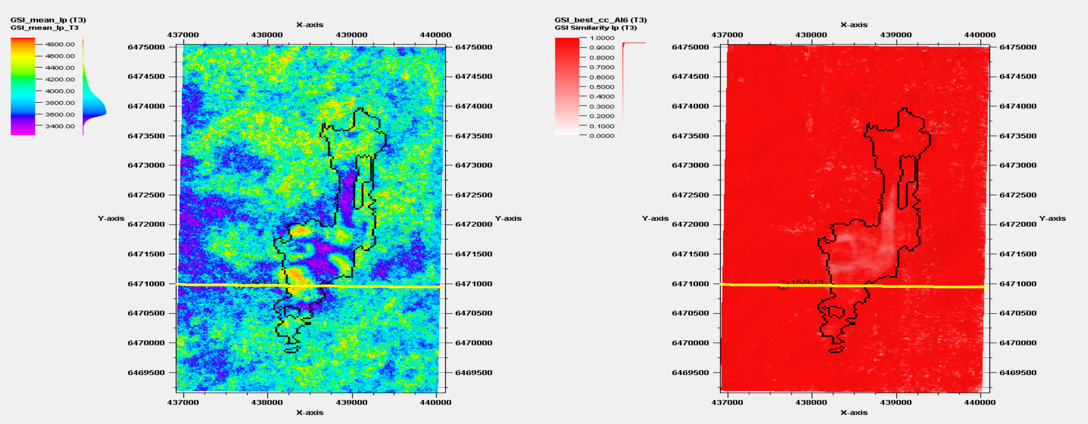

(a) Ip 2006 GSI **(b)** best cc AI6 2006 GSI

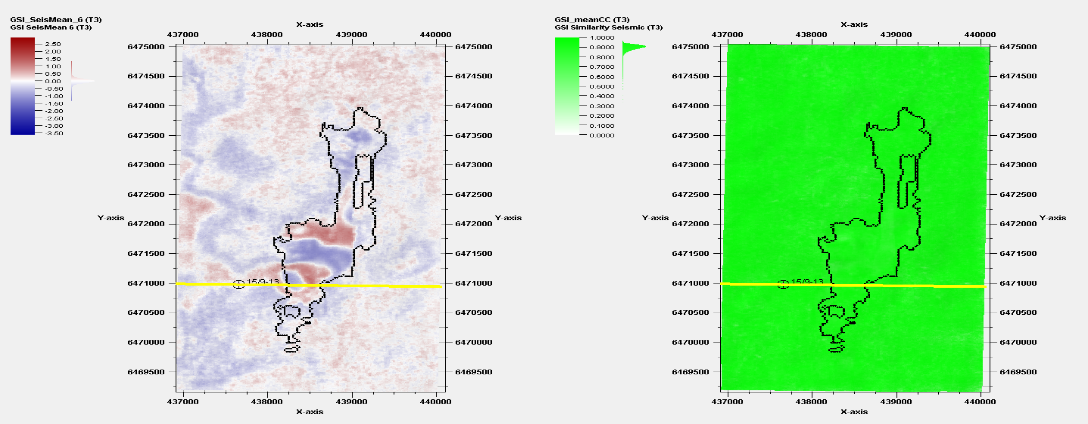

(c) Synthetic Seismic 2006 GSI **(d)** Mean CC 2006 GSI

Figure A.5: Inversion Results 2006 L9 GSI

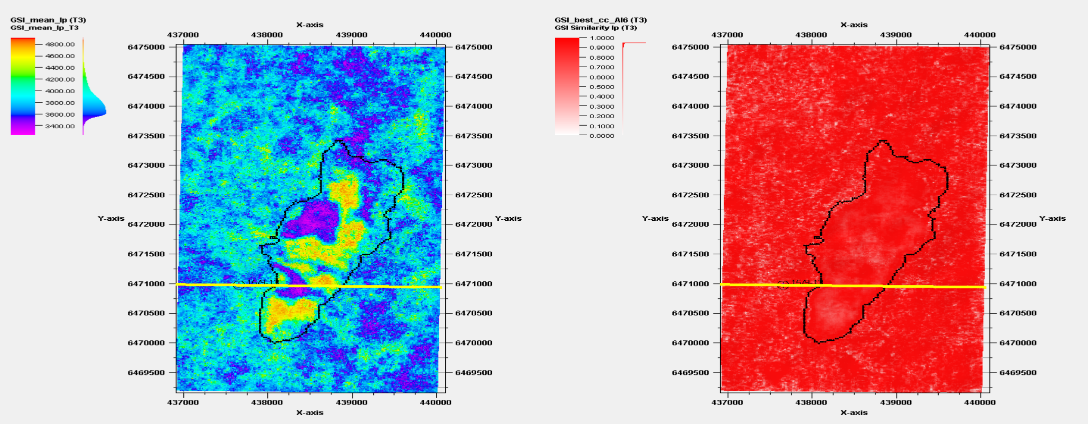

(a) Ip 2006 GSI **(b)** best cc AI6 2006 GSI

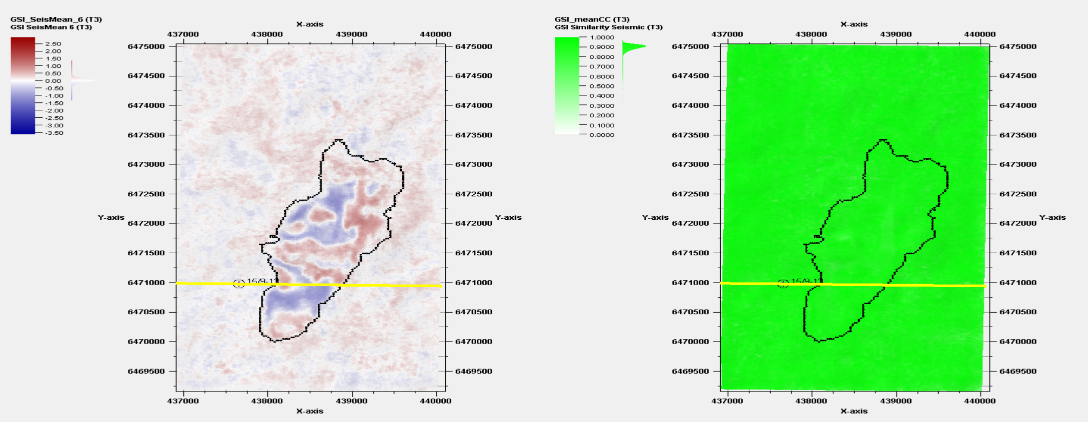

(c) Synthetic Seismic 2006 GSI **(d)** Mean CC 2006 GSI

Figure A.6: Inversion Results 2006 L5 GSI

A.2 GSI Processing L9

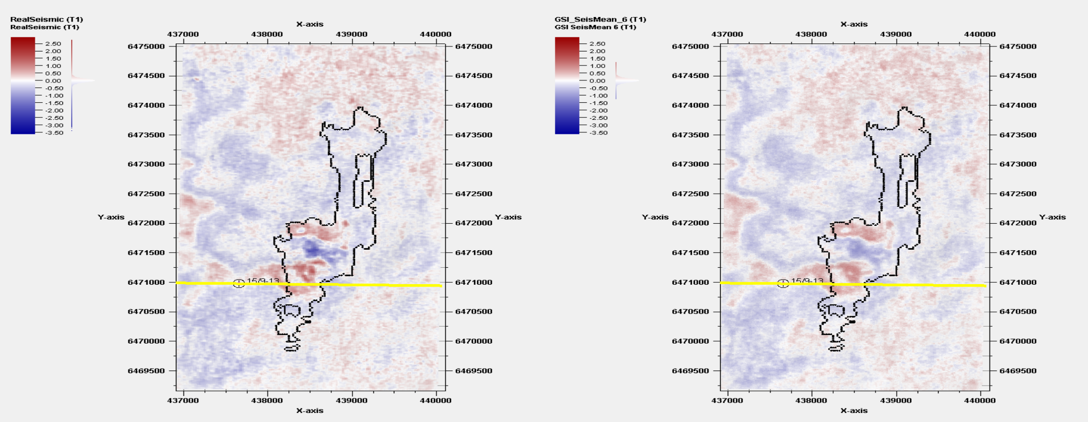

(a) Real Seismic 2001 **(b)** Synthetic Seismic 2001 GSI

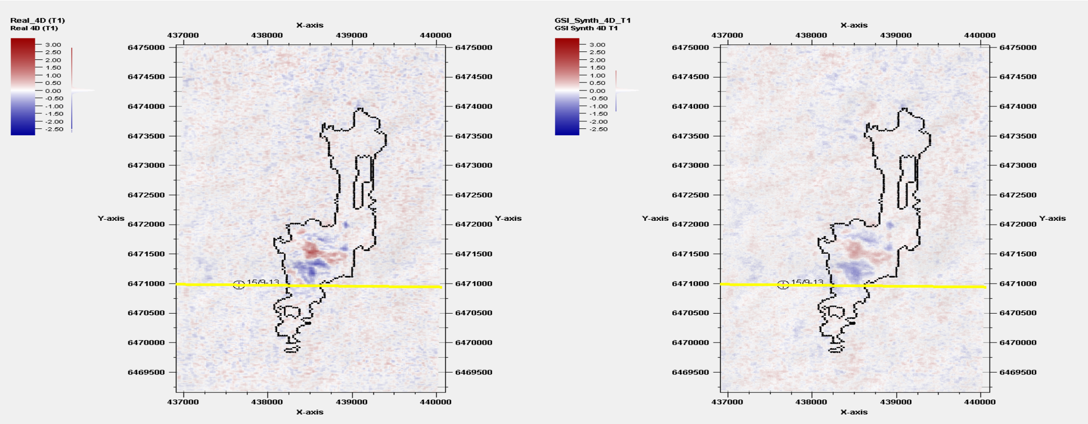

(c) Real Seismic Base minus Real Seismic Monitor **(d)** Real Seismic Base minus Synthetic Seismic Monitor 2001 GSI

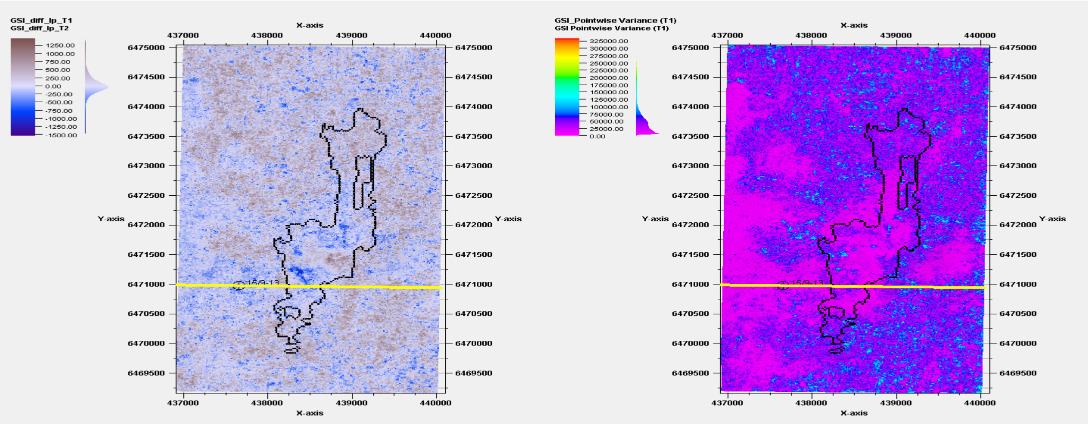

(e) Ip Base minus Ip Monitor 2001 GSI **(f)** Point-wise Variance

Figure A.7: Processing GSI 2001 L9 Results

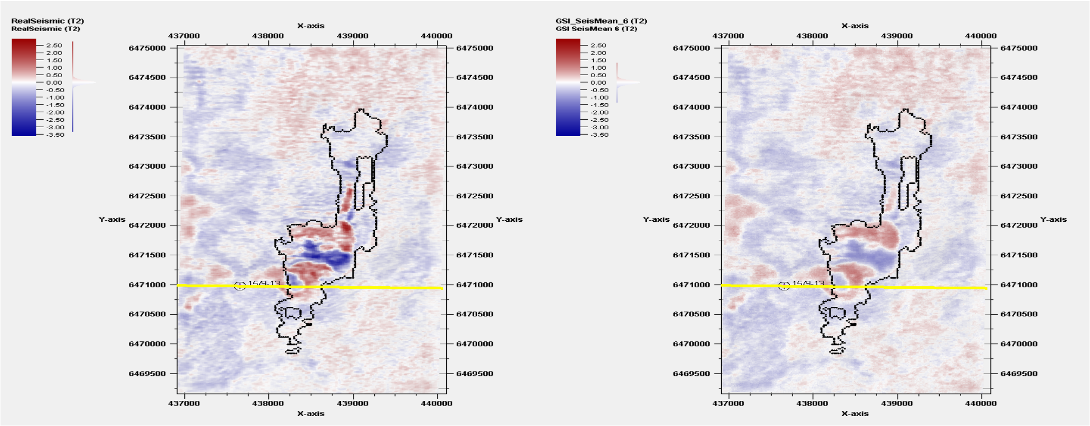

(a) Real Seismic 2004

(b) Synthetic Seismic 2004 GSI

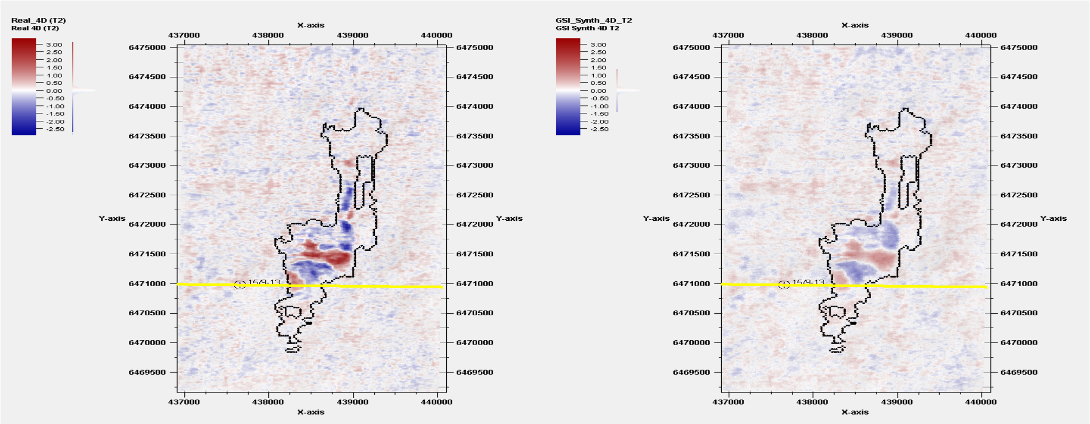

(c) Real Seismic Base minus Real Seismic Monitor 2004 GSI

(d) Real Seismic Base minus Synthetic Seismic Monitor 2004 GSI

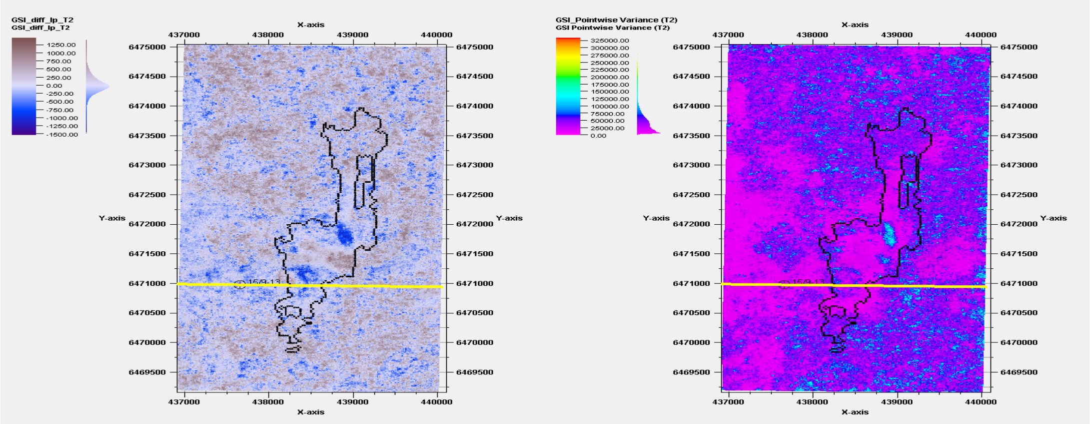

(e) Ip Base minus Ip Monitor 2004 GSI

(f) Point-wise Variance 2004 GSI

Figure A.8: Processing GSI 2004 Results L9

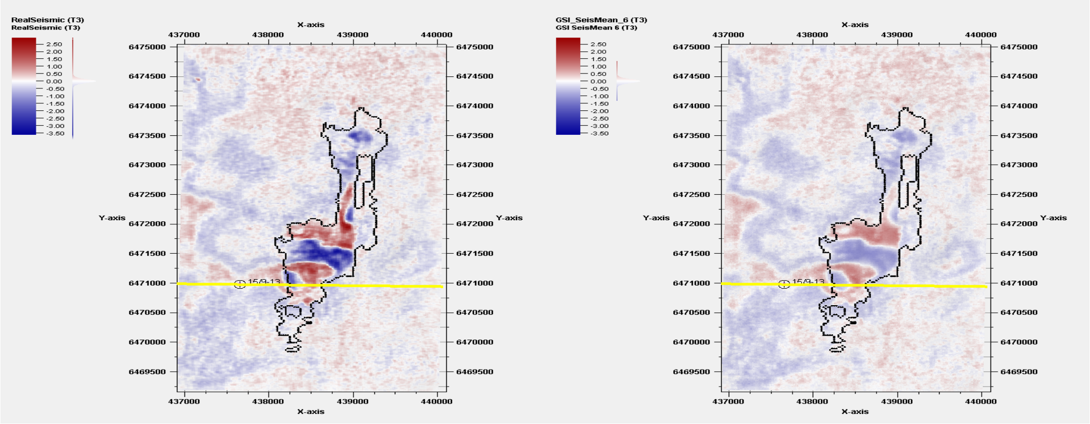

(a) Real Seismic 2006

(b) Synthetic Seismic 2006 GSI

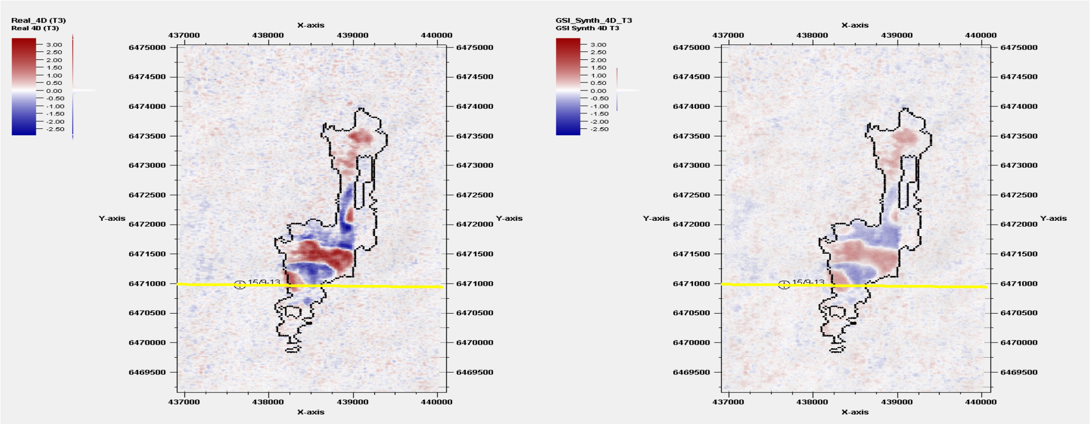

(c) Real Seismic Base minus Real Seismic Monitor

(d) Real Seismic Base minus Synthetic Seismic Monitor 2006 GSI

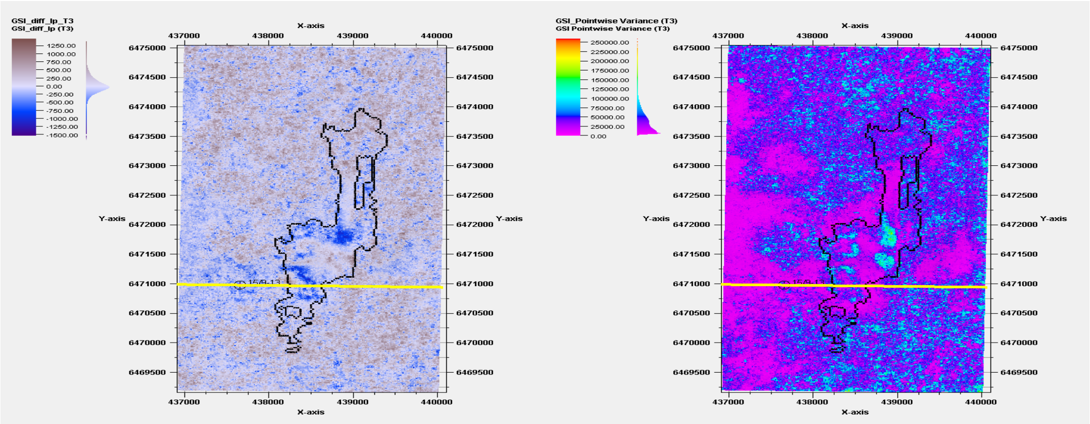

(e) Ip Base minus Ip Monitor 2006 GSI

(f) Point-wise Variance 2006 GSI

Figure A.9: Processing GSI 2006 Results L9

A.3 4D Inversion Results L9 and L5

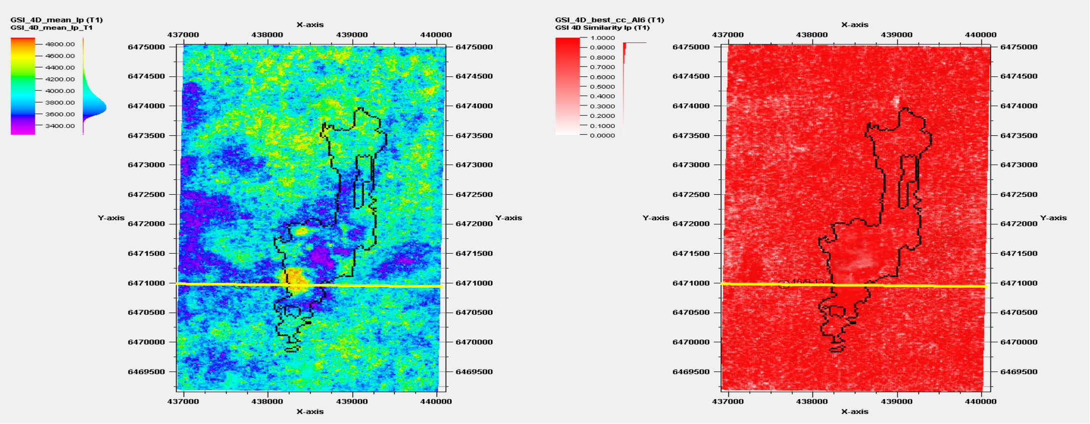

(a) Ip 2001 GSI 4D

(b) best cc AI6 2001 GSI 4D

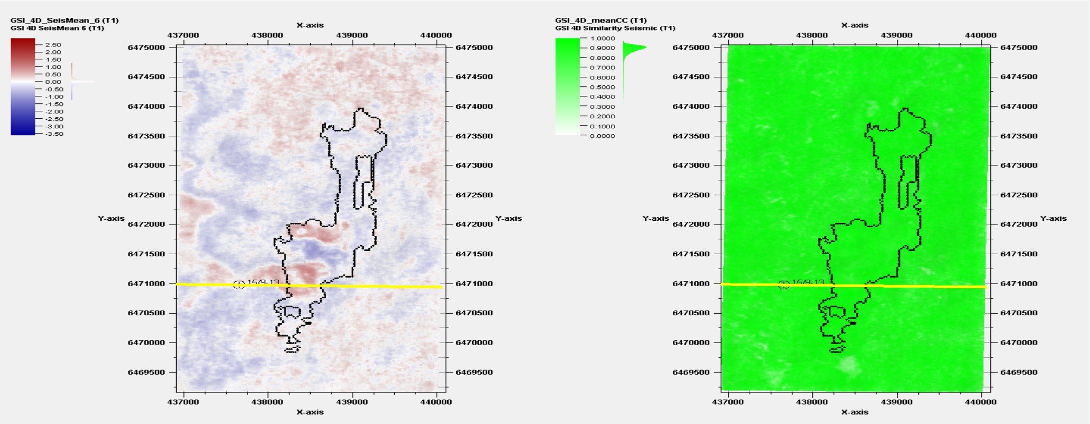

(c) Synthetic Seismic 2001 GSI 4D

(d) Mean CC 2001 GSI 4D

Figure A.10: Inversion Results 2001 L9 GSI 4D

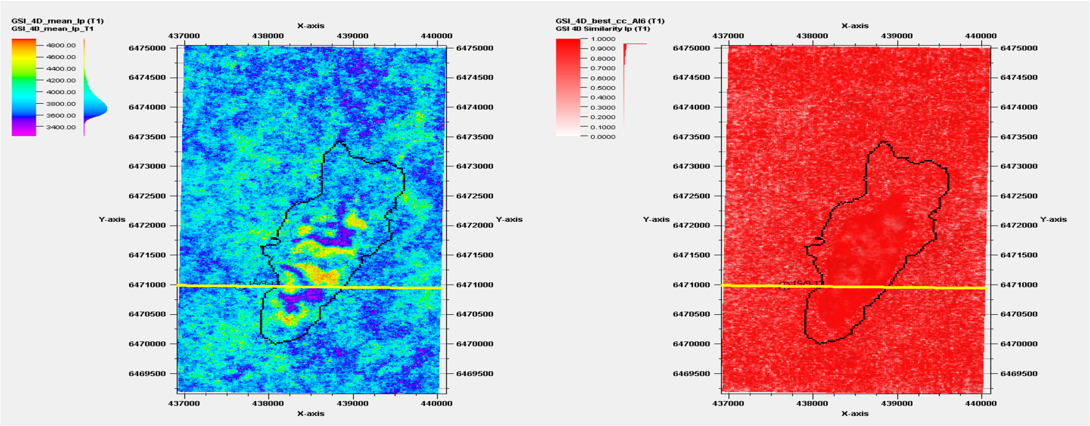

(a) Ip 2001 GSI 4D **(b)** best cc AI6 2001 GSI 4D

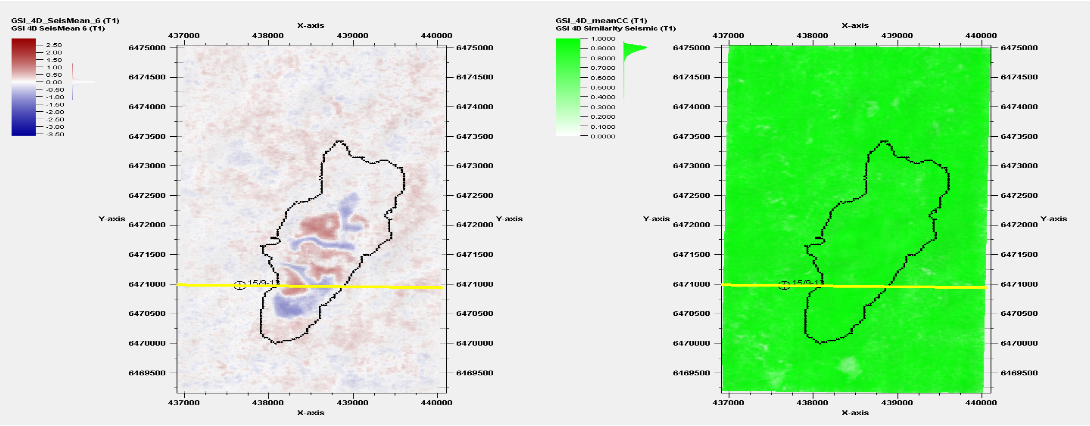

(c) Synthetic Seismic 2001 GSI 4D **(d)** Mean CC 2001 GSI 4D

Figure A.11: Inversion Results 2001 L5 GSI 4D

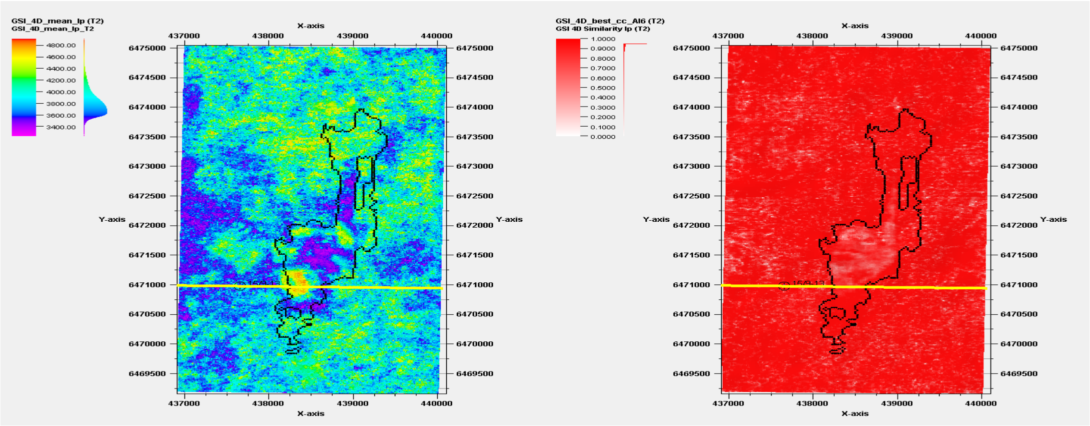

(a) Ip 2004 GSI 4D

(b) best cc AI6 2004 GSI 4D

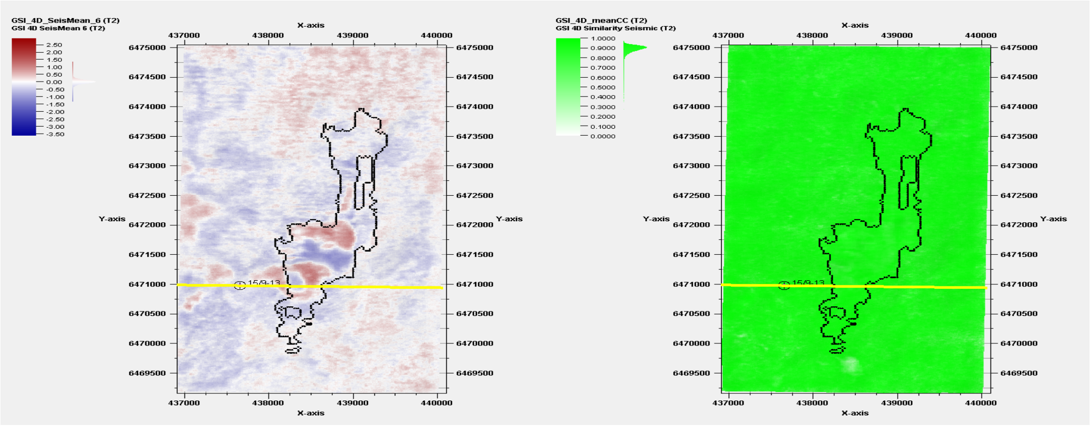

(c) Synthetic Seismic 2004 GSI 4D

(d) Mean CC 2004 GSI 4D

Figure A.12: Inversion Results 2004 L9 GSI 4D

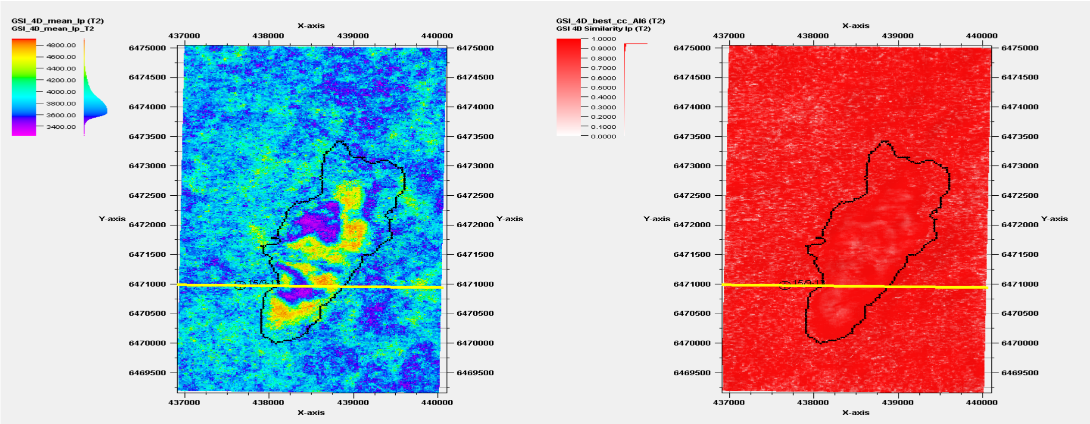

(a) Ip 2004 GSI 4D

(b) best cc AI6 2004 GSI 4D

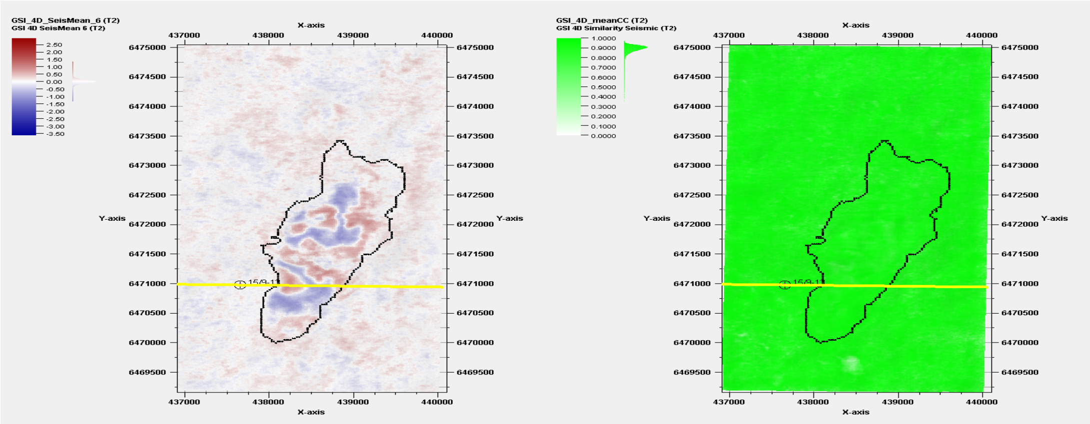

(c) Synthetic Seismic 2004 GSI 4D

(d) Mean CC 2004 GSI 4D

Figure A.13: Inversion Results 2004 L5 GSI 4D

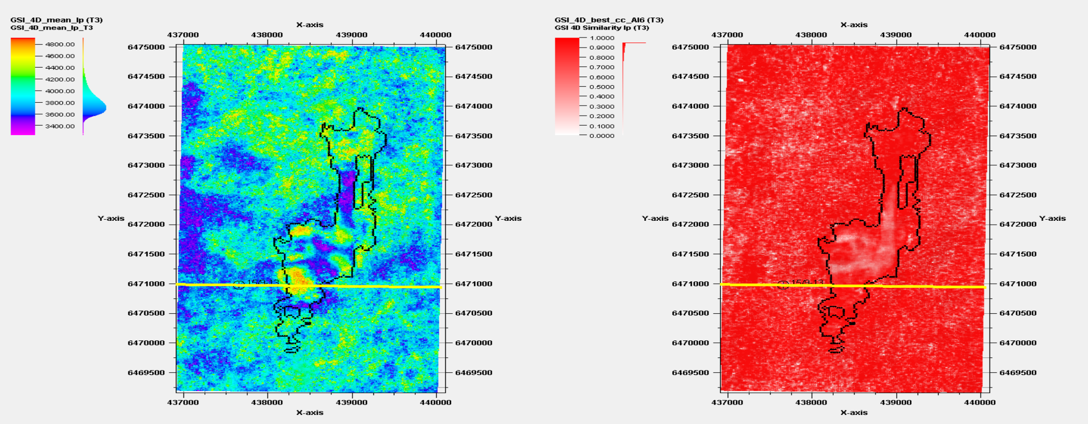

(a) Ip 2006 GSI 4D

(b) best cc AI6 2006 GSI 4D

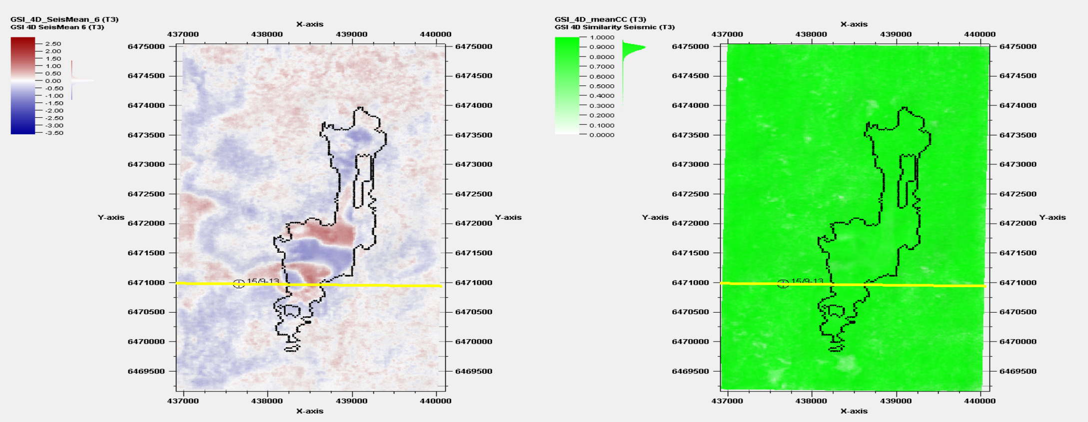

(c) Synthetic Seismic 2006 GSI 4D

(d) Mean CC 2006 GSI 4D

Figure A.14: Inversion Results 2006 L9 GSI 4D

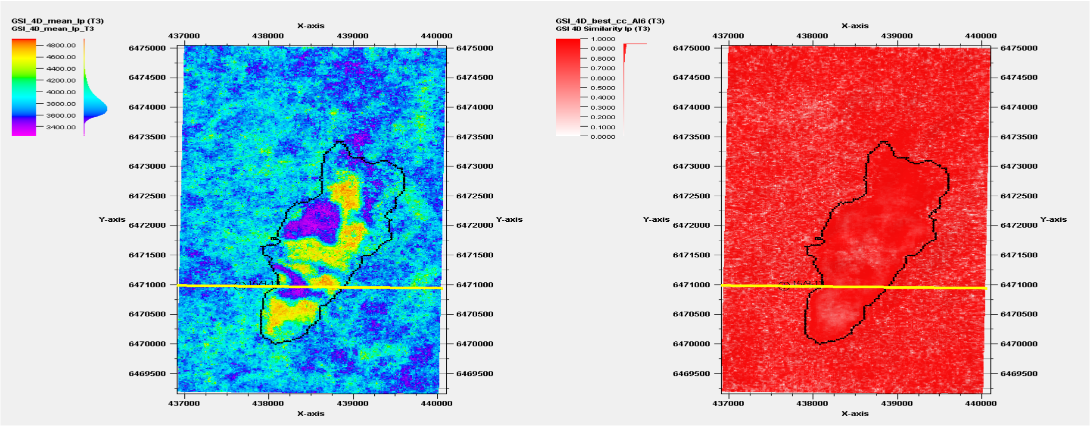

(a) Ip 2006 GSI 4D **(b)** best cc AI6 2006 GSI 4D

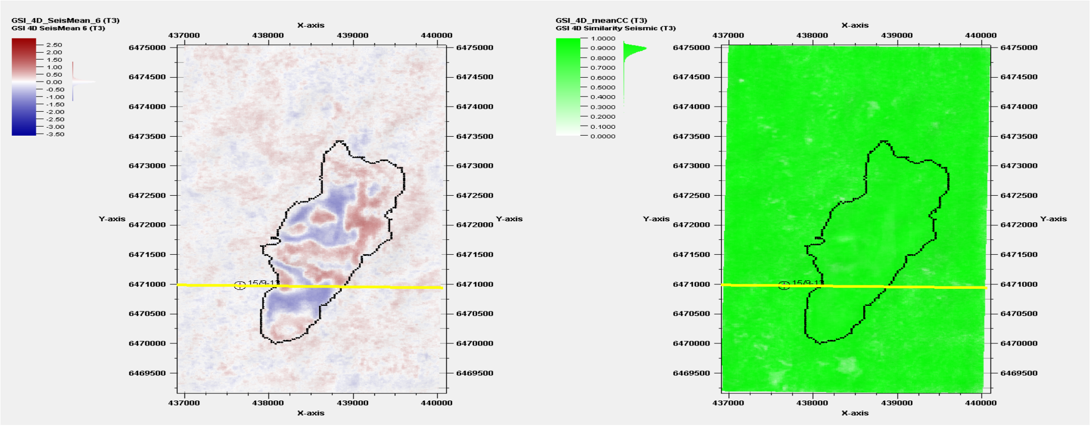

(c) Synthetic Seismic 2006 GSI 4D **(d)** Mean CC 2006 GSI 4D

Figure A.15: Inversion Results 2006 L5 GSI 4D

A.4 Processing 4D GSI L9

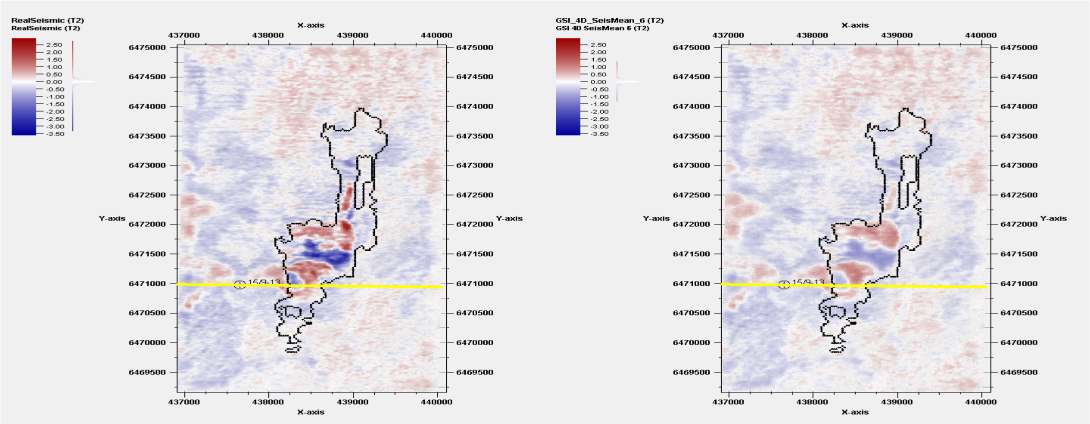

(a) Real Seismic 2004

(b) Synthetic Seismic 2004 GSI 4D

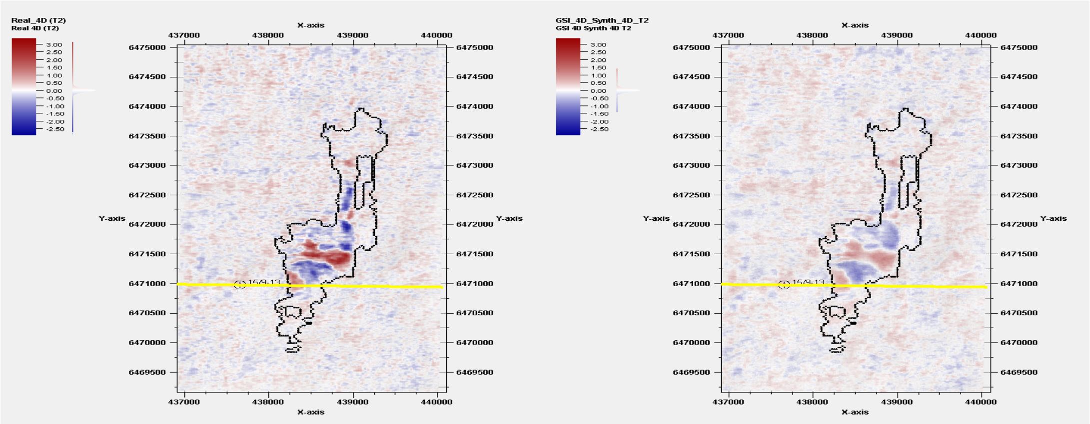

(c) Real Seismic Base minus Real Seismic Monitor

(d) Real Seismic Base minus Synthetic Seismic Monitor 2001 GSI 4D

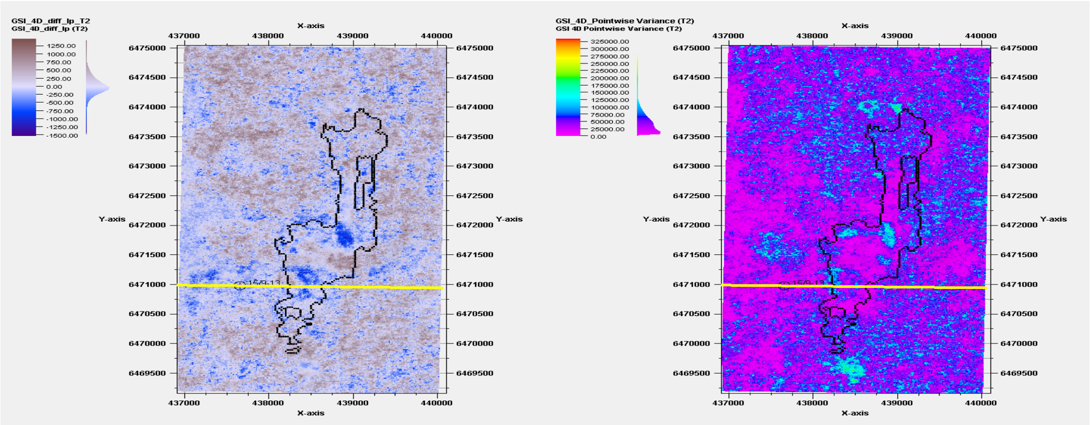

(e) Ip Base minus Ip Monitor 2001 GSI 4D

(f) Point-wise Variance

Figure A.16: Processeing GSI 4D 2004 Results L9

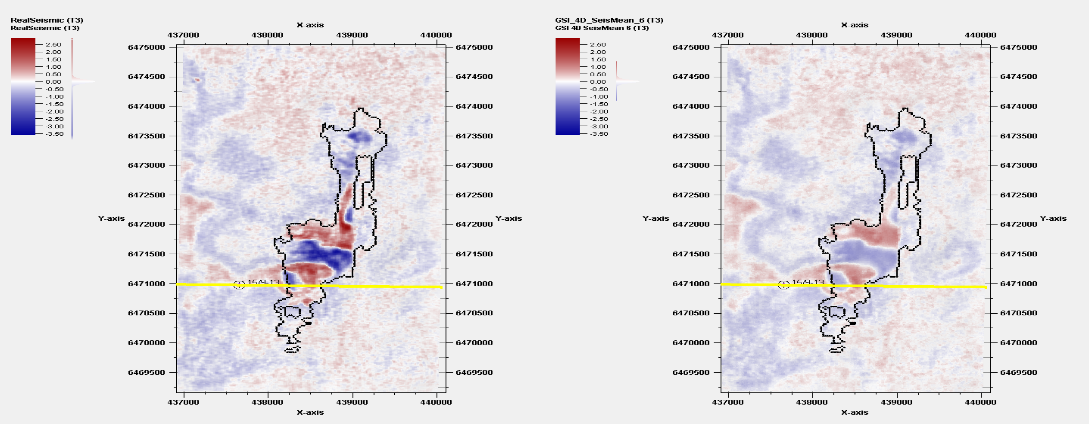

(a) Real Seismic 2006

(b) Synthetic Seismic 2001 GSI 4D

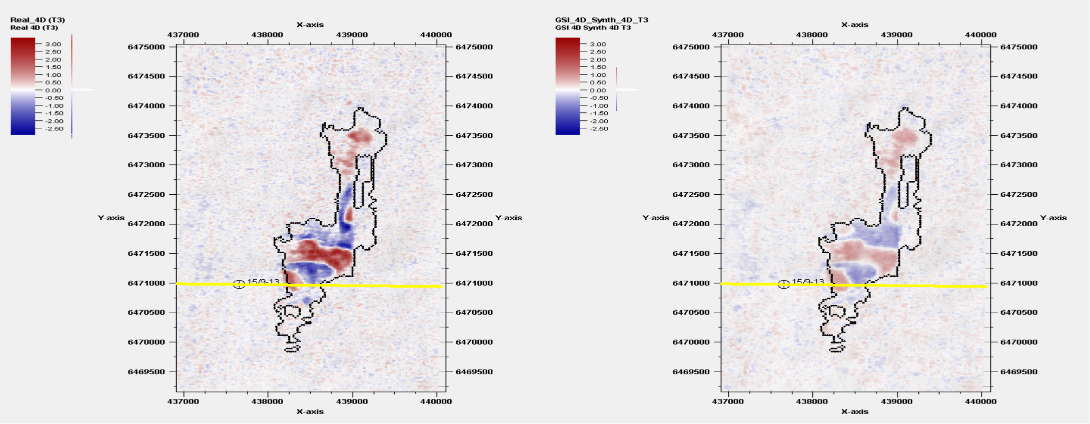

(c) Real Seismic Base minus Real Seismic Monitor

(d) Real Seismic Base minus Synthetic Seismic Monitor 2001 GSI 4D

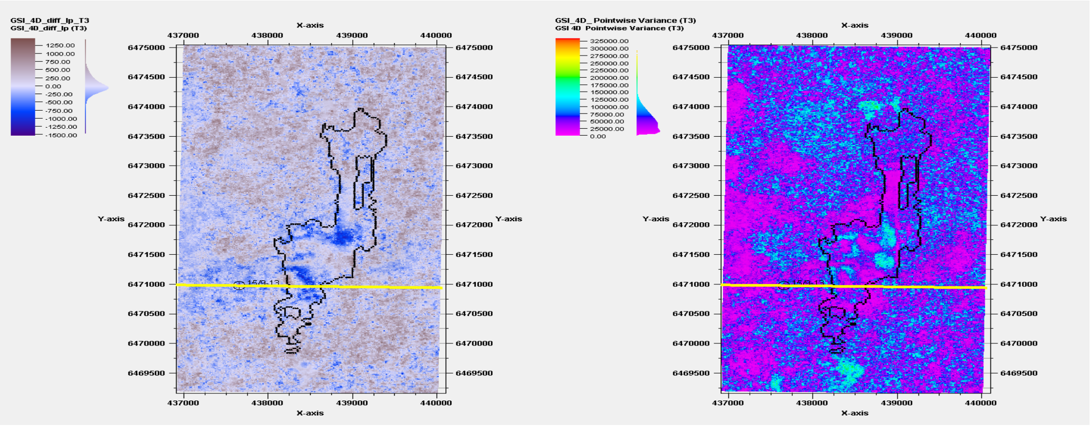

(e) Ip Base minus Ip Monitor 2001 GSI 4D

(f) Point-wise Variance

Figure A.17: Processing GSI 4D 2006 Results L9

A.5 Model Domain GSI L9

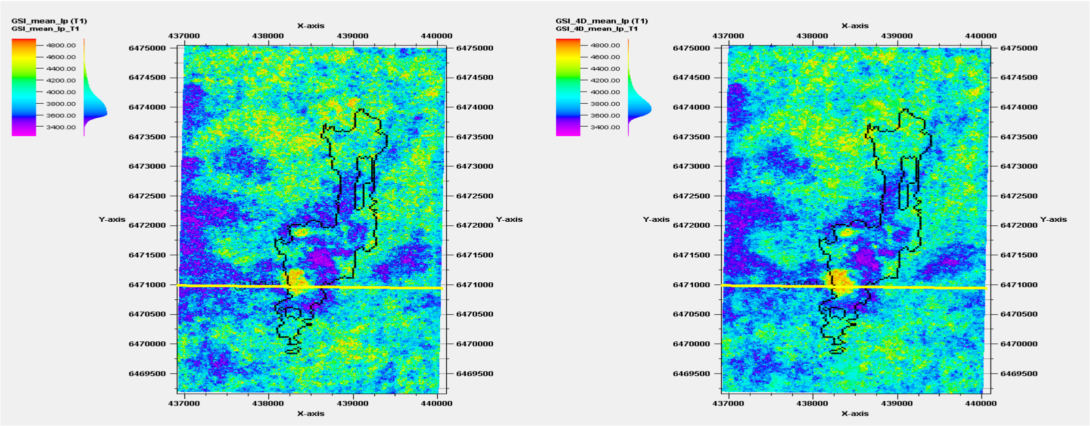

(a) Ip 2001 GSI

(b) Ip 2001 GSI 4D

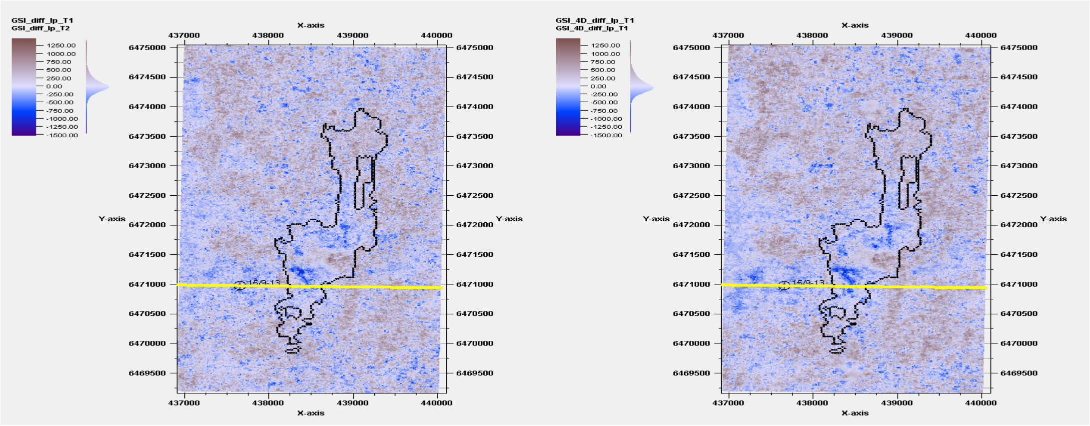

(c) Ip Base Minus Ip Monitors 2001 GSI

(d) Ip Base Minus Ip Monitors 2001 GSI 4D

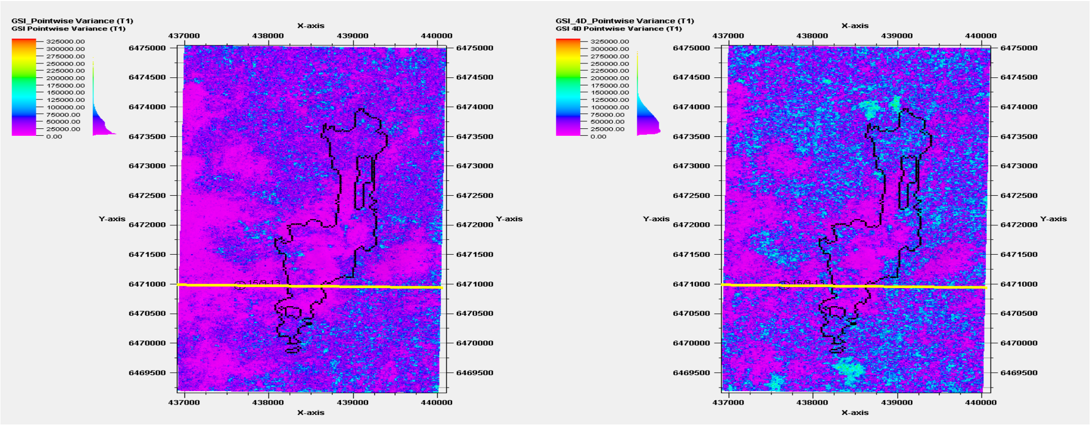

(e) Point-wise Variance 2001 GSI

(f) Point-wise Variance 2001 GSI 4D

Figure A.18: Model Domain 2001 L9

A.6 Seismic Domain L5

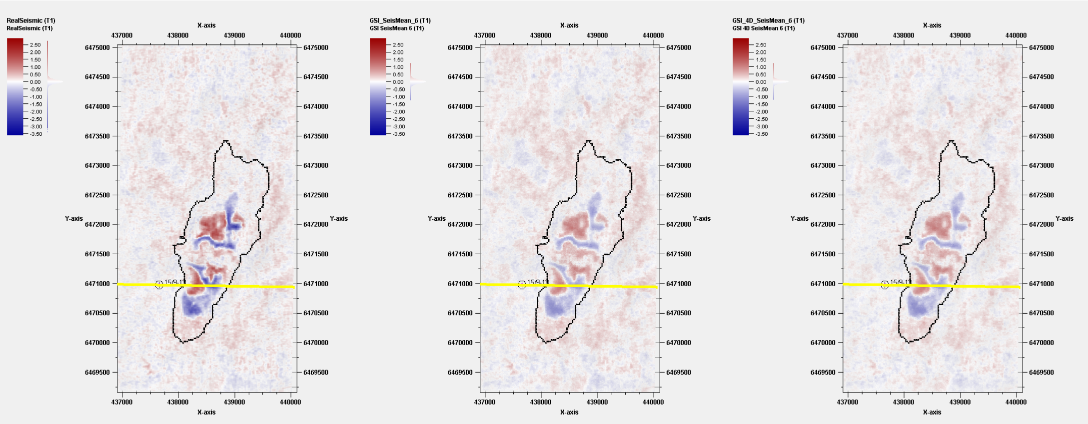

(a) Real Seismic 2001 **(b)** Synthetic Seismic 2001 GSI **(c)** Synthetic Seismic 2001 GSI 4D

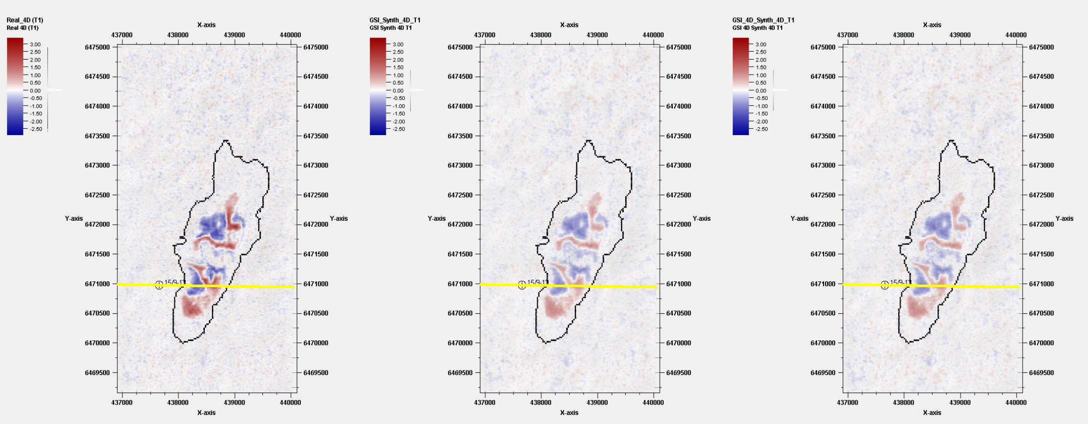

(d) Real Seismic Base Minus Real Seismic Monitors 2001 **(e)** Real Seismic Base Minus Synthetic Seismic Monitors 2001 GSI **(f)** Real Seismic Base Minus Synthetic Seismic Monitors 2001 GSI 4D

Figure A.19: Seismic Domain 2001 L5

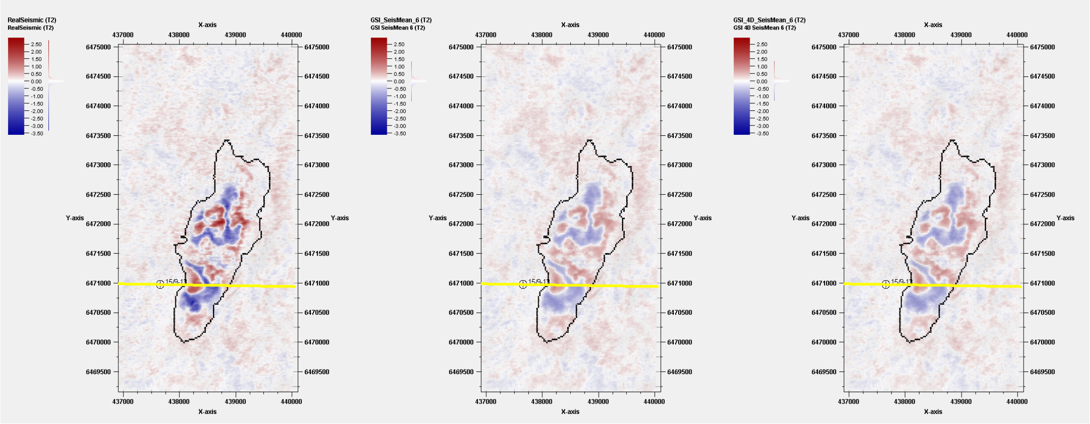

(a) Real Seismic 2004 L5

(b) Synthetic Seismic 2004 GSI L5

(c) Synthetic Seismic 2004 GSI 4D L5

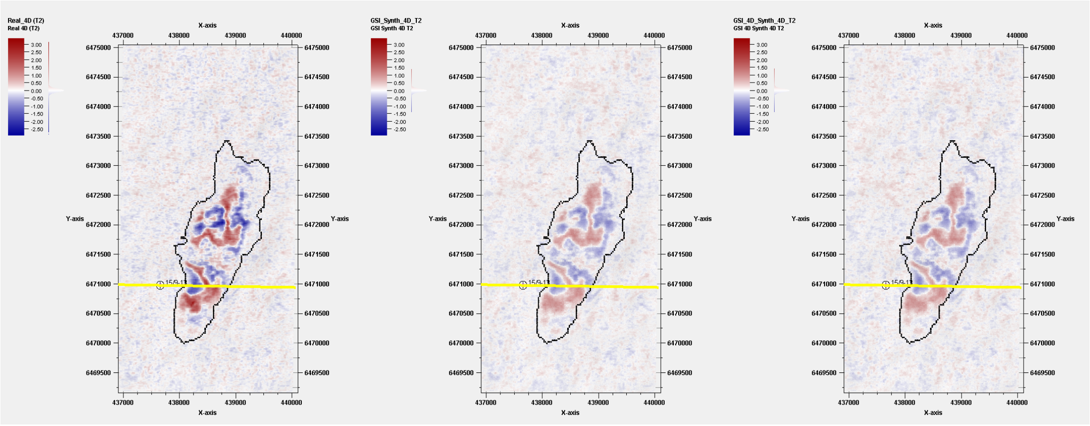

(d) Real Seismic Base Minus Real Seismic Monitors 2004 L5

(e) Real Seismic Base Minus Synthetic Seismic Monitors 2004 GSI L5

(f) Real Seismic Base Minus Synthetic Seismic Monitors 2004 GSI 4D L5

Figure A.20: Seismic Domain 2004 L5

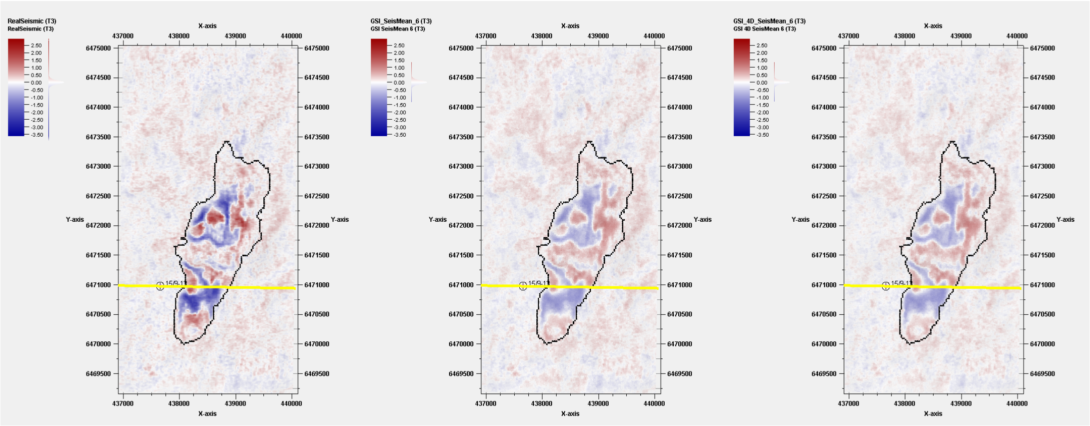

(a) Real Seismic 2006 L5

(b) Synthetic Seismic 2006 GSI L5

(c) Synthetic Seismic 2006 GSI 4D L5

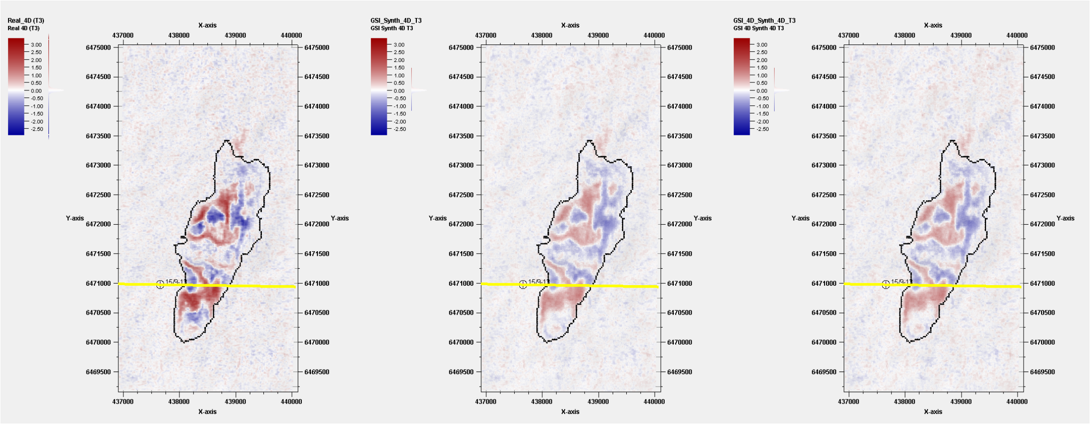

(d) Real Seismic Base Minus Real Seismic Monitors 2006 L5

(e) Real Seismic Base Minus Synthetic Seismic Monitors 2006 GSI L5

(f) Real Seismic Base Minus Synthetic Seismic Monitors 2006 GSI 4D L5

Figure A.21: Seismic Domain 2006 L5

A.7 Seismic Domain L9

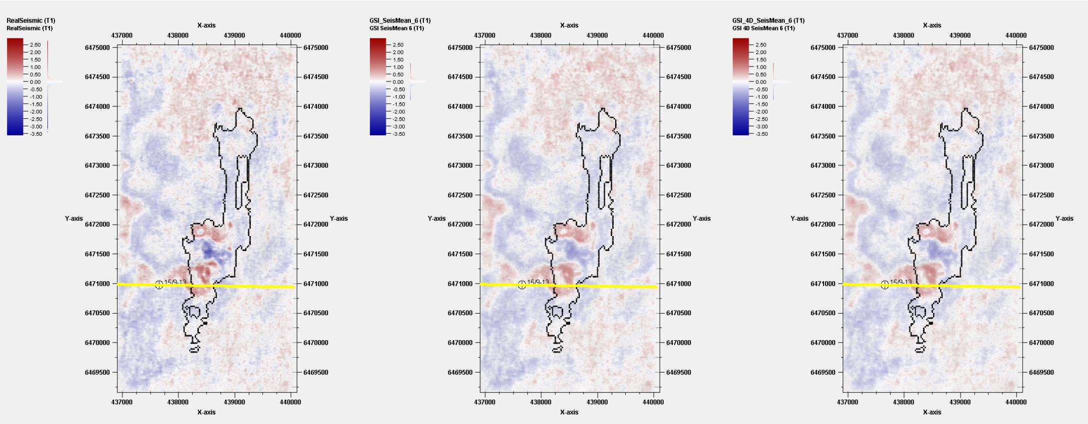

(a) Real Seismic 2001 **(b)** Synthetic Seismic 2001 GSI **(c)** Synthetic Seismic 2001 GSI 4D

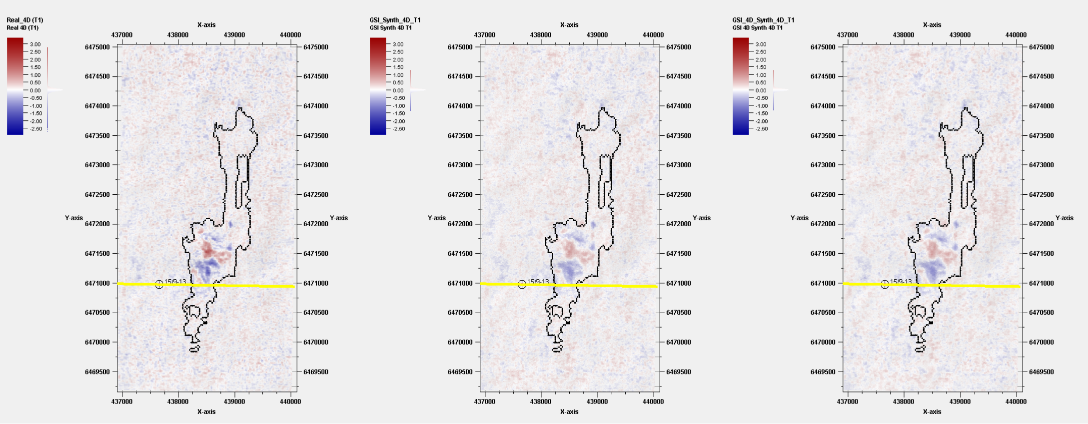

(d) Real Seismic Base Minus Real Seismic Monitors 2001 **(e)** Real Seismic Base Minus Synthetic Seismic Monitors 2001 GSI **(f)** Real Seismic Base Minus Synthetic Seismic Monitors 2001 GSI 4D

Figure A.22: Seismic Domain 2001 L9

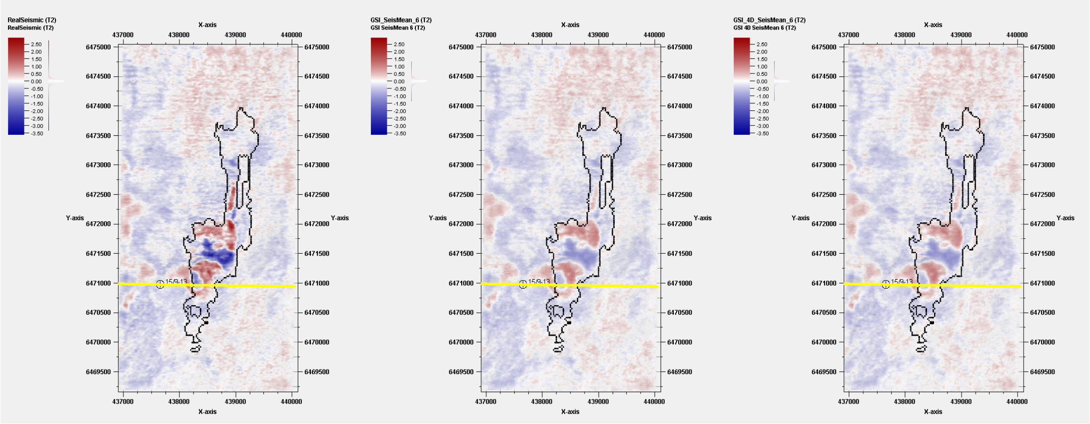

(a) Real Seismic 2004 L9

(b) Synthetic Seismic 2004 GSI L9

(c) Synthetic Seismic 2004 GSI 4D L9

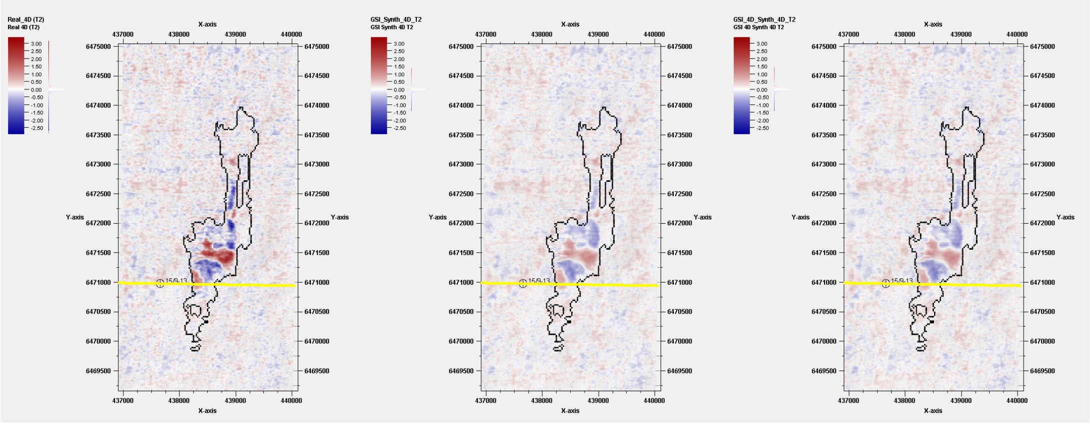

(d) Real Seismic Base Minus Real Seismic Monitors 2004 L9

(e) Real Seismic Base Minus Synthetic Seismic Monitors 2004 GSI L9

(f) Real Seismic Base Minus Synthetic Seismic Monitors 2004 GSI 4D L9

Figure A.23: Seismic Domain 2004 L9

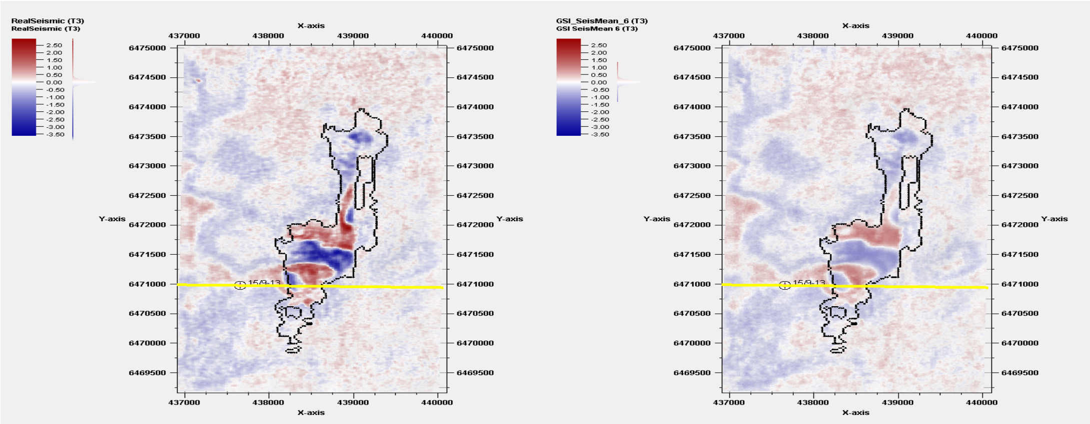

(a) Ip 2006 GSI

(b) Ip 2006 GSI 4D

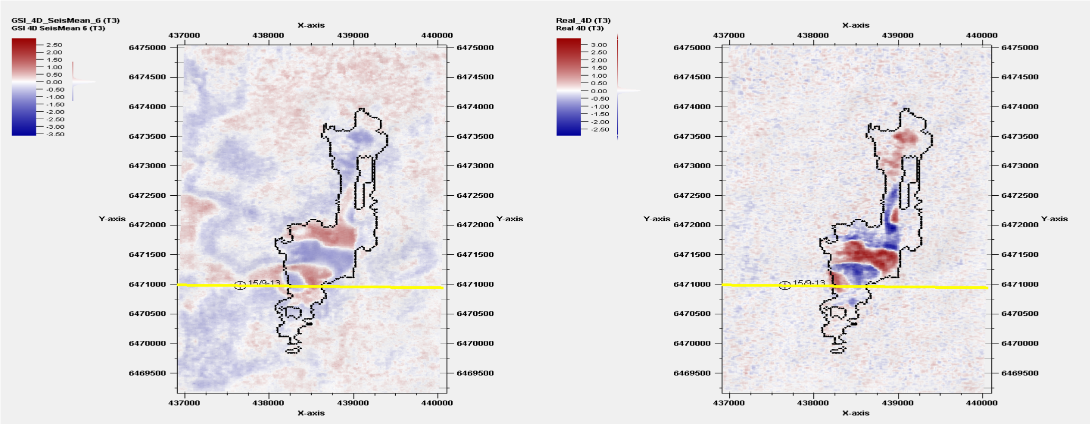

(c) Ip Base Minus Ip Monitors 2006 GSI

(d) Ip Base Minus Ip Monitors 2006 GSI 4D

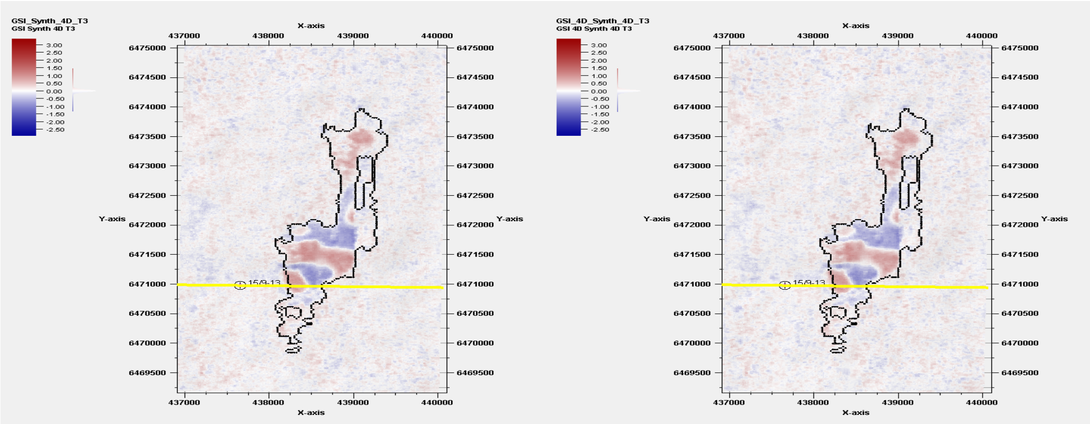

(e) Point-wise Variance 2006 GSI

(f) Point-wise Variance 2006 GSI 4D

Figure A.24: Model Domain 2006 L9

Table A.1: Model Dimensions

Axis	Min	Max	Delta
X	436910.32	440103.47	3193.14
Y	6469154.60	6475043.73	5889.13
Time	-1332.74	-750.22	582.53
Lat	58°21’26.6323”N	58°24’38.6217”N	0°03’11.9894”
Long	1°55’13.1024”E	1°58’35.3111”E	0°03’22.2086”

Description	Value
Original SRD:	SRD Z=0.0 RV=1480.0
Target SRD:	SRD Z=0.0 RV=1480.0
Absolute shift:	0.00
In this folder:	65
Includes sub folders:	65
Grid cells (nI x nJ x nK)	249 x 468 x 255
Total number of grid cells:	29715660
Total number of cells in filtered area:	29696535

Table A.2: Acoustic Impedance

Name	Type	Min	Max	Delta	N	Mean	Std	Var	Sum
P_impedanc_Well_15-9/13	Cont.	3235.64	4912.88	1677.24	255	3815.44	363.49	132121.73	972938.08
GSI_mean_Ip (T0)	Cont.	3235.64	4912.88	1677.24	29696535	3821.95	287.85	82856.34	1.13E+11
GSI_4D_mean_Ip (T1)	Cont.	3235.64	4912.88	1677.24	29696535	3813.73	204.87	41972.36	1.13E+11
GSI_mean_Ip (T1)	Cont.	3235.64	4912.88	1677.24	29696535	3814.54	235.57	55492.14	1.13E+11
GSI_4D_mean_Ip (T2)	Cont.	3235.64	4912.88	1677.24	29696535	3814.11	222.6	49548.92	1.13E+11
GSI_mean_Ip (T2)	Cont.	3235.64	4912.88	1677.24	29696535	3814.72	235.91	55653.36	1.13E+11
GSI_4D_mean_Ip (T3)	Cont.	3235.64	4912.88	1677.24	29696535	3814.3	209.05	43703.21	1.13E+11
GSI_mean_Ip (T3)	Cont.	3235.64	4912.88	1677.24	29696535	3815.2	235.85	55627.12	1.13E+11

Table A.3: Point-wise Variance

Name	Type	Min	Max	Delta	N	Mean	Std	Var	Sum
GSI_Pointwise Variance (T0)	Cont.	0	216059.16	216059.16	29696535	27919.84	22571.9	509490860.5	8.29E+11
GSI_4D_Pointwise Variance (T1)	Cont.	0	289506.78	289506.78	29696535	54035.42	33702.64	1135867643	1.60E+12
GSI_Pointwise Variance (T1)	Cont.	0	270375.94	270375.94	29696535	39667.18	28129.64	791276477.7	1.18E+12
GSI_4D_Pointwise Variance (T2)	Cont.	0	276328.25	276328.25	29696535	44623.96	30538.35	932590862.9	1.33E+12
GSI_Pointwise Variance (T2)	Cont.	0	278387.91	278387.91	29696535	39682.3	28169.78	793536639.5	1.18E+12
GSI_4D_ Pointwise Variance (T3)	Cont.	0	292465.03	292465.03	29696535	52438.65	33256.08	1105966938	1.56E+12
GSI_Pointwise Variance (T3)	Cont.	0	259808.73	259808.73	29696535	37805.19	27645.73	764286488.8	1.12E+12

Table A.4: Seismic base minus monitor

Name	Type	Min	Max	Delta	N	Mean	Std	Var	Sum
Real_4D (T1)	Cont.	-2.72	2.76	5.48	29696535	0	0.13	0.02	-5032.08
GSI_4D_Synth_4D_T1	Cont.	-1.33	1.26	2.6	29696535	0	0.11	0.01	-1796.97
GSI_Synth_4D_T1	Cont.	-1.37	1.29	2.65	29696535	0	0.11	0.01	-2353.33
Real_4D (T2)	Cont.	-2.84	3.13	5.96	29696535	0	0.18	0.03	-15347.78
GSI_4D_Synth_4D_T2	Cont.	-1.38	1.41	2.79	29696535	0	0.14	0.02	2957
GSI_Synth_4D_T2	Cont.	-1.4	1.38	2.78	29696535	0	0.14	0.02	1696.03
Real_4D (T3)	Cont.	-2.93	3.4	6.33	29696535	0	0.17	0.03	-17107.31
GSI_4D_Synth_4D_T3	Cont.	-1.36	1.45	2.81	29696535	0	0.13	0.02	5667.1
GSI_Synth_4D_T3	Cont.	-1.32	1.44	2.76	29696535	0	0.13	0.02	3996.75

Table A.5: Acoustic Impdedance Difference

Name	Type	Min	Max	Delta	N	Mean	Std	Var	Sum
GSI_4D_diff_Ip_T1	Cont.	-1453.06	1398.34	2851.4	29696535	8.22	251.13	63068.69	244127789.3
GSI_diff_Ip_T1	Cont.	-1468.26	1418.09	2886.35	29696535	7.42	244.19	59629.84	220290819.5
GSI_4D_diff_Ip_T2	Cont.	-1472.73	1412.82	2885.55	29696535	7.84	281.68	79345.55	232846706
GSI_diff_Ip_T2	Cont.	-1486.72	1402.72	2889.44	29696535	7.23	270.06	72931.08	214669689.1
GSI_4D_diff_Ip_T3	Cont.	-1467.47	1426.12	2893.59	29696535	7.65	261.17	68211.3	227130303.9
GSI_diff_Ip_T3	Cont.	-1536.71	1371.49	2908.2	29696535	6.75	252.82	63918.57	200594440.5

Table A.6: Similarity Ip

Name	Type	Min	Max	Delta	N	Mean	Std	Var	Sum
GSI Similarity Ip (T0)	Cont.	0	0.95	0.95	29696535	0.8947	0.0944	0.0089	26570195.92
GSI_4D Similarity Ip (T1)	Cont.	0	0.95	0.95	29696535	0.7984	0.1596	0.0255	23710125.86
GSI Similarity Ip (T1)	Cont.	0	0.95	0.95	29696535	0.8837	0.1057	0.0112	26241452.83
GSI_4D Similarity Ip (T2)	Cont.	0	0.95	0.95	29696535	0.8634	0.1201	0.0144	25639325.37
GSI Similarity Ip (T2)	Cont.	0	0.95	0.95	29696535	0.8829	0.1073	0.0115	26218814.54
GSI_4D Similarity Ip (T3)	Cont.	0	0.95	0.95	29696535	0.8035	0.1589	0.0252	23862154.76
GSI Similarity Ip (T3)	Cont.	0	0.95	0.95	29696535	0.8826	0.106	0.0112	26209534.59

Table A.7: Similarity Seismic

Name	Type	Min	Max	Delta	N	Mean	Std	Var	Sum
GSI Similarity Seismic (T0)	Cont.	0.3684	0.9666	0.5982	29696535	0.8877	0.0442	0.002	26361524.13
GSI_4D Similarity Seismic (T1)	Cont.	0.3103	0.9702	0.6599	29696535	0.8796	0.0528	0.0028	26121438.8
GSI Similarity Seismic (T1)	Cont.	0.3461	0.9699	0.6238	29696535	0.9033	0.031	0.001	26823854.89
GSI_4D Similarity Seismic (T2)	Cont.	0.2725	0.9697	0.6972	29696535	0.8871	0.0433	0.0019	26345270.43
GSI Similarity Seismic (T2)	Cont.	0.3932	0.969	0.5758	29696535	0.8971	0.0335	0.0011	26639405.94
GSI_4D Similarity Seismic (T3)	Cont.	0.2367	0.9697	0.733	29696535	0.8699	0.0543	0.0029	25834321.14
GSI Similarity Seismic (T3)	Cont.	0.3335	0.9672	0.6337	29696535	0.8936	0.0334	0.0011	26535429.28